

# THE $\text{HeH}^+$ ISOTOPOLOGUES IN INTENSE ASYMMETRIC LASER FIELDS

Von der Fakultät für Mathematik und Physik  
der Gottfried Wilhelm Leibniz Universität Hannover

zur Erlangung des akademischen Grades  
Doktor der Naturwissenschaften  
Dr. rer. nat.

genehmigte Dissertation von

**M. Sc. Florian Oppermann**

2023

Referent: Prof. Dr. Manfred Lein  
Korreferentin: Prof. Dr. Stefanie Gräfe  
Korreferent: Prof. Dr. Volker Engel

Tag der Promotion: 12. Juni 2023

<https://doi.org/10.15488/13880>

# Abstract

In this thesis, the effects of intense laser pulses on molecular dynamics are studied at the example of the helium hydride molecular ion  $\text{HeH}^+$ . It serves as a benchmark system for asymmetric molecules because it has features such as an asymmetric mass distribution, a permanent dipole moment and a rich structure of electronic levels while still being relatively simple and easy to model. In order to carry out numerical simulations in high accuracy, we first develop a reduced-dimensional model system for  $\text{HeH}^+$  that still reproduces crucial real-world data. This quantum-mechanical non-Born-Oppenheimer model is then used in time-dependent Schrödinger-equation calculations to study various effects:

The ionization (electron removal) and subsequent dissociation of  $\text{HeH}^+$  are studied in laser fields of 800 nm and 400 nm. Enhanced ionization at a certain internuclear distance as well as excitation of vibrational motion—if possible—have significant effects on the molecular dynamics and the ionization probability.

Breaking the molecule into  $\text{He} + \text{H}^+$  (*ground-state dissociation*) or  $\text{He}^+ + \text{H} + e^-$  (*ionization*) are two prototypical, very simple chemical reactions. By means of collinearly polarized two-color fields which have a spatial asymmetry, we show that it is possible to switch from one fragmentation channel to the other one just using the relative two-color delay as a control knob.

Finally, molecular dynamics depends on the choice of isotopologue, i. e. the nuclear masses. The reduced mass of the nuclei has an obvious and very important effect on the time scale of vibrational motion and the available  $\text{HeH}^+$  isotopologues allow to study this. However, also the mass distribution within the molecule influences the dynamics, especially in molecular ions where the dipole moment depends on the nuclear center of mass.

The quantum-mechanical non-Born-Oppenheimer calculations are supported by a multi-level Born-Oppenheimer model and by classical-trajectory calculations where appropriate. We compare some of our results to measurement data and suggest feasible experimental parameters for other of our findings where there are no measured results yet.

**Keywords:** molecular dynamics, time-dependent Schrödinger equation, strong-field physics



# Contents

<b>Abstract</b>	<b>i</b>
<b>Atomic units</b>	<b>v</b>
<b>1 Introduction</b>	<b>1</b>
1.1 Quantum mechanics and limitations . . . . .	1
1.2 Molecules and strong-field physics . . . . .	2
1.3 The helium hydride molecular ion . . . . .	4
1.4 Open questions and outline . . . . .	5
1.5 Approximations . . . . .	6
<b>2 HeH<sup>+</sup> in monochromatic 400nm and 800nm fields</b>	<b>13</b>
2.1 Non-Born-Oppenheimer TDSE model . . . . .	13
2.2 Fragmentation pathways . . . . .	17
2.3 Kinetic-energy release . . . . .	19
2.4 Frozen-nuclei ionization and enhancement . . . . .	23
2.5 Ionization and frustrated ionization . . . . .	27
2.6 Application of the HeH <sup>+</sup> model to H <sub>2</sub> <sup>+</sup> . . . . .	31
2.7 Strong-field experiments on HeH <sup>+</sup> . . . . .	33
2.8 Focal-volume / intensity averaging . . . . .	35
2.9 Intensity dependence of ionization KER . . . . .	37
2.10 Ionization of HeD <sup>+</sup> . . . . .	40
2.11 Conclusion . . . . .	42
<b>3 Two-color dissociation vs. ionization control at 1380nm</b>	<b>43</b>
3.1 Tailored fields . . . . .	43
3.2 Non-Born-Oppenheimer and focal-volume-averaged results . . . . .	45
3.3 Two-color ionization in detail . . . . .	48
3.4 Two-color dissociation in detail . . . . .	54
3.5 Photoelectron momentum distribution . . . . .	57
3.6 Effect of the pulse duration . . . . .	58

3.7	Conclusion . . . . .	60
<b>4</b>	<b>Mass-dependent dissociation dynamics</b>	<b>61</b>
4.1	Quantum models . . . . .	63
4.1.1	Electron-nuclear non-Born-Oppenheimer TDSE . . . . .	63
4.1.2	Two-level Born-Oppenheimer TDSE . . . . .	64
4.2	Classical-trajectory model . . . . .	67
4.3	Excursus: Classical initial conditions . . . . .	68
4.3.1	Equilibrium position & expectation values . . . . .	69
4.3.2	Fixed-energy momentum or position distribution . . . . .	69
4.3.3	Wigner or Husimi distribution . . . . .	70
4.3.4	Stationary initial conditions . . . . .	70
4.4	Quantum ladder climbing to dissociation . . . . .	72
4.5	Electronic excitation . . . . .	76
4.6	Classical dissociation probabilities . . . . .	76
4.7	Conclusion . . . . .	79
<b>5</b>	<b>Conclusion and outlook</b>	<b>81</b>
<b>A</b>	<b>Born-Oppenheimer approximation</b>	<b>85</b>
A.1	General considerations . . . . .	85
A.2	Two-level Born-Oppenheimer model . . . . .	87
<b>B</b>	<b>Fine-tuning of soft-core parameters</b>	<b>91</b>
B.1	Parameters for one-electron model . . . . .	91
B.2	Parameters for two-electron model . . . . .	99
	<b>Bibliography</b>	<b>109</b>
	<b>Acknowledgements</b>	<b>125</b>
	<b>Curriculum Vitae</b>	<b>127</b>
	<b>List of publications</b>	<b>128</b>

# Atomic units

The shortest unit of time in the multiverse is the New York Second, defined as the period of time between the traffic lights turning green and the cab behind you honking.

---

Terry Pratchett, *Lords and Ladies*, 1992

Throughout this thesis, atomic units (a.u.) are used except otherwise noted. Atomic units are defined by treating the reduced Planck constant  $\hbar$ , the elementary charge  $e$ , the electron rest mass  $m_e$  and  $4\pi\epsilon_0$  (where  $\epsilon_0$  is the vacuum permittivity) as unity. Note that the electron charge is  $-1$  in atomic units. Important derived units are the length unit  $a_0 = 4\pi\epsilon_0\hbar^2/(m_e e^2) \approx 5.3 \times 10^{-11}$  m (Bohr radius), the energy unit  $E_h = m_e e^4/(4\pi\epsilon_0\hbar)^2 \approx 4.4 \times 10^{-18}$  J  $\approx 27.2$  eV (Hartree) and the time unit  $\hbar/E_h \approx 2.4 \times 10^{-17}$  s = 24 as (as = attoseconds).

The conversion factors from atomic units to other unit systems are  $\hbar/a_0$  for momentum,  $E_h/a_0$  for force and  $E_h/(ea_0)$  for electric field strength. In atomic units, the speed of light has the value of the inverse fine-structure constant,  $c = e^2/(4\pi\epsilon_0\hbar\alpha) = 1/\alpha \approx 137$ .

Note that we give some properties in SI units for convenience. This applies to the laser intensity ( $\text{W}/\text{cm}^2$ ), laser wavelength (nm or  $\mu\text{m}$ ) and times (typically fs). We will always explicitly specify the units if other than atomic units are used.

In the bottom-left corner, you can see the time evolution of the HeH<sup>+</sup> electron-nuclear wave function ( $v = 5$  initial state) in an 800 nm seven-cycle laser pulse with  $3 \times 10^{14}$  W/cm<sup>2</sup> peak intensity. Flip the book pages from front to back in order to see the time evolution as a “movie”. See the explanation of figure 2.2 (page 18) for details about the plot.





# 1 Introduction

The fundamental laws necessary for the mathematical treatment of large parts of physics and the whole of chemistry are thus fully known, and the difficulty lies only in the fact that application of these laws leads to equations that are too complex to be solved.

---

Paul Dirac, 1929

## 1.1 Quantum mechanics and limitations

Leaving relativistic and gravitational effects aside, most physical systems can be fully described by specifying a Hamilton operator  $H$  and an initial state  $\psi(t_0)$  whose time evolution is then determined by the time-dependent Schrödinger equation (TDSE)

$$i\frac{d}{dt}\psi(t) = H\psi(t).$$

Results of measurements are given as probabilities to find a certain value, e. g. the probability for a self-adjoint operator  $A$  with (non-degenerate) eigenvalue  $\lambda_i$  and eigenstate  $\Lambda_i$  the probability  $w$  to find this value when measuring  $\psi$  is

$$w(\lambda_i, A, \psi) = |\langle \Lambda_i | \psi \rangle|^2$$

and the expectation value for the measurement is  $\langle \psi | A | \psi \rangle$ .

In this thesis, we investigate the dynamics of molecules (especially the  $\text{HeH}^+$  molecular ion) in strong laser fields. Within the general approximations used here (see section 1.5), we can easily write down the full Hamiltonian explicitly—and we do that in appendix A—but it contains three spatial degrees of freedom per particle (nucleus or electron), i. e. 12 degrees of freedom for the two nuclei and two electrons of  $\text{HeH}^+$ . Even though  $\text{HeH}^+$  is one of

the simplest molecules that exist, it is practically impossible to calculate its dynamics without further significant approximations<sup>1</sup>.

This is true for basically all quantum systems. Even though we know the fundamental laws, we cannot directly deduce predictions such as binding strengths of atoms or molecules, ionization rates or dynamically competing processes et cetera. We need models and approximations on the theoretical side and measurements that isolate specific effects on the experimental side in order to understand the mechanisms and processes in complex quantum systems. Light-matter interaction is one example how we can study dynamics in such quantum systems and it has been a useful tool for about two centuries, from absorption spectroscopy [1] and the photoelectric effect [2, 3] through development of the first laser [4] which in turn opened up new fields like photonics [5] and—important for us—strong-field and attosecond physics [6]. In the next section we will illuminate what strong-field physics is and how we can apply it to learn something about molecules.

### 1.2 Molecules and strong-field physics

Molecules are quantum systems that consist of multiple (at least two) atoms which are bound to each other due to their electron configuration, i. e. taking them apart would increase the total energy of the system.

We consider the field of molecular strong-field dynamics from two different perspectives: Coming from the fundamental theoretical-physics foundations, it seems obvious to first consider *atoms* as compound entities of a nucleus (neutrons and protons) and electrons and then—as the next complex objects—study molecules. In a hydrogen atom, the “binding force”<sup>2</sup> of a classical electron in a distance of  $1 a_0 \approx 5.3 \times 10^{-11}$  m (Bohr radius) from a proton is  $8.2 \times 10^{-8}$  N which is the same as the force that an electric field of  $5.1 \times 10^{11}$  V/m exerts on the electron. This field strength occurs in a linearly polarized continuous-wave laser with  $3.5 \times 10^{16}$  W/cm<sup>2</sup> intensity. Using laser intensities of roughly this magnitude justifies the name *strong-field* physics<sup>3</sup> [7]. Shorter and stronger

---

<sup>1</sup>In a numerical grid-based representation with only ten grid points per degree of freedom (we use  $10^2$  to  $10^4$ ) and only one byte per grid point (we use double-precision complex numbers, i. e. 16 bytes per grid point), the wave function occupies  $10^{12}$  B = 1 TB of computer memory.

<sup>2</sup>We use quotation marks here because a classical electron cannot stably orbit a nucleus. What we calculate is the force due to the  $-1/r$  potential (in atomic units) of the proton.

<sup>3</sup>Note that the “binding force” scales with the distance from the nucleus like  $1/r^2$  (and is



laser pulses allow to access length and time scales that go down to the atomic level [8]. Many non-linear effects take place during strong-field interaction such as above-threshold ionization [9], non-sequential double ionization [10] and high-harmonic generation [11], just to name a few. The latter has led to the field of attosecond-pulse generation [12] which in turn allowed to study even shorter time scales. Many of these effects can be described efficiently by models and simulations that do not require to solve the TDSE for the whole system. Selected prevalent examples are the PPT/ADK<sup>4</sup> ionization rate [13–15], the strong-field approximation [16–18] and the three-step model of high-harmonic generation [19, 20]. The electron motion follows the electric-field oscillations which can go down to the attosecond ( $10^{-18}$  s) time scale.

Since molecular bonds are created by interacting electrons shielding the positively charged nuclei from each other, the attosecond electron dynamics is also particularly important for the understanding of the formation, dynamics and breaking of molecular bonds. Additionally, molecules have more degrees of freedom with different time scales<sup>5</sup>: Vibrational motion of the nuclei (period for H<sub>2</sub>: 7.7 fs) and rotation of the molecule (period for H<sub>2</sub> with angular momentum corresponding to quantum number  $J = 0, 1, \dots$ :  $270 \text{ fs}/\sqrt{J(J+1)}$ ) [21, p. 364]. The different time scales reflect the hierarchy of energy spacings: electronic > vibrational > rotational. *Femtochemistry* [22, 23] utilizes the different time scales in pump-probe experiments where femtosecond coherent nuclear dynamics is initiated and probed, respectively, by much faster electronic processes induced by laser pulses. Even though the time scales of different degrees of freedom usually differ by large factors, often they cannot be treated independently [24]. Examples are interactions of the freed electron with the moving nuclei (e. g. in the generation of photoelectrons [25] or high harmonics [26, 27]) and charge-resonance-enhanced ionization (CREI), a strong modulation of the ionization yield depending on the internuclear distance [28, 29].

---

partially shielded in larger atoms) and that the laser field does not need to reach exactly the strength of the Coulomb force in order to have a significant effect on the electron. Thus in practice, laser intensities are usually smaller. What is strong depends on the target system.

<sup>4</sup>Named after A. M. Perelomov, V. S. Popov and M. V. Terent'ev and M. V. Ammosov, N. B. Delone and V. P. Krainov, respectively.

<sup>5</sup>As energy eigenstates, both vibrational and rotational quantum levels are stationary and thus have no period. Time scales are calculated for corresponding classical systems and usually agree with quantum wave-packet motion.

## 1 Introduction

The name femtochemistry indicates the second perspective on molecular strong-field physics: chemistry. From a physicist's point of view, chemistry is the physics of valence electrons. Thus, understanding and controlling electron movement is key for understanding and steering chemical reactions or shifting chemical equilibria [30]. Ubiquitous redox reactions are based on electron transfer [31, 32] but charge transfer in molecules is an active field of research far beyond that, see [33] for a review. The chemical reactions we consider in this thesis are probably the simplest kind of reactions—breakup of a diatomic molecule. However, there are still different possible outcomes: *Dissociation*, that is, fragmentation without electron removal; *ionization*, here defined as removal of one electron (followed by fragmentation); *double ionization*, that is, removal of both electrons (followed by fragmentation); see figure 1.1. The combined dynamics of nuclei and electrons determine the dominating fragmentation channel.

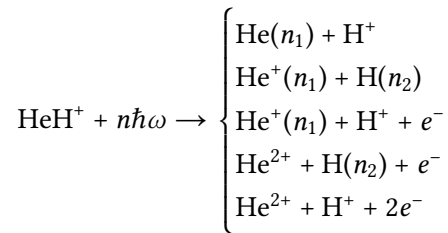


Figure 1.1: Possible fragmentation channels for  $\text{HeH}^+$ . The first two correspond to dissociation, the next two to single ionization and the last one to double ionization.  $n_1$  and  $n_2$  indicate possible excitation states of the reaction products.

### 1.3 The helium hydride molecular ion

$\text{HeH}^+$  is one of the simplest molecules that exist and the first one that formed after Big Bang nucleosynthesis [34] but it has not been directly detected in interstellar space until 2016 (measurement, published 2019) [35]. Due to the strong binding potential of the helium core, it can be thought of as a helium atom that has a proton attached to it [36]. At the equilibrium internuclear



distance of 1.46 a.u. it has a vertical ionization potential<sup>6</sup> of 44.4 eV, the dissociation energy from the vibrational ground state is 1.8 eV

HeH<sup>+</sup> is a particularly interesting benchmark molecule because it is very simple *and* has a strong asymmetry—both regarding the mass and the charge distribution. There are numerous studies on H<sub>2</sub><sup>+</sup> and H<sub>2</sub> which serve as archetypes of symmetric diatomic molecules. However, many relevant molecules are not symmetric and HeH<sup>+</sup> may provide insights into their properties. Another inviting property of HeH<sup>+</sup> is that the mass distribution within the molecule depends strongly on the isotopologue. One measure for this is the ratio of nuclear masses of helium and hydrogen—short: mass ratio—which varies from 4:1 for the common <sup>4</sup>He<sup>1</sup>H<sup>+</sup> down to 1:1 for <sup>3</sup>HeT<sup>+</sup>. Therefore, mass effects can be assumed to be very pronounced compared to larger (heavier) molecules where the mass ratio often cannot be varied on such a broad range.

Since its first detection in a laboratory in 1925 [37], HeH<sup>+</sup> has been subject to various experimental and theoretical studies, e. g. spectroscopy in the infrared regime [38] and photoionization and -dissociation in the ultraviolet regime [39–42]. The strong-field dynamics of HeH<sup>+</sup> in infrared or optical laser pulses has only been studied in recent years by a few groups [43–52].

## 1.4 Open questions and outline

In this thesis, we aim to answer a few questions on strong-field effects in molecules with the example of HeH<sup>+</sup>.

1. How are nuclear and electronic motion connected, specifically for the competing ionization and dissociation in visible and near-infrared laser fields?

We will shed light on this question in chapter 2 which in parts is based on the following publication.

Philipp Wustelt et al. “Heteronuclear Limit of Strong-Field Ionization: Fragmentation of HeH<sup>+</sup> by Intense Ultrashort Laser Pulses”. In: *Phys. Rev. Lett.* 121 (7 2018), p. 073203. DOI: 10.1103/PhysRevLett.121.073203

---

<sup>6</sup>“Vertical” refers to Born-Oppenheimer potential-energy curves like figure 2.1 where vertical transitions between electronic states do not change the internuclear distance.

2. Can we steer the molecule into one of the two fragmentation channels ionization and dissociation by tuning a suitable laser pulse?

This question is the center of chapter 3 where two-color pulses are utilized. Some of the results have been published before in

Florian Oppermann et al. “Dissociation and ionization of  $\text{HeH}^+$  in sub-cycle-controlled intense two-color fields”. In: *Journal of Physics B: Atomic, Molecular and Optical Physics* 53.17 (2020). DOI: 10.1088/1361-6455/ab9a93.

3. What is the effect of the choice of isotopologue on strong-field ionization and dissociation? What effects are due to the reduced mass of the nuclei, what effect does the mass distribution have?

The effect of the reduced mass is already discussed in chapters 2 and 3 but we disentangle the mass ratio of the nuclei from the reduced mass in chapter 4 and study its isolated effect. The following publication covers some of the results from this chapter.

Florian Oppermann, Saurabh Mhatre, Stefanie Gräfe, and Manfred Lein. “Mass-ratio dependent strong-field dissociation of artificial helium hydride isotopologues”. In: *Journal of Physics B: Atomic, Molecular and Optical Physics* (2023), accepted. arXiv: 2301.04500

Before we start investigating the first question, the next section gives an overview of the approximations that are used throughout this thesis. Note that some technical details as well as a recap of the Born-Oppenheimer approximation can be found in the appendix from page 85 onwards.

### 1.5 Approximations

In the following chapters of this thesis, we will carry out simulations for several settings using different models. We describe the common set of approximations, their justifications and their limitations in this section.

The first class of approximations are quite general and are applicable in most studies of strong-field physics:

1. **No relativistic effects.** We ignore all effects that come from relativistic motion of the molecule or single electrons. This allows us to use standard



non-relativistic Hamiltonian operators like  $H = p^2/(2m) + V(x)$  for a single-particle system. As a justification, we can compare typical energy scales in the relativistic energy formula  $E^2 = p^2/(2m) + m^2c^4$  where  $c$  is the speed of light. For an electron, the rest mass corresponds to  $E_0 = mc^2 \approx 511$  keV, whereas the largest kinetic energies involved are typically reached during quiver motion in the laser field. Here, the ponderomotive energy (in atomic units) is given by  $U_p = E^2/(4\omega^2)$  where  $E$  is the electric field strength and  $\omega$  is the laser frequency / photon energy. For a field of  $10^{15}$  W/cm<sup>2</sup> intensity and 1200 nm wavelength,  $U_p = 134$  eV is less than 0.1 % of the rest-mass energy  $E_0$ .

Note that this approximation also excludes relativistic corrections that contribute to fine-structure splitting of energy eigenstates like spin-orbit coupling as well as more fundamental relativistic treatment like quantum electrodynamics.

2. **No fundamental forces beyond electrodynamics.** Although it is possible to induce nuclear fusion by very strong laser light [55, 56], we ignore the treatment of the strong interaction that would be necessary to cover those dynamics. For effects of the strong interaction force to be relevant, nuclei of two atoms would need to approach each other to at most a few fm =  $10^{-15}$  m [57]. At this distance, the energy stored in the Coulomb repulsion of just two protons is 1.44 MeV which again exceeds the occurring energies of a few to a few dozens of electronvolts by many orders of magnitude.
3. **Classical treatment of the laser light.** The correct theory to describe coherent light fields and their interaction with matter is quantum optics. Excitations of the quantized field are called photons and give rise to product (and possibly entangled) states of light and matter. Quantum optics explains effects such as spontaneous and stimulated emission which are essential for the theory of the laser.<sup>7</sup> Interestingly, resonant transitions and Rabi oscillations which correspond to absorption and emission of single photons can be described correctly in semi-classical

---

<sup>7</sup>Spontaneous emission cannot be explained with classical electrical fields. However, Albert Einstein correctly predicted both spontaneous and stimulated emission based on Planck's idea of quantized light already in 1916 [58, 59], well before quantum optics existed as a closed theory.

models with classical electric fields, even though the theory has no concept of a photon or quantized light [60]. This fact together with the huge number of photons in our laser pulses<sup>8</sup> justifies to include the laser interaction classically via an external time-dependent potential in the Hamiltonian.

- 4. Dipole approximation for the laser light.** Classical, i. e. non-quantized, light is described by solutions to Maxwell's equations [61]. In the absence of matter, the solutions are (superpositions of) propagating electric and magnetic vector fields that are orthogonal to each other and to the propagation direction  $\mathbf{n}$ . In Coulomb gauge, they are defined by a vector potential  $\mathbf{A}(\mathbf{r}, t)$  via  $\mathbf{E} = -\partial_t \mathbf{A}$  and  $\mathbf{B} = \nabla \times \mathbf{A} = \mathbf{n} \times \mathbf{E}/c$ . Then, the dipole approximation  $\mathbf{A}(\mathbf{r}, t) = \mathbf{A}(t)$  results in a spatially homogeneous electric field  $\mathbf{E}(t)$  and a vanishing magnetic field  $\mathbf{B} = 0$ . It is justified for laser pulses whose wavelength is much larger than the length scales of typical dynamics and if the Lorentz force  $\mathbf{v} \times \mathbf{B}$  is much smaller than the force from the electric field  $q\mathbf{r} \cdot \mathbf{E}$ . The ratio of the quiver radius<sup>9</sup> and the laser wavelength  $\lambda$  is given by  $E_0\lambda/(2\pi c)^2$ . For a field of  $10^{15}$  W/cm<sup>2</sup> and 1200 nm wavelength, this ratio is 0.5 %. Since  $|\mathbf{B}| = |\mathbf{E}|/c$ , the Lorentz force is small as long as the occurring velocities are much smaller than the speed of light which we have discussed at item 1.

For these reasons, we apply the dipole approximation throughout this thesis. It should be mentioned that although it is common practice to use the dipole approximation [62], non-dipole effects are important in some strong-field settings [50, 63].

In addition to these general approximations we make further simplifications which are more specific to the actual system we consider, the HeH<sup>+</sup> molecular ion.

- 5. Single-active-electron (SAE) approximation.** For the reasons outlined in section 1.1, it is very hard to simulate all electronic degrees of freedom of atoms and molecules with many electrons. We briefly discuss three common ways to handle this problem: First, one can use

---

<sup>8</sup>A 1 mJ laser pulse at 800 nm wavelength contains  $4 \times 10^{15}$  photons.

<sup>9</sup>The quiver motion is typically calculated for a classical electron in a linearly polarized continuous-wave laser field  $\mathbf{E}(t) = E_0 \cos(\omega t)\mathbf{e}_x$ . The quiver radius  $E_0/\omega^2$  is the amplitude of the oscillating motion of the electron.





density-functional theory (DFT) [64, 65] which works with electron densities instead of correlated electron wave functions. This reduces the dimensionality dramatically (from  $3N$  to 3 if we ignore the spin) but for the price that the relevant functionals are not exactly known. Second, one can keep (at least some of) the electronic degrees of freedom but restrict the size of specific dimensions by limiting the basis set to suitable states. This allows to treat the electrons fully correlated while keeping the computational cost manageable<sup>10</sup> but it needs a lot of knowledge about the system in order to choose the basis states efficiently. Examples for this are the restricted- or generalized-active-space configuration-interaction methods [66, 67]. Third (and actually a special case of the second method), one can simply assume that all but one electron show little dynamics during the light-matter interaction and can thus be ignored. This frees computational resources to treat the remaining *single active electron* with high accuracy and with a large basis set (e. g. on a fine spatial grid). SAE simulations have a long and successful history in strong-field physics [68, 69]. Of course, most targets have more electrons and multi-electron effects can play a significant role [70–72] and the limitations of the SAE approximation are obvious if a second electron is excited or even removed (double ionization).

One reason for the success of the SAE approximation lies in the jump of the excitation and ionization energies for the second electron once the first one is removed. Removing the first electron from a helium atom requires 24.6 eV, removing the second one from the ionized atom is much harder and requires 54.4 eV [73]. In our case this huge energy difference justifies the assumption that the second electron of the  $\text{HeH}^+$  molecular ion is tightly bound, mostly to the helium core<sup>11</sup>.

In order to set up the SAE Hamiltonian, we need to decide what the *effective* potential for the active electron should look like. Usually this potential is chosen and scaled such that important properties like the ionization potential reproduce the exact values. We discuss this issue

---

<sup>10</sup>Although it still can become infeasible very easily as shown in section 1.1.

<sup>11</sup>Of course, in the real atom both electrons are bound equally strong because they are indistinguishable. The full wave function in the SAE approximation has to be thought of as the (anti-)symmetrized product of one electron in the ground state and one electron described by the simulated wave function.

for our HeH<sup>+</sup> model in the beginning of chapter 2 and in appendix B.

- 6. Reduced dimensionality.** In order to use computational resources even more efficiently, we neglect the spatial dimensions perpendicular to the molecular axis and treat the molecule as a one-dimensional system. This means that both the nuclei and the single active electron can only move along the molecular axis which itself is fixed. Reduced-dimensionality models have a long history in strong-field simulations and the softened Coulomb potential  $(x^2 + a)^{-1/2}$  has proved useful because it has the  $1/|x|$  Coulomb tail and at the same time allows the wave function to cross the origin<sup>12</sup> [24, 76]. As a consequence of the reduced dimensionality, there are no rotational excitations of the molecule or angular-momentum levels of the electron. Since our photon energies are larger than the energy spacings of rotational eigenstates and linearly polarized light leaves the angular momentum of the electron unchanged [77], we accept both limitations. However, our model also lacks the atomic  $l$  quantum number due to the reduced dimensionality such that the number of electronic states that can be populated is decreased.

Note that we do not question that spacetime is 1 + 3 dimensional. If we did that, we should use the respective solutions to Poisson's equation for the potential of a charge distribution  $\rho$ ,  $\Delta V(x) = 4\pi\rho(x)$ , i. e.  $Cx$  (1D) or  $\ln(C/r)$  (2D) for a point charge. Obviously, these potentials have very different properties than the  $1/r$  Coulomb potential that we want to approximate.

- 7. Aligned molecules in the laser field.** Connected to the previous approximation, we assume the laser polarization axis to coincide with the molecular axis. Although this initial alignment cannot be guaranteed in an experimental setup where the molecules are randomly oriented, the coincidence measurements we compare our simulations with can be selected a posteriori for aligned or oriented molecules [78]. Also, the dissociation and ionization dynamics of HeH<sup>+</sup> is strongest if the molecule is aligned with the laser field *and* the molecule tends to align

---

<sup>12</sup>The Hamilton operator with Coulomb potential,  $p^2/2 + 1/|x|$ , is not self-adjoint and can only be defined as the orthogonal sum of the respective operators on the positive and negative half-axes [74, 75]. A hand-waving explanation is that in two or more dimensions, the particle can go around the singularity.



during the laser pulse if it has enough time [79, 80]. Even though we cannot model the alignment step, we still cover the important dynamics in the aligned state with our approximation.

Now that we have defined the playground and the region of validity for our studies, we turn on the lasers and shed light on the first of our questions in the next chapter.



## 2 HeH<sup>+</sup> in monochromatic 400nm and 800nm fields

Flash before my eyes  
Now it's time to die  
Burning in my brain  
I can feel the flame.

---

“Ride the Lightning” (Metallica), 1984

Parts of the content of this chapter have been published in [49].

In this chapter, we look at the dynamics of the aligned HeH<sup>+</sup> molecular ion in monochromatic, linearly polarized laser pulses with 400 nm or 800 nm wavelength. This “flash” of the laser can cause the target to ionize and/or dissociate, so depending on the exact parameters, the molecule is determined to “die” as soon as it feels the light. For the TDSE simulations, we employ our one-dimensional single-active-electron non-Born-Oppenheimer model that is described first before we come to physics.

### 2.1 Non-Born-Oppenheimer TDSE model

To derive the TDSE, we start with lab coordinates  $\vec{r}$  for the electron and  $\vec{R}_{\text{He}}, \vec{R}_{\text{H}}$  for the helium and hydrogen nuclei, respectively. We call the corresponding momentum operators (derivatives)  $\vec{p}_e, \vec{P}_{\text{He}}$  and  $\vec{P}_{\text{H}}$ , respectively. In length gauge, these three particles with masses 1,  $m_{\text{He}}$  and  $m_{\text{H}}$  and charges  $-1, Z_{\text{He}}$  and  $Z_{\text{H}}$  in an external electric field  $\vec{E}(t)$  are described by the Hamiltonian

$$\begin{aligned} H_{\text{lab}}(t) = & \frac{\vec{p}_e^2}{2} + \frac{\vec{P}_{\text{He}}^2}{2m_{\text{He}}} + \frac{\vec{P}_{\text{H}}^2}{2m_{\text{H}}} \\ & + V_{\text{ion}} \left( \left| \vec{R}_{\text{He}} - \vec{R}_{\text{H}} \right| \right) + V_{\text{He}} \left( \left| \vec{r} - \vec{R}_{\text{He}} \right| \right) + V_{\text{H}} \left( \left| \vec{r} - \vec{R}_{\text{H}} \right| \right) \\ & - \left( -\vec{r} + Z_{\text{He}}\vec{R}_{\text{He}} + Z_{\text{H}}\vec{R}_{\text{H}} \right) \cdot \vec{E}(t). \end{aligned} \quad (2.1)$$

## 2 $\text{HeH}^+$ in monochromatic 400nm and 800nm fields

Here,  $V_{\text{ion}}$  is the potential energy when the active electron is removed, i. e. the ground-state Born-Oppenheimer potential-energy curve of  $\text{HeH}^{2+}$ , and  $V_{\text{He}}$ ,  $V_{\text{H}}$  model the interaction between the electron and the helium or hydrogen nucleus, respectively. The inactive electron is assumed to be located at the helium core, i. e. it is included in  $m_{\text{He}}$  and  $Z_{\text{He}} = Z_{\text{H}} = 1$ .

We now perform a coordinate change into center-of-mass (c.o.m.) coordinates and coordinates relative to the nuclear center of mass,

$$\begin{aligned}\vec{R}_{\text{c.o.m.}} &:= \frac{m_{\text{He}}\vec{R}_{\text{He}} + m_{\text{H}}\vec{R}_{\text{H}} + \vec{r}}{M + 1}, \\ \vec{x} &:= \vec{r} - \frac{m_{\text{He}}\vec{R}_{\text{He}} + m_{\text{H}}\vec{R}_{\text{H}}}{M}, \\ \vec{R} &:= \vec{R}_{\text{He}} - \vec{R}_{\text{H}}.\end{aligned}$$

$M = m_{\text{He}} + m_{\text{H}}$  is the total nuclear mass (including the inactive electron). Taking into account that the corresponding momenta  $\vec{P}_{\text{c.o.m.}}$ ,  $\vec{p}$ ,  $\vec{P}$  transform as derivatives, we obtain

$$\begin{aligned}\vec{p}_e &= \vec{p} + \frac{1}{M + 1}\vec{P}_{\text{c.o.m.}}, \\ \vec{P}_{\text{He}} &= -\frac{m_{\text{He}}}{M}\vec{p} + \frac{m_{\text{He}}}{M + 1}\vec{P}_{\text{c.o.m.}} + \vec{P}, \\ \vec{P}_{\text{H}} &= -\frac{m_{\text{H}}}{M}\vec{p} + \frac{m_{\text{H}}}{M + 1}\vec{P}_{\text{c.o.m.}} - \vec{P}.\end{aligned}$$

Inserting the new coordinates and momenta into (2.1) yields

$$\begin{aligned}H_{\text{lab}}(t) &= \frac{\vec{p}_{\text{c.o.m.}}^2}{2(M + 1)} + (1 - Z_{\text{He}} - Z_{\text{H}})\vec{R}_{\text{c.o.m.}} \cdot \vec{E}(t) \\ &+ \frac{\vec{p}^2}{2\mu_e} + \frac{\vec{P}^2}{2\mu} + V_{\text{ion}}(|\vec{R}|) + V_{\text{He}}\left(\left|\vec{x} - \frac{m_{\text{H}}}{M}\vec{R}\right|\right) + V_{\text{H}}\left(\left|\vec{x} + \frac{m_{\text{He}}}{M}\vec{R}\right|\right) \\ &+ \left(\frac{M + Z_{\text{He}} + Z_{\text{H}}}{M + 1}\vec{x} + \frac{Z_{\text{H}}m_{\text{He}} - Z_{\text{He}}m_{\text{H}}}{M}\vec{R}\right) \cdot \vec{E}(t),\end{aligned}$$

where we have introduced the reduced masses  $\mu_e = M/(M + 1)$  for the electron and  $\mu = m_1 m_2 / M$  for the nuclei. As expected, the first line describing the center-of-mass motion of the charged molecule in the external field decouples from the other degrees of freedom and we can neglect it for our purposes.



If we now reduce the dimensionality for  $\vec{x}$  and  $\vec{R}$  by projecting both on the molecular axis, we end up with the main TDSE that we will use throughout this thesis:

$$i \frac{d\Psi(x, R; t)}{dt} = (H_0 + (\kappa x + \lambda R)E(t))\Psi(x, R; t) \quad (2.2)$$

with the field-free Hamiltonian

$$H_0 = \frac{p^2}{2\mu_e} + \frac{P^2}{2\mu} - \frac{Z_H}{\sqrt{(x + \frac{m_{He}}{M}R)^2 + \alpha_1(R)}} - \frac{Z_{He}}{\sqrt{(x - \frac{m_H}{M}R)^2 + \alpha_2(R)}} + V_{\text{ion}}(R). \quad (2.3)$$

Here, we have used  $\kappa = (M + Z_1 + Z_2)/(M + 1)$ ,  $\lambda = (Z_1 m_2 - Z_2 m_1)/M$  and the explicit form of the softened Coulomb potential for  $V_H$ ,  $V_{He}$ . The parameter functions  $\alpha_j(R)$  are tuned for each internuclear distance such that the two lowest Born-Oppenheimer potential energy curves (shown in figure 2.1) are reproduced exactly (cf. appendix B). Note that we only use positive values for  $R$ . This means that the helium core is located at the positive position  $x = (m_H/M)R$  and that the hydrogen core is located on the left at  $x = -(m_{He}/M)R$ .

In velocity gauge, the coupling terms are transformed into instantaneous momentum shifts by the vector potential  $A(t) = -\int^t E(t')dt'$ ,

$$H(t) = \frac{(p + \kappa A(t))^2}{2\mu_e} + \frac{(P + \lambda A(t))^2}{2\mu} + V(x, R) = T + V,$$

where  $V(x, R)$  collects the  $x$ - and  $R$ -dependent terms in (2.3). The gauge transform is given by

$$\Psi_{\text{len.}}(x, R; t) = \Psi_{\text{vel.}}(x, R; t) e^{iA(t)(\kappa x + \lambda R)}.$$

The spatial wave function is represented on a  $x$ - $R$  grid with  $N_x = 2048$  grid points in  $x$  direction (step size  $\Delta x = 0.2$  a.u., symmetric around 0) and  $N_R = 2048$  grid points in  $R$  direction (step size  $\Delta R = 0.05$  a.u., starting at 0.05 a.u.). Momentum operators act as derivatives and they are implemented using fast Fourier transforms [85]. Time evolution uses the split-operator method [86] where the short-time propagator reads

$$U(t, t + \Delta t) \approx e^{-iH(t)\Delta t} \approx e^{-iT\Delta t/2} e^{-iV\Delta t} e^{-iT\Delta t/2} + \mathcal{O}(\Delta t^3).$$

When the wave function approaches the grid boundary in  $x$  direction, it is absorbed by a complex monomial potential of fourth order which starts at

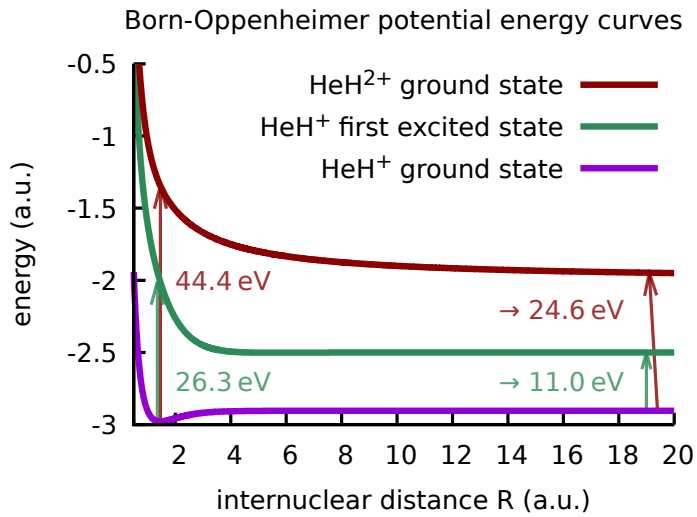


Figure 2.1: Lowest two Born-Oppenheimer potential-energy curves of  $\text{HeH}^+$  and lowest curve of  $\text{HeH}^{2+}$ . Arrows and numbers indicate the vertical excitation energy and ionization potential at equilibrium distance and asymptotically for separated nuclei, respectively. Data from [81–84], see appendix B for details.





179 a.u. distance from the nuclear center of mass<sup>1</sup>. The absorbed part is from then on propagated without electron-nuclei interaction. At the end of the time evolution, the norm squared of the absorbed part is the ionization yield and the kinetic-energy release (KER) of the ionization channel is calculated by projecting the absorbed wave function onto nuclear continuum energy eigenstates of  $\text{HeH}^{2+}$ .

The electric laser field is given by

$$E(t) = E_0 f(t) \cos(\omega t + \varphi),$$

where the envelope  $f$  with  $0 \leq f(t) \leq 1$  is either a  $\sin^2$  function or a Gaussian,  $\varphi$  is the carrier-envelope phase (CEP) and  $\omega$  is the carrier frequency of the laser. Since we use atomic units,  $\omega$  is also the photon energy. When the laser pulse duration  $T$  is specified, it means the full width at half maximum (FWHM) of the intensity, i. e.  $E(0)^2 = 2E(T)^2$  if the pulse is centered around  $t = 0$ .

## 2.2 Fragmentation pathways

Our model system has three possible outcomes of an interaction with a laser pulse: 1. The molecule stays bound; either in the initial vibrational state or in any superposition of vibrational states. 2. The molecule breaks into two fragments,  $\text{He} + \text{H}^+$  or  $\text{He}^+ + \text{H}$ , and the active electron stays bound to one of the fragments, possibly in an excited state. 3. The molecule is further ionized to  $\text{HeH}^{2+}$ , i. e. the active electron leaves the molecule. Due to the repulsive  $1/R$  potential of  $\text{HeH}^{2+}$ , ionization is always followed by rather fast dissociation (“Coulomb explosion”).

Of course, the real  $\text{HeH}^+$  has even more pathways: Double ionization comes to mind (which our single-active-electron model cannot describe) and at intensities high enough to remove both electrons from the molecule (and if the gas density is high enough), the broad field of plasma physics unfurls which is beyond the scope of this work.

Figure 2.2 shows an example result of a TDSE calculation which propagates the vibrational state  $v = 5$ ,  $v$  being the vibrational quantum number, in a 35 fs laser pulse at 800 nm wavelength. Most of the pathways described previously

---

<sup>1</sup>The complex absorbing potential (CAP) has the form  $V_{\text{CAP}}(x) = -i\alpha(|x| - x_0)^4$  for  $|x| > x_0$  with a strength parameter  $\alpha$  that is chosen depending on relevant electron momenta [87]. A typical value is  $\alpha = 10$  a.u. The offset  $x_0 = 179$  a.u. is the start of the CAP.

2  $\text{HeH}^+$  in monochromatic 400nm and 800nm fields

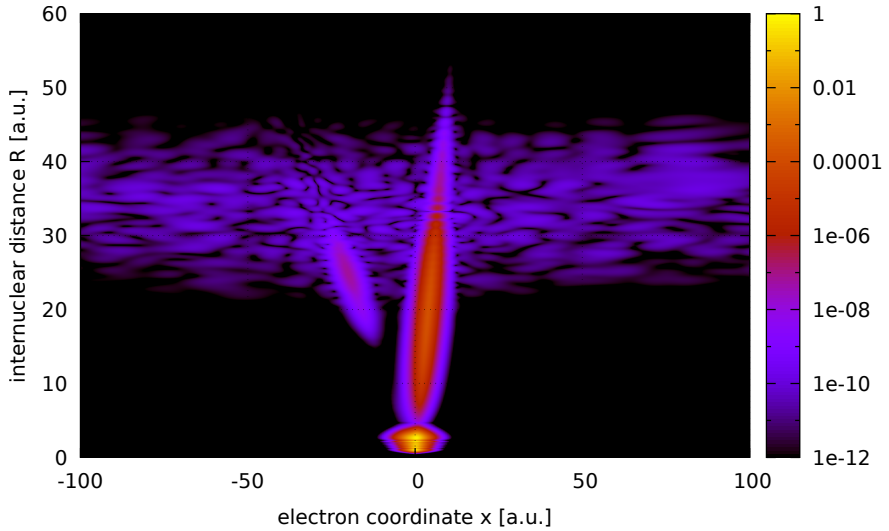


Figure 2.2: Spatial probability density  $|\Psi(x, R)|^2$  after time evolution of the  $v = 5$  initial state in a 35 fs laser pulse at 800 nm and  $5 \times 10^{13} \text{ W/cm}^2$  peak intensity.

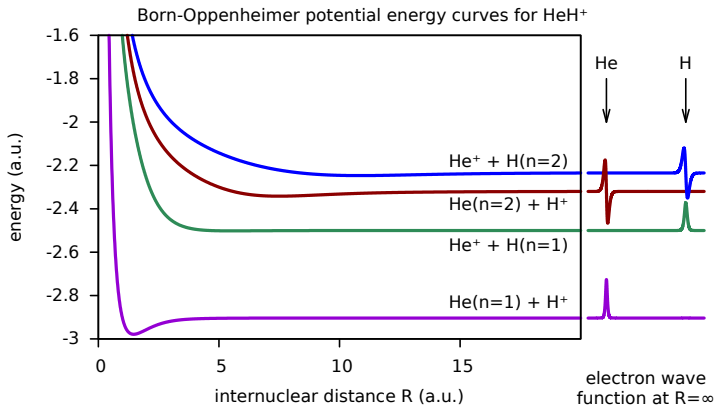


Figure 2.3: Born-Oppenheimer curves of  $\text{HeH}^+$  and  $\text{HeH}^{2+}$ , similar to figure 2.1 but calculated from our TDSE model. Asymptotic electronic states are sketched on the right; they alternate between states localized at the helium atom and states localized at the hydrogen atom.



can be seen in four features of the plot: 1. The initial state is still mostly unchanged due to the relatively small intensity of the laser pulse. It is located at low internuclear distance  $R$  at the bottom center of the plot and the five nodes of the  $v = 5$  state are visible along the  $R$  direction upon close inspection. 2. The probability along the line  $x/R = m_1/M \approx 1/5$  corresponds to the electron being located at the helium side while the molecule dissociates. The absence of nodes along the  $x$  direction indicates population of the electronic ground state, i. e. dissociation into  $\text{He} + \text{H}^+$  without electronic excitation, cf. figure 2.3, lowest curve. 3. With the same argument, the corresponding but smaller feature along the line  $x/R = -m_2/M \approx -4/5$  belongs to dissociation in the first excited electronic state into  $\text{He}^+ + \text{H}$ . 4. The structured “cloud” at  $20 \text{ a.u.} \leq R \leq 45 \text{ a.u.}$  can be attributed to Rydberg states, i. e. electronically excited states where the electron is only weakly bound and strongly delocalized. Since this Rydberg wave packet is too delocalized to contribute to the molecular bond, the molecule dissociates similarly fast as if it had been ionized. In section 2.5, we investigate the connection between ionization and Rydberg states. Note that ionization is not visible here because freed electrons move towards the absorbing boundary fast enough that they have left the main grid at the end of the time evolution. The effect of the absorbing boundary is not visible because figure 2.2 shows only a zoom into the details and does not cover the whole grid.

In our simulation, the different fragmentation channels can be analyzed individually by projecting the final wave function onto different states, namely the bound vibrational states or the electronic states at a given internuclear distance. The latter yields the vibrational wave function  $\psi_n(R)$  of the Born-Oppenheimer product wave function  $\psi_n(R)\phi_n(x; R)$ ; cf. (A.2), appendix A.

## 2.3 Kinetic-energy release

One important observable—that is also experimentally available—is the kinetic-energy release (KER). It is defined as the total kinetic energy of the nuclei in the center-of-mass (c.o.m.) frame, i. e.

$$E_{\text{KER}} = \frac{P^2}{2\mu}, \quad (2.4)$$

where  $P$  is the relative momentum of the two nuclei and  $\mu$  is the reduced mass. Momentum conservation dictates that  $P_{1,\text{c.o.m.}} = -P_{2,\text{c.o.m.}}$ , i. e. the nuclear

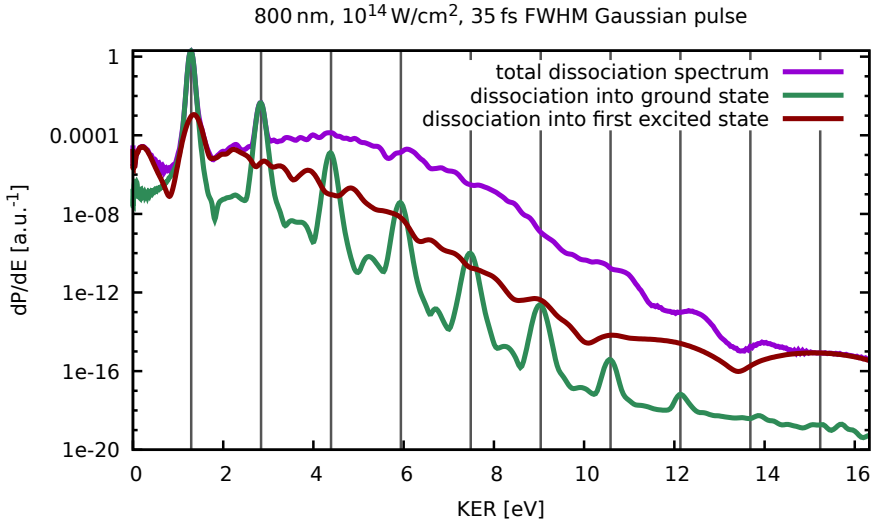


Figure 2.4: Kinetic-energy release in different channels after time evolution of the  $v = 6$  initial state in a 35 fs laser pulse at 800 nm and  $10^{14} \text{ W/cm}^2$  peak intensity.

momenta cancel each other in the center-of-mass frame and the relative momentum can be calculated from any of the two momenta,  $|P_{1,\text{c.o.m.}}| = |P_{2,\text{c.o.m.}}| = |P|/2$ .

The total dissociation KER spectrum after illumination of the  $v = 6$  initial state with a 35 fs laser pulse at 800 nm and  $10^{14} \text{ W/cm}^2$  peak intensity, shown as the violet curve in figure 2.4, has a few distinct peaks and a broad underlying structure. *Total* means that the signal contains the contributions from all bound electronic states. It is calculated by first projecting out the bound vibrational states from the final wave function, followed by a Fourier transform and integration over the electron momentum. This gives a nuclear-momentum distribution  $|\Psi(P)|^2$  which can then be transformed according to (2.4) to produce the KER spectrum. If we do the  $R$ -dependent projections onto electronic eigenstates mentioned in the previous section, it becomes clear that the ground-state contribution (green curve) consists of a series of exponentially falling peaks with a regular photon-energy spacing (1.55 eV, indicated by vertical lines). These are *above-threshold-dissociation* (ATD) peaks which have also been calculated by Ursrey et al. [44]. It is an effect similar to



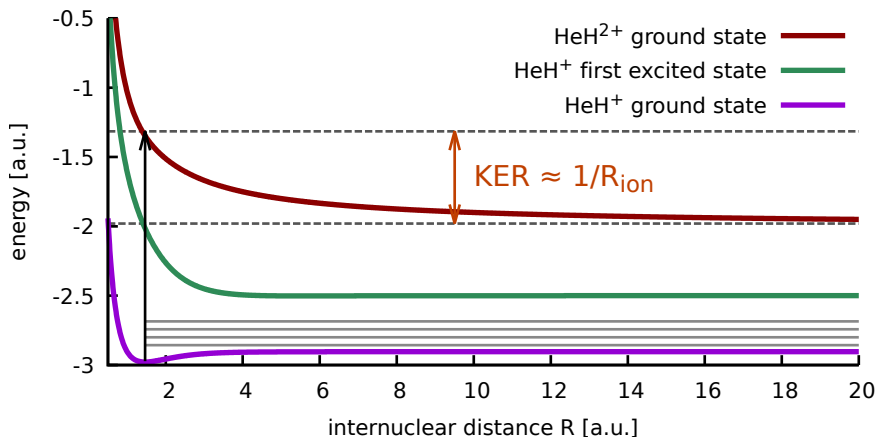


Figure 2.5: Born-Oppenheimer curves of  $\text{HeH}^+$  and  $\text{HeH}^{2+}$  like in figure 2.1. The vertical arrow indicates instantaneous ionization from the potential minimum. The dashed horizontal lines show the amount of potential energy that is converted into KER during the dissociation process that follows the ionization. Above the ground-state curve, above-threshold-dissociation energies are indicated by horizontal grey lines. They correspond to absorption of one to four 800 nm photons, starting in the  $v = 6$  state.

above-threshold ionization (ATI) in the sense that more photons are absorbed than necessary to reach the continuum. In our case, a single 800 nm photon is enough to excite the  $v = 6$  state into the dissociation continuum with excess (kinetic) energy 1.3 eV. Absorption of additional photons increase the kinetic energy of the fragments by  $\omega$  for each photon. ATD is possible and nicely visible here because there is a large energy gap to the first electronically excited state, cf. figure 2.5.

We can understand the KER spectra for the cases of electronically excited states and ionization by inspecting the Born-Oppenheimer potential-energy curves in figure 2.5. When a localized wave packet at some internuclear distance  $R_{\text{ion}}$  is instantaneously excited or ionized, it is vertically transferred to a different potential surface on which it will accelerate according to the gradient of the potential<sup>2</sup>. If the wave packet starts with zero initial velocity

<sup>2</sup>Obviously, this explanation uses both the Born-Oppenheimer approximation and a classical picture but it works well enough as we will see.

## 2 HeH<sup>+</sup> in monochromatic 400nm and 800nm fields

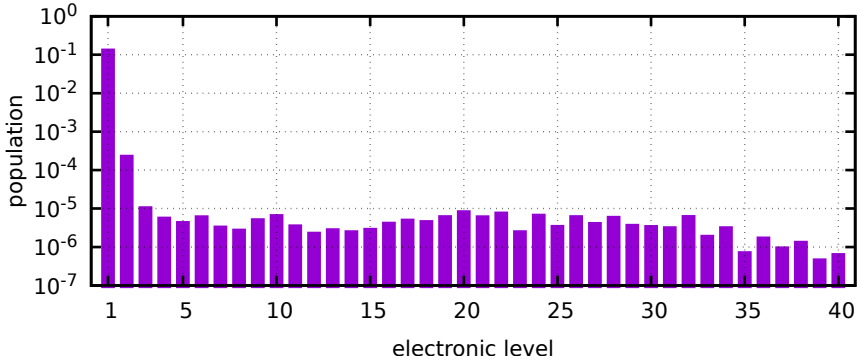


Figure 2.6: Population of electronic states at the end of the time evolution.  $n = 1$  is the electronic ground state. Initial state and laser parameters as in figure 2.4.

and is assumed to be undisturbed by the laser field for the rest of its propagation, the final kinetic energy is directly given by the change in potential energy:  $E_{\text{KER}} = V(R_{\text{ion}}) - V(\infty)$ . From the dissociative nature of practically all excited-state potential-energy curves as well as the HeH<sup>2+</sup> potential we can infer the following qualitative statement:

In the kinetic-energy-release spectrum of electronically excited or ionized states, *low* kinetic energies correspond to excitation or ionization at *large* internuclear distance and vice versa.

Going back to figure 2.4, we see that the main KER peak position of the first excited state is very similar to the first ATD peak in the ground state but slightly shifted to higher energy. The most likely pathway for this signal is that a dissociative wave packet moves on the ground-state potential curve and is partly excited to the first excited state only when the dissociative potential curve is almost flat at  $R \gtrsim 3$  a.u. We will see that indeed nuclear motion followed by electronic excitation is an important mechanism in the fragmentation of HeH<sup>+</sup>. Instead of a very small remaining deceleration on the ground-state curve the excited wave packet then experiences a small acceleration which fits the small shift of the maximum to higher energy.

Additionally, we note that neither the ground state nor the first excited state can explain the broad spectral distribution that is centered at roughly



4.3 eV. Further projections onto excited states do not reveal a single state that carries this specific KER distribution. Instead, many excited electronic states are populated and together they form the cloud in figure 2.2 and the broad spectrum with large KER in figure 2.4. This can be seen in figure 2.6. We discuss those nearly-ionized states in section 2.5.

## 2.4 Frozen-nuclei ionization and enhancement

Going one step back, we first investigate how ionization works when the nuclei *do not* move. The *frozen-nuclei approximation* is employed frequently in strong-field studies of molecules if the dynamics happen much faster than the time scale of nuclear motion [28, 88]. It is implemented by removing the kinetic-energy term for the nuclei in (2.3) or, equivalently, by setting the reduced nuclear mass  $\mu$  to infinity. This means that one still can use vibrational states with a certain nuclear distribution as initial states (as opposed to *fixed-nuclei* calculations which is often understood to mean that  $R$  is fixed at one value) but components at different nuclear coordinates do not mix and the TDSE can in principle<sup>3</sup> be solved independently for each  $R$ .

In order to calculate the internuclear-distance dependent ionization probability, we use the Born-Oppenheimer electronic ground state  $\phi_1(x; R)$  (normalized for each  $R$ ) as the initial state, cf. appendix A. Then, the  $R$ -dependent ionization probability can be calculated from the wave function at the end of the time evolution using

$$P_{\text{ion}}(R) = 1 - \int |\Psi(x, R; t_{\text{end}})|^2 dx.$$

We use a short (3 optical cycles total duration) laser pulse with  $8 \times 10^{14}$  W/cm<sup>2</sup> peak intensity and varying wavelength. The intensity is chosen so that the maximum yield in figure 2.7 is close to 1. The carrier-envelope phase  $\varphi$  is defined so that for  $\varphi = 0$  the electric-field maximum coincides with the maximum of the envelope. The electric field at this time points in the direction from hydrogen to helium.

We validate our one-dimensional model by comparing it to results from other calculations. Dehghanian et al. [45] have implemented a fixed-nuclei TDSE

---

<sup>3</sup>In practice, we use the same program code as for the non-frozen case—except for the nuclear kinetic term—and solve the TDSE for all  $R$  simultaneously.

2  $\text{HeH}^+$  in monochromatic 400nm and 800nm fields

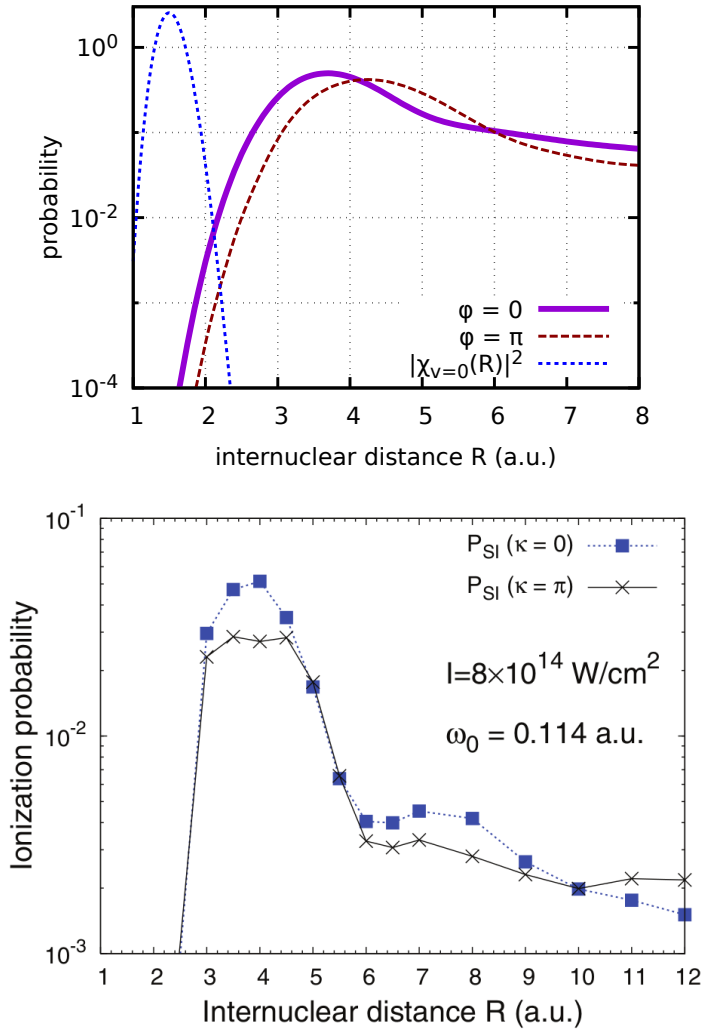


Figure 2.7: Top: Fixed-nuclei ionization probability from our 1D TDSE model in a 3-cycle 400 nm pulse with  $8 \times 10^{14} \text{ W/cm}^2$  peak intensity and CEP  $\varphi = 0$  (solid line) or  $\varphi = \pi$  (dashed line). Dotted blue line: Probability density of the vibrational ground state wave function. Bottom: Same from Dehghanian et al. [45], reproduced fig. 8(a),  $\kappa = \varphi$ .





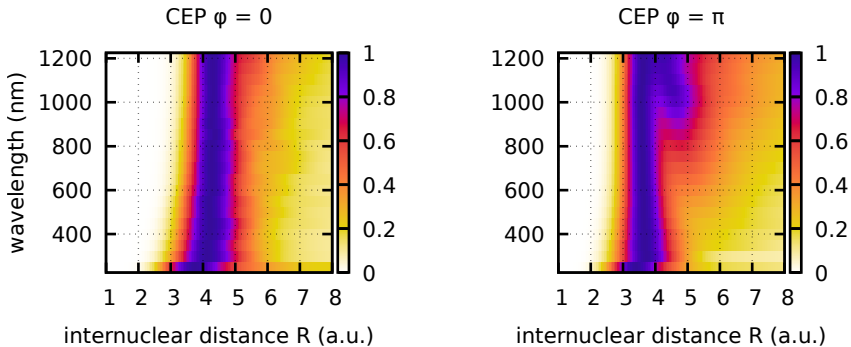


Figure 2.8: Ionization yield for fixed nuclei at internuclear distance  $R$  in a 3-cycle laser pulse with  $8 \times 10^{14}$  W/cm<sup>2</sup> peak intensity and varying wavelength. Results are normalized for each wavelength.

model for HeH<sup>+</sup> which covers the whole correlated two-electron dynamics. In figure 2.7, we compare fixed-nuclei ionization probabilities from our model (left) with results from Dehghanian, Bandrauk and Lagmago Kamta [45, 89, 90]. Both calculations are in very good qualitative agreement that the ionization probability is greatly enhanced with a peak around internuclear distance 3 a.u. to 4 a.u. compared to the equilibrium distance of 1.46 a.u. Note that this enhanced-ionization region is mostly outside the range where the low-lying vibrational states are located (represented by the vibrational ground state, blue dotted curve in figure 2.7).

The CEP shift of  $\pi$  corresponds to a sign change in the electric field or, equivalently, to a change of the orientation of the molecule. While in our results, the  $\varphi = \pi$  curve has its peak at higher  $R$ , the overall trend that  $\varphi = 0$  ionizes easier is still mostly reproduced. We will discuss the orientation-dependent ionization and dissociation in more detail in chapter 3.

One important result of [45] is that the enhancement region of the ionization probability does not depend on the wavelength of the laser pulse. We can confirm this for our model system as is shown in figure 2.8. For both  $\varphi = 0$  and  $\varphi = \pi$ , the main peak of the ionization probability stays between 3 and 4 a.u. if we vary the wavelength from the near-ultraviolet to the near-infrared. Notably, for  $\varphi = \pi$  a second peak appears for large wavelengths. Since Dehghanian et al. present results only for 200, 400 and 800 nm, it is not possible to make a

## 2 HeH<sup>+</sup> in monochromatic 400nm and 800nm fields

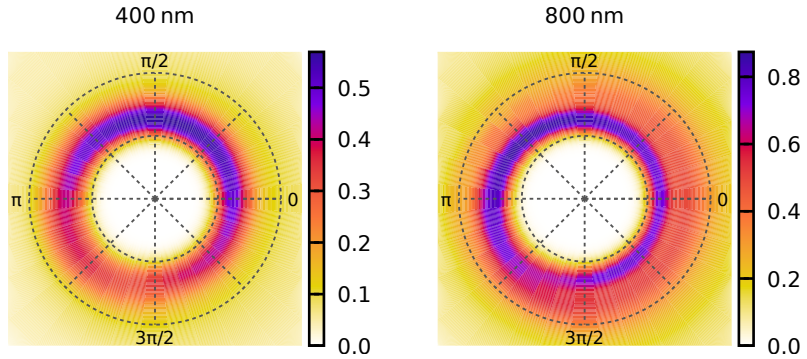


Figure 2.9: Ionization yield (colour coded) for fixed nuclei in a 3-cycle laser pulse with  $8 \times 10^{14} \text{ W/cm}^2$  peak intensity and varying carrier-envelope phase. Radially, the internuclear distance  $R$  is plotted with circles at 3 and 6 a.u.; the polar angle is the CEP  $\varphi$ .

comparison in this infrared regime.

The CEP dependence is shown in higher resolution in figure 2.9. The internuclear distance (plotted as radial coordinate) of the peak depends weakly on the CEP. More interesting is the CEP dependence of the ionization probability at the peak. For 400 nm, it is not maximal at  $\varphi = 0$  or  $\varphi = \pi$  (which would be intuitive because the maximal field strength during the laser pulse is then maximized) but rather at a phase around  $\varphi = 3\pi/8$  with a clear minimum around  $\varphi = 11\pi/8$ .

Figure 2.10 compares the time-dependent populations of the electronic ground state and the first excited state for the fixed internuclear distance  $R = 3.5 \text{ a.u.}$  and two choices of the CEP<sup>4</sup>. We see that the positive electric-field peak transfers population from the ground state into the excited state. In panel (a), this excited population is then efficiently ionized by the following negative electric-field peak. For the opposite CEP, panel (b), the main population transfer into the excited state occurs *after* the peak of the envelope. Therefore, this population cannot be ionized as efficiently and the total ionization yield is lower.

<sup>4</sup>The idea to explain the CEP-dependent ionization probability via the time-dependent population of electronic states was first presented by Bruno Schulz and Alejandro Saenz (personal communication, 6 Dec 2018).



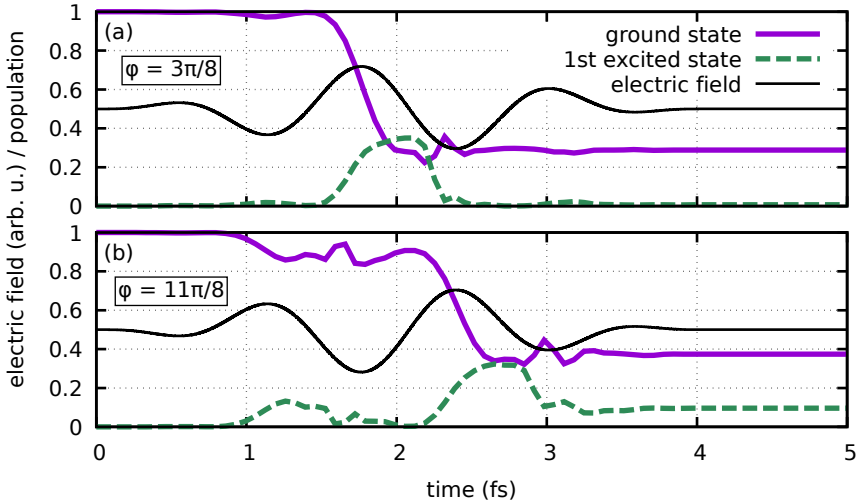


Figure 2.10: Instantaneous population of electronic states during a 3-cycle 400 nm laser pulse with  $8 \times 10^{14} \text{ W/cm}^2$  peak intensity (same as left panel of figure 2.9). Results are shown for fixed internuclear distance  $R = 3.5 \text{ a.u.}$  and the two values of the CEP  $3\pi/8$  and  $11\pi/8$  which maximize and minimize the ionization yield, respectively. The electric field (thin solid black line) in these two cases differs in the temporal order of positive and negative peaks.

The ionization probability of  $\text{HeH}^+$  depends not only on the orientation of the molecule in the laser field but for very short pulses also on their exact temporal structure.

## 2.5 Ionization and frustrated ionization

In sections 2.2 and 2.3, we have exposed  $\text{HeH}^+$  to moderate intensities which—albeit able to fragment the molecule via vibrational dissociation—do not produce significant amounts of ionization yield. We consider the opposite extreme for a moment. Figure 2.11 shows the ionization KER spectrum (i. e. the kinetic-energy release for the part of the wave function that has been absorbed at large  $x$  values because the electron has left the molecule) for different initial states and the two peak intensities  $5 \times 10^{14} \text{ W/cm}^2$  and  $5 \times 10^{15} \text{ W/cm}^2$ .

Higher-excited initial states are easier to ionize: At the lower peak intensity, the ionization yields for the initial states  $v = 5, 7, 9$  are 40.2 %, 86.5 % and 93.8 %, respectively. The  $v = 9$  state is ionized quickly for both intensities—resulting in similar KER spectra—whereas the lower states  $v = 5$  and  $v = 7$  only show a single KER peak at the lower intensity but show both more yield (more than 97 %) and more structure at the higher intensity.

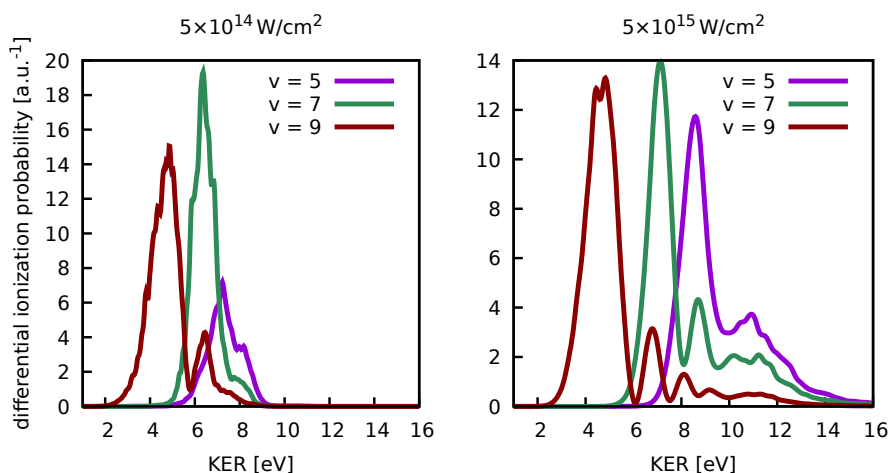


Figure 2.11: Ionization KER spectrum of  $\text{HeH}^+$  starting in different initial states using a 35 fs laser pulse at 800 nm wavelength. Left: moderate peak intensity ( $5 \times 10^{14} \text{ W/cm}^2$ ). Right: high peak intensity ( $5 \times 10^{15} \text{ W/cm}^2$ ).

The structure in the KER spectrum is a direct image of the initial spatial probability distribution: If the laser field is quick and strong enough to ionize the molecule quasi-instantaneously before any vibrational motion takes place, the whole initial wave function is lifted vertically onto the  $\text{HeH}^{2+}$  curve and is mapped to the KER axis (cf. figure 2.5). Due to the monotonic shape of the  $\text{HeH}^{2+}$  potential (approximately  $1/R$ ), this mapping can be inverted, i. e. one can reconstruct a spatial distribution at the time of ionization from the ionization KER spectrum (reflection principle [91–93]). This has been done in figure 2.12 where the overall shape of the initial wave function could be reproduced from the KER. Quick oscillations at small internuclear distance (= high ionization potential and high KER) can only be resolved with very short (3 optical cycles total duration) and very intense ( $10^{16} \text{ W/cm}^2$  peak intensity) laser



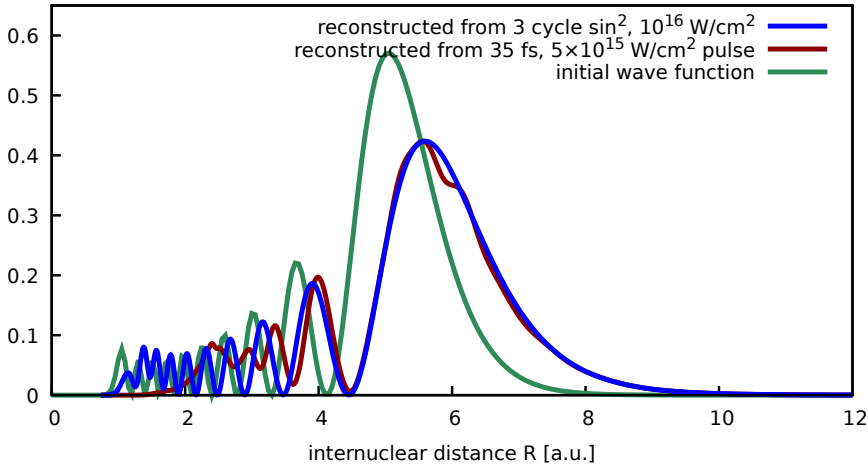


Figure 2.12: Reconstructed wave function by inverting  $E_{\text{KER}} = 1/R_{\text{ion}}$  for two different laser pulses (blue and red curve) together with the actual initial  $v = 10$  state.

pulses. We see that the peak positions do not match exactly. This corresponds to an energy offset which may occur if the instantaneous kinetic energy is used as the KER at some time after the laser pulse and the wave packet gains a bit more energy afterwards.

In figure 2.2 we have already seen that the laser pulse produces states where the electron is bound but delocalised and the molecule rapidly dissociates. The KER of this dissociation channel is similar to the ionization KER because both processes actually start with ionization which immediately launches Coulomb explosion on the  $1/R$  potential curve of  $\text{HeH}^{2+}$ . However, the freed electron can be recaptured in an excited state. Nubbemeyer et al. [94] have shown that this happens upon recollision of the photoelectron with the ionized molecule (or atom in their case) and they dubbed this process *frustrated tunnel ionization* (FTI). Even though the Rydberg states have a small ionization potential (binding energy), their population *increases* with increasing intensity of the laser pulse. The KER of frustrated tunnel ionization has been measured by the same group during double-ionization experiments on  $\text{H}_2$  [95]. They observed the same general effect—FTI at similar KER as in ionization—as in our  $\text{HeH}^+$  simulations.

As a summary of the effects discussed above (ATD, FTI and ionization KER), figure 2.13 shows the KER spectrum in linear scale for both dissociation and

2  $\text{HeH}^+$  in monochromatic 400nm and 800nm fields

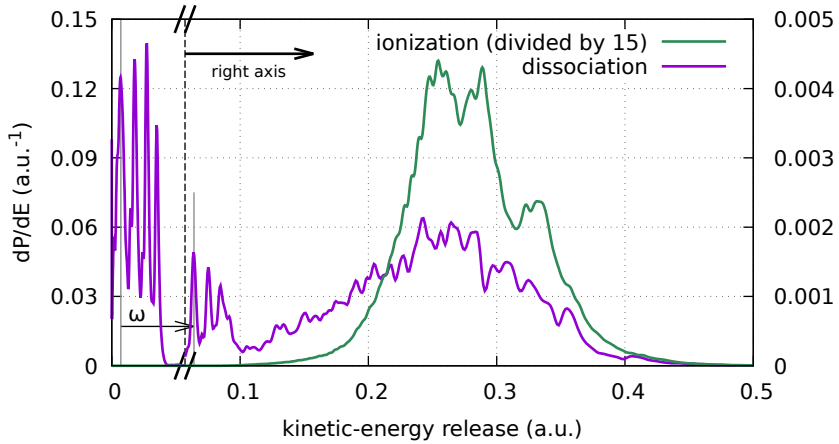


Figure 2.13: Kinetic-energy release for the dissociation and the ionization channel after a 35 fs laser pulse at 800 nm wavelength and  $5 \times 10^{14} \text{ W/cm}^2$  peak intensity. Results for vibrational states  $v = 0 \dots 4$  are incoherently summed up using the weights from table 2.1. The photon-energy spacing  $\omega$  between ATD peaks is indicated by an arrow. The plot is split in two: The first set of peaks uses the left vertical axis. Everything right of the vertical dashed line ( $\text{KER} > \omega$ ) is scaled and uses the right vertical axis. Additionally, the ionization spectrum has been scaled down.



ionization. Here, we assume a mixture of vibrational states as the initial states and sum the results incoherently using the weights from table 2.1 on page 37 which resemble the experimental distribution of initial states, cf. section 2.9. Due to the mixture of initial states, we see not only one ATD peak with  $\text{KER} < \omega$  but one for each vibrational state<sup>5</sup>. There is another set of peaks shifted up in energy by one photon energy. Note that in the right part of the plot the vertical axis is scaled.

The position of the broad peak in the dissociation signal at large KER agrees with the position of the ionization KER. This is the FTI signal described above which is composed of many excited electronic states, cf. figure 2.6. Depending on the electronic state and the internuclear distance where the electron has been recaptured, the KER can be reduced compared to the case where no recapturing occurs. Therefore, the FTI peak is broader towards smaller energies.

## 2.6 Application of the $\text{HeH}^+$ model to $\text{H}_2^+$

Before we come to more unique features of  $\text{HeH}^+$ , we apply our TDSE model to probably the most prominent benchmark molecule in strong-field physics: the dihydrogen cation  $\text{H}_2^+$ . In some aspects  $\text{H}_2^+$  is very similar to our model system. It is a diatomic molecule, it has one active electron (but in  $\text{H}_2^+$  this is no approximation) and it carries a permanent charge. Due to its symmetry, however, the structure of the electronic spectrum is quite different. While in  $\text{HeH}^+$  the electron is localized at the helium and hydrogen side in the ground and the excited state, respectively, the two lowest electronic states of  $\text{H}_2^+$  are anti-symmetric and symmetric states, respectively, with equal probability on both sides. For this reason, the two lowest Born-Oppenheimer potential-energy curves shown in figure 2.14 are asymptotically degenerate in contrast to the  $\text{HeH}^+$  case where there is a relatively large energy gap between the two curves.

Our TDSE model (2.3) can be used for  $\text{H}_2^+$  by setting  $\alpha_1(R) = \alpha_2(R)$  and optimizing this function so that the Born-Oppenheimer ground-state-energy curve matches the correct one, similar to appendix B. Feuerstein and Thumm [97] use a similar potential but they introduce a second parameter which

---

<sup>5</sup>Except for the ground state: Two photons are necessary to excite  $v = 0$  into the continuum (only one for the other states). The peak is at 0.046 a.u. but it is not visible in linear scale.

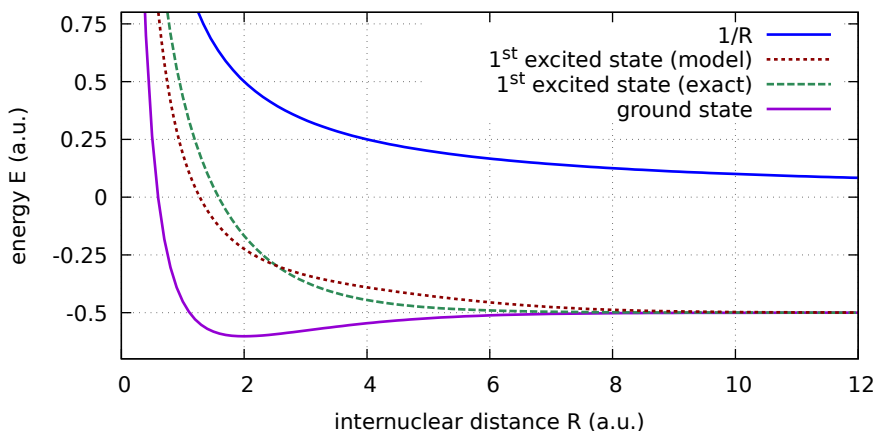
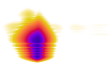


Figure 2.14: Two lowest Born-Oppenheimer potential-energy curves of  $\text{H}_2^+$  and the potential curve  $1/R$  of the ionized system  $\text{H}_2^{2+}$ . The excited-state energies in the model (red dotted curve) cannot reproduce the exact values (green dashed curve) exactly. Data points from [96].

allows them to also better reproduce the first excited state. Figure 2.14 displays the mismatch of excited-state energies that our model produces.

The comparison of  $\text{H}_2^+$  KER spectra is shown in figure 2.15. Due to the slightly different potentials no exact agreement can be expected. We can, however, see that the main features from Feuerstein and Thumm are also visible in our results: Two dissociation peaks at low KER around 1 eV and 2 eV and one broad ionization KER signal which peaks around 6 eV. One obvious difference is the contribution to the dissociation KER spectrum which has similar energy as the ionization signal. Of course, this is the already known frustrated tunnel ionization, i. e. bound but highly excited electronic states which dissociate quickly. It is completely absent in the right plots because in Feuerstein and Thumm's calculation, the absorbing boundary in the electron coordinate starts already at 25 a.u. distance from the nuclear center of mass. Therefore, practically the whole FTI signal is absorbed and counts as additional ionization in their calculation. We see that increasing computational capabilities—here in form of larger grid sizes—can sometimes uncover physical effects without changing the model significantly.

Note that the low-energy dissociation signal in our model is dominated by





the ground state whereas it is likely (they do not explicitly analyse it) that one of the peaks in Feuerstein and Thumm's spectrum corresponds to the excited state. This can be caused by the distorted shape of the excited-state potential-energy curve which is above the exact values in the relevant transition region, i. e. resonant transitions are only possible at larger internuclear distance.

Since our model has lost the ability to exactly reproduce not only one but two electronic states due to the symmetry requirement  $\alpha_1 = \alpha_2$ , it is not likely to produce relevant results for  $\text{H}_2^+$  where more advanced models are available [98–101]. Instead, we will now return to  $\text{HeH}^+$ .

## 2.7 Strong-field experiments on $\text{HeH}^+$

Before going to the next results, we have a brief look at the experimental setup that has been used to produce some of the data. The collaboration with the experimental group of Prof. Gerhard Paulus in Jena was part of the QUTIF programme<sup>6</sup>. The measurements have been carried out mainly by Philipp Wustelt and are described in much more detail in his PhD thesis [78] and the publications [49, 102, 103].

Figure 2.16 shows schematically the experimental setup. The starting point is the ion source where hot  $\text{HeH}^+$  molecular ions are formed in a duoplasmatron from a mixture of helium and hydrogen gas. Actually, many different ions and molecules are created in the source. Therefore, the accelerated ion beam needs to be filtered with respect to the charge state and the mass-to-charge ratio using a Wien filter before it is shaped with einzel lenses and deflector plates. In the interaction region, the ion beam crosses the focus of the laser pulse. We do not study the details of the laser system here. Instead, the pulse parameters are given for each experimental result that we discuss. It is, however, important to point out that there is a *phase meter* in the beam line (not shown) which measures the carrier-envelope-phase for every single laser shot and allows for phase tagging instead of phase stabilization [102]. In the detector region, fragments with different mass-to-charge ratio are separated by electric field and coincidence measurements of the time of flight and the position on the detector screen of all charged fragments are done for every single shot. In principle, this allows to capture the whole 3D momentum for all involved

---

<sup>6</sup>QUTIF stands for **Q**uantum **D**ynamics in **T**ailored **I**ntense **F**ields and was a priority programme (2015–2022) funded by the German Research Foundation DFG.

2  $\text{HeH}^+$  in monochromatic 400nm and 800nm fields

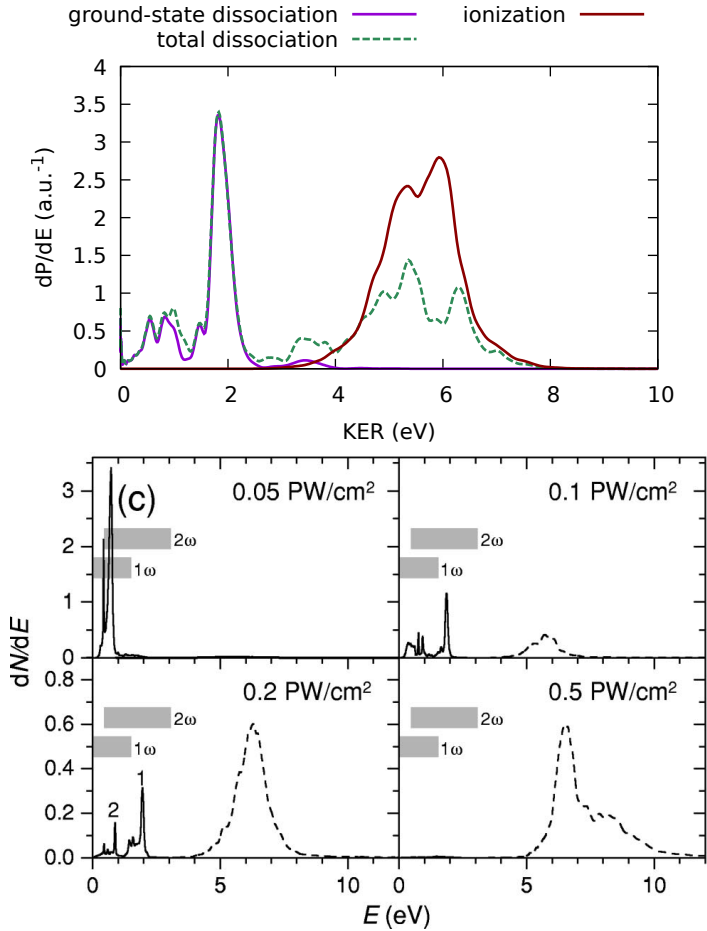
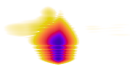


Figure 2.15: Kinetic-energy release of  $\text{H}_2^+$  after a 25 fs pulse with 800 nm wavelength. Left: Calculation with our model at  $2 \times 10^{14} \text{ W}/\text{cm}^2$  peak intensity. Shown are the ionization channel as well as the total dissociation spectrum (including FTI) and the spectrum of the dissociating part in the electronic ground state. Right: Calculations from Feuerstein and Thumm [97, fig. 4] at four peak intensities. Solid lines: dissociation; dashed lines: ionization.



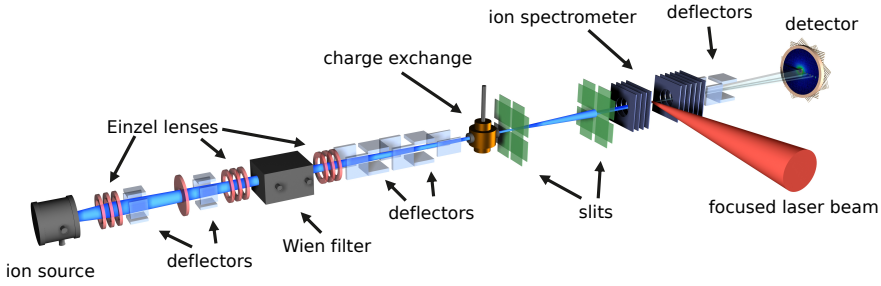


Figure 2.16: Schematic view of the experimental setup. Translated fig 3.1 from [78].

particles.

Experimental difficulties are mostly induced by the low event rate of 0.01 Hz to 10 Hz which is due to the low particle density of the ion beam ( $\approx 10^5 \text{ cm}^{-3}$ , similar to the background gas at  $10^{-10} \text{ mbar}$ ) [78]. Long measurement times which require good stability of all components are the consequence and one reason why there are not many strong-field experiments on  $\text{HeH}^+$ .

## 2.8 Focal-volume / intensity averaging

In our simulations, we always consider a single molecule in an exactly defined laser pulse. In reality, however, the ion beam as well as the laser beam has a certain shape and extent. Depending on the position within the laser-beam profile, the peak intensity varies by orders of magnitude and the measurement collects results from all targets within the focal volume. Therefore, focal-volume—or intensity—averaging has to be applied to simulation results in order to make them comparable to experimental measurement data.

In a Gaussian laser beam, the intensity depends on the radial distance  $r$  from the laser propagation axis as

$$I(r, z) = I_0 \left( \frac{w_0}{w(z)} \right)^2 \exp \left( \frac{-2r^2}{w(z)^2} \right), \quad w(z) = w_0 \sqrt{1 + \left( \frac{z}{z_R} \right)^2}$$

where  $z$  is the distance in propagation direction from the focal point,  $w(z)$  is the waist radius at distance  $z$ ,  $w_0 = w(0)$  and  $z_R = \pi w_0^2 / \lambda$  is the Rayleigh

length.

If an ion beam and a laser beam are crossed vertically, the relevant (involved) focal volume depends on the relative size of both: If the ion beam is very thin compared to  $w(z)$ , the focal volume can be approximated by a line and focal-volume averaging is a one-dimensional integral. If the ion beam radius is large compared to  $w(z)$  but much smaller than the Rayleigh length  $z_R$ , then  $w(z)$  is approximately constant along the ion beam and a two-dimensional integral over a cut through the beam profile provides the focal-volume average. If, however, the target extends over a large region relative to the laser-beam sizes  $w_0$  and  $z_R$ , the full three-dimensional intensity profile of the laser field has to be taken into account.

For all three cases, the volume function  $V(I_0, I)$ —i. e. the volume where the intensity is between  $I$  and  $I_0$ —has been calculated by Wang et al. [104]. The focal-volume averaged spectrum  $S(I_0)$  of some intensity-dependent probability  $P(I)$  is given by<sup>7</sup>

$$S(I_0) = \int_V P(I(\vec{x})) d^N \vec{x} = \int_0^{I_0} P(I) \left[ -\frac{\partial V(I_0, I)}{\partial I} \right] dI. \quad (2.5)$$

In our case, the ion beam radius of approximately  $200 \mu\text{m}$  is smaller than the Rayleigh length of roughly  $400 \mu\text{m}$  at  $800 \text{ nm}$  or  $800 \mu\text{m}$  at  $400 \text{ nm}$  and larger than the focus waist size of  $10 \mu\text{m}$  [78]. Therefore, it is most appropriate to use the 2D formula and (2.5) reduces (up to normalization) to

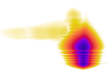
$$S_{2D}(I_0) \sim \int_0^{I_0} \frac{P(I)}{I} dI. \quad (2.6)$$

Whenever we show intensity-averaged results, we use this two-dimensional focal-volume averaging.

Note that due to the large volume with low intensity, there are many more targets that interact with low-intensity pulses than targets that experience the highest intensities. This is reflected in (2.6) by the  $1/I$  term. For that reason, often the low or intermediate intensities are more representative for focal-volume averaged properties than results obtained at the peak intensity.

Some strong-field effects like harmonic generation rely on the interplay of macroscopically separated targets within the laser focal volume. In this case, phase matching is crucial [105, 106] and it is not sufficient to simply sum

<sup>7</sup>Compare eq. (1) in [104].



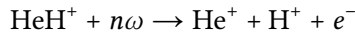
$v$	0	1	2	3	4	5	6
HeH <sup>+</sup>	0.55	0.23	0.11	0.07	0.04		
HeD <sup>+</sup>	0.436	0.238	0.136	0.0814	0.0513	0.0339	0.0236

Table 2.1: Initial population of vibrational states after preparing the molecules in the ion source. HeH<sup>+</sup> values reproduced Table I from [107]. HeD<sup>+</sup> calculated by assuming the same energy distribution.

results from all targets incoherently. For comparison with our experimental setup, incoherent integration over the focal volume is correct because the low event rate and the single-shot coincidence measurement setup mean that each detector signal comes exactly from one target. Even if multiple targets interact with a single laser pulse they are not in a coherent state.

## 2.9 Intensity dependence of ionization KER

We continue this chapter with some joint experimental and simulation results that have been published in [49]. Figure 2.17 shows the kinetic-energy release of the ionization channel



using an 800 nm laser pulse with 35 fs FWHM pulse duration and varying peak intensity. The simulation results are focal-volume averaged and include contributions from multiple initial vibrational states with weights according to Loreau et al. [107] which are given in table 2.1. For each peak intensity, the results are normalized so that the highest color value in each horizontal line is 1.

Starting with the highest peak intensity, we see the KER spectrum centered around 10 eV to 12 eV in figure 2.17. The corresponding internuclear distance  $R$  at the time of ionization (cf. section 2.3)—printed on the upper axis—is between 2 a.u. and 3 a.u. We can conclude that the high-intensity pulse ionizes the molecule mostly at internuclear distances which are relatively close to the equilibrium distance of 1.46 a.u. Albeit similar to the imaging of the vibrational wave function seen in figure 2.12, the longer pulse duration, the focal-volume averaging and the vibrational averaging prevent us from seeing any vibrational structure here.

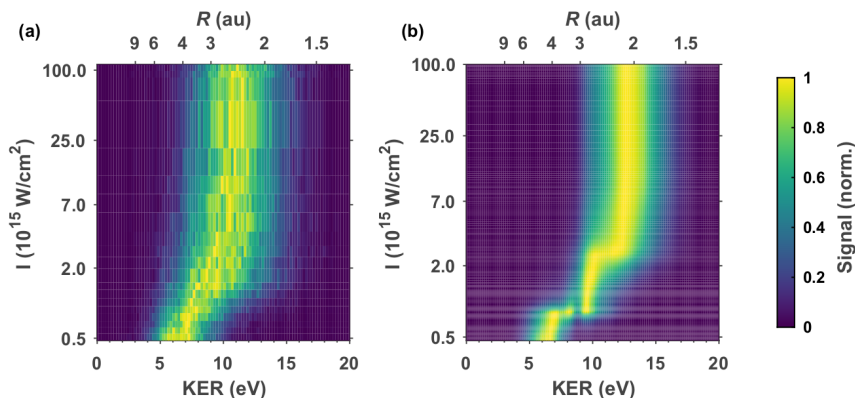


Figure 2.17: Intensity dependence of ionization KER spectrum after irradiating  $\text{HeH}^+$  with a 35 fs laser pulse at 800 nm wavelength. Left: measurement; right: focal-volume and vibrationally averaged simulation results. Reproduced fig. 6.6 from [78].

When the intensity is decreased, the KER decreases in several steps. The first step—where the KER goes down from 11.5 eV to 10 eV in the simulation results—can be attributed to a change of the dominantly ionized vibrational state: At high intensity, the lowest vibrational state can be ionized and it dominates the ionization signal due to its 55% of the population. The first excited state has a vibrational wave function which facilitates more efficient ionization at larger internuclear distance (cf. section 2.4) and thus can exceed the ground-state peak in the KER spectrum if the intensity is small enough (mind the normalization).

The second jump at lowest intensities (indicated by the arrows), however, cannot be explained by the vibrational mixture. Instead, the high-lying vibrational states of  $\text{HeH}^+$  are excited by absorption of a single 800 nm photon whereby vibrational wave-packet motion up to  $R = 7$  a.u. is initiated. At these large internuclear distances, ionization is much easier and, thus, also possible at low intensities.

The vibrational population at the end of the laser pulse can be extracted from single TDSE calculations; it is plotted in figure 2.18 for three cases. Especially at low intensity, a distinct excitation peak around  $v = 7$  is visible which fits the 800 nm resonance. In contrast, the states closest to the initial state,  $v = 1 \dots 4$ ,



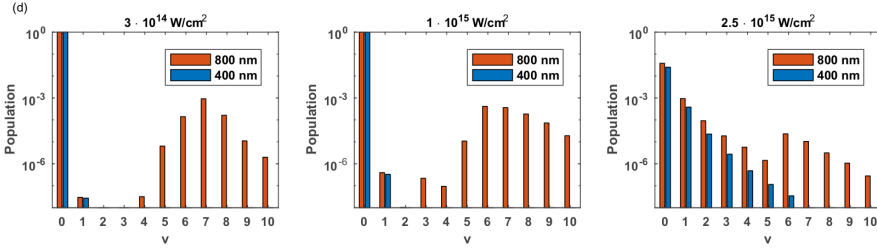


Figure 2.18: Population of vibrational states at the end of the time evolution. The  $v = 0$  initial state is exposed to a 400 nm (blue) or 800 nm (orange) laser pulse with peak intensity  $3 \times 10^{14} \text{ W/cm}^2$ ,  $1 \times 10^{15} \text{ W/cm}^2$  or  $2.5 \times 10^{15} \text{ W/cm}^2$  (from left to right). Reproduced fig. 6.9(d) from [78].

are hardly populated. With increasing field strength, non-resonant excitation of neighbouring states takes place.

The same measurements and simulations have been done with slightly longer (50 fs) 400 nm laser pulses. The results are plotted in figure 2.19. In contrast to the 800 nm results, we only see one significant transition to lower KER when the intensity is decreased. As before, it corresponds to the declining contribution of the  $v = 0$  state such that the  $v = 1$  KER at about 10 eV dominates the signal. In the simulation results, it is very clear that the jump to even lower KER is completely absent.

This is because the 400 nm field cannot drive any vibrational transitions efficiently since already a single photon has enough energy to dissociate the molecule. This also shows that the vibrational population of  $v \geq 2$  in figure 2.18 does not come from the *Lochfraß* effect. *Lochfraß* is the initiation of vibrational wave-packet motion via uneven ionization of an initial state [108]. Indeed, the ionization probability highly depends on the internuclear distance (similar for both 800 nm and 400 nm laser pulses) and vibrational excitation via *Lochfraß* is possible. However, the comparison between the two results shows that the direct vibrational excitation has a much stronger effect on the ionization KER. *Lochfraß* populates mostly the neighbouring state(s) [108], i. e. the small population of the  $v = 1$  state at  $3 \times 10^{14} \text{ W/cm}^2$  in figure 2.18 likely can be attributed to *Lochfraß*.

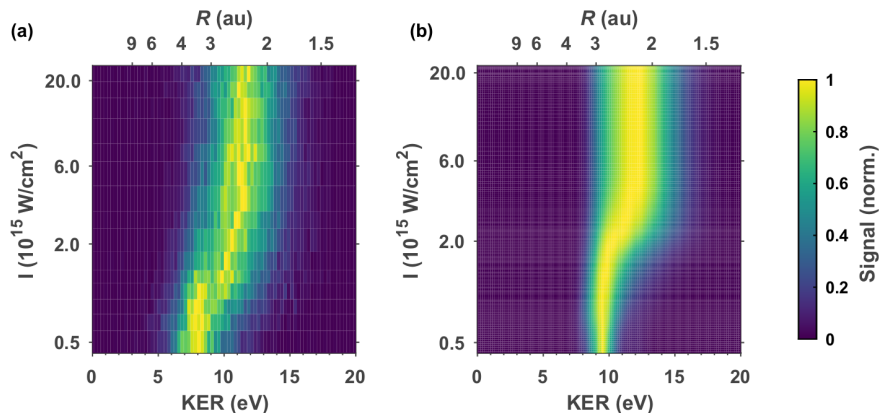


Figure 2.19: Intensity dependence of ionization KER spectrum after irradiating  $\text{HeH}^+$  with a 50 fs laser pulse at 400 nm wavelength. Left: measurement; right: focal-volume and vibrationally averaged simulation results. Reproduced fig. 6.8 (a-b) from [78].

## 2.10 Ionization of $\text{HeD}^+$

Since vibrational excitation plays an important role for the ionization process, we will now investigate isotope effects which manifest primarily in the vibrational dynamics. The heavier isotopologue  $\text{HeD}^+$  has a larger reduced mass (2442 a.u. compared to 1467 a.u. for  $\text{HeH}^+$ ) which causes it to move slower and have different vibrational states. The energies of the bound vibrational states are deeper inside the potential well and their spacing is smaller than for  $\text{HeH}^+$ . Therefore, it does not make sense to use the same vibrational population for the initial distribution. Instead, the  $\text{HeH}^+$  population is interpolated as a function of the vibrational energies and evaluated at the  $\text{HeD}^+$  eigenenergies. This produces the values listed for  $\text{HeD}^+$  in table 2.1.

Using these weights, we compare the vibrationally averaged ionization KER spectra for  $\text{HeH}^+$  and  $\text{HeD}^+$ . We omit the intensity averaging—which can smear out and obscure effects—and show results for two single intensities  $10^{14} \text{ W/cm}^2$  and  $5 \times 10^{14} \text{ W/cm}^2$  in figure 2.20 (a) and (b), respectively.

For the smaller intensity, both isotopologues produce very similar KER spectra. Note, however, that the  $\text{HeH}^+$  result has been scaled down by a factor of 30 in order to be of the same magnitude as the  $\text{HeD}^+$  signal! The KER





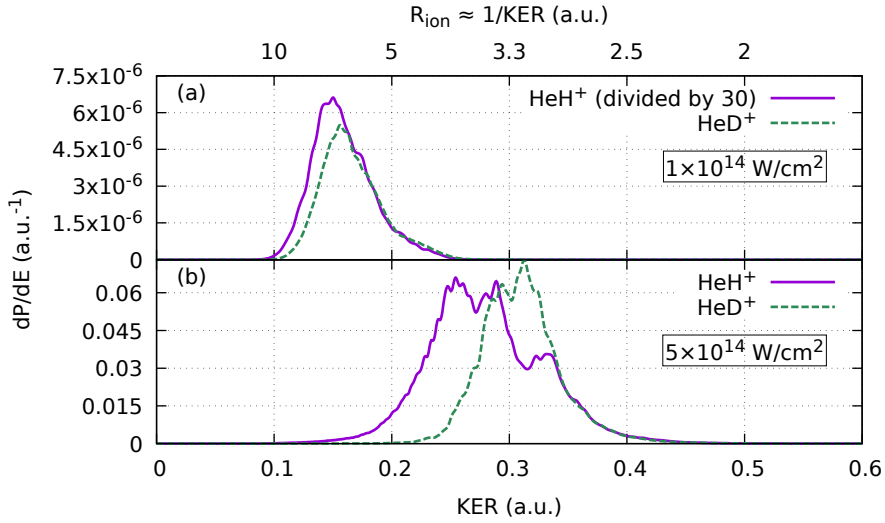


Figure 2.20: Ionization KER spectrum for vibrationally averaged HeH<sup>+</sup> and HeD<sup>+</sup> at intensities  $10^{14} \text{ W/cm}^2$  (a) and  $5 \times 10^{14} \text{ W/cm}^2$  (b) of a 35 fs laser pulse at 800 nm wavelength. In (a), the HeH<sup>+</sup> spectrum has been divided by 30 for better comparability. The weights for vibrational averaging are given in table 2.1. The scale on the top translates KER into internuclear distance at the time of ionization via the approximate  $1/R$  relation of the HeH<sup>2+</sup> BO potential-energy curve.

spectrum is centered at small KER which correspond to large internuclear distance at the time of ionization. This is in agreement with our previous findings regarding the KER spectrum at small intensities. Since the 800 nm field can drive vibrational transitions, it is likely that the slower motion of  $\text{HeD}^+$  towards the enhanced-ionization region at larger  $R$  causes the substantially reduced probability compared to  $\text{HeH}^+$ .

In panel (b) where we increase the intensity to  $5 \times 10^{14} \text{ W/cm}^2$ , both isotopologues have roughly similar yields (no scaling required). Here, it is obvious that the  $\text{HeH}^+$  spectrum is much broader towards smaller KER, again indicating quicker motion of the nuclei before the ionization process.

We conclude that the ability to reach larger internuclear distances quickly during the laser pulse influences the ionization probability significantly.  $\text{HeD}^+$  is heavier and slower and thus less likely to ionize.

## 2.11 Conclusion

Ionization of  $\text{HeH}^+$  is highly dependent on the internuclear distance and thus nuclear motion and electron removal are strongly linked. In contrast to symmetric molecules such as  $\text{H}_2^+$ , it is possible to directly drive vibrational transitions in  $\text{HeH}^+$  using a near-infrared or infrared field which can also ionize the molecule. In this case, the vibrational and electronic degrees of freedom must be treated together in order to cover the whole dynamics. If we switch from 800 nm to 400 nm light, all vibrational transitions are non-resonant and the dependence of the ionization yield on the nuclear configuration is mostly reduced to the mixture of initial vibrational states.

The effect of varying the nuclear masses is now quite intuitive: Heavier isotopologues (larger reduced mass) move slower, therefore the enhancement effect of vibrational excitation on the ionization yield is smaller because the favoured internuclear distances are reached later during or even after the laser pulse.

We have seen here that by using a suitable laser pulse—actually just something that can drive vibrational excitations—we can stimulate both nuclear motion and (subsequently) ionization. The next logical step is to control ionization and dissociation independently.



## 3 Two-color dissociation vs. ionization control at 1380nm

Why do two colors, put one next to the other, sing? Can one really explain this? No. Just as one can never learn how to paint.

---

Pablo Picasso

Whereas in the previous chapter we have mostly used simple monochromatic laser pulses without any special properties (except for some being very short), in this chapter we expose  $\text{HeH}^+$  to  $\omega$ - $2\omega$  (two-color) fields which provide an easily tunable directional asymmetry. This allows us to exploit the asymmetry of the molecule and, as a consequence, to steer the fragmentation process into one or the other fragmentation channel. If not noted otherwise, all calculations in this chapter start in the vibrational ground state  $v = 0$ .

In the following, we first describe the exact laser pulse. Then, the main results using the non-Born-Oppenheimer TDSE model and focal-volume averaging are presented as they have been published in [53], followed by in-depth analyses of the relevant effects and mechanisms.

### 3.1 Tailored fields

We have already seen in section 2.4 that for short laser pulses the direction of the main electric-field maximum (pointing from helium to hydrogen or vice versa) can have a huge effect on the ionization probability. More generally, the asymmetric  $\text{HeH}^+$  molecule is obviously sensitive to the asymmetry of the laser pulse.

Long monochromatic laser pulses are relatively symmetric; only by decreasing the pulse duration the carrier-envelope-phase (CEP) dependence and asymmetry of the laser pulse come into play. However, there are more ways to shape laser pulses. One of the easiest implementations of *tailored fields*—and

### 3 Two-color dissociation vs. ionization control at 1380nm

the method that we will employ—are collinearly polarized two-color pulses. They have been used for several decades for controlling the breakup of atoms and molecules in strong laser fields [109–111] and for studying electron trajectories [112–118].

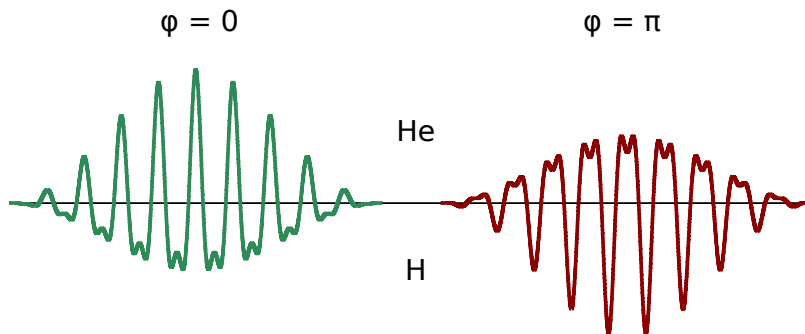


Figure 3.1: Examples of two-color laser pulses with 1380 nm fundamental wavelength and 690 nm second harmonic with intensity ratio 5:1 and 10 cycles  $\sin^2$  envelope.  $\varphi$  is the CEP of the second harmonic. In the left panel ( $\varphi = 0$ ), the positive electric-field maxima are increased by the second harmonic. This electric-field direction points from hydrogen to helium. In the right panel ( $\varphi = \pi$ ), the orientation is essentially reversed. Positive electric fields point from hydrogen to helium.

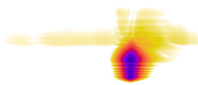
Explicitly, the laser pulse is polarized along the molecular axis and its electric field strength is given by  $E(t) = E_\omega(t) + E_{2\omega}(t; \varphi)$  where

$$\begin{aligned} E_\omega(t) &= E_\omega^0 \sin^2(\pi t/\tau) \cos(\omega(t - \tau/2)), \\ E_{2\omega}(t; \varphi) &= E_{2\omega}^0 \sin^2(\pi t/\tau) \cos(2\omega(t - \tau/2) + \varphi). \end{aligned} \quad (3.1)$$

Here,  $\tau$  is the full duration of the laser pulse<sup>1</sup> and  $E(t) = 0$  for  $t < 0$  and for  $t > \tau$ . The relation to the full width at half maximum (FWHM)  $T$  of the intensity envelope reads

$$T = \tau \left( 1 - \frac{2}{\pi} \arcsin(2^{-1/4}) \right) \approx 0.36\tau.$$

<sup>1</sup>Later, we will use laser pulses where  $E_\omega$  and  $E_{2\omega}$  have different pulse durations. They are defined analogously.



All intensity values in this chapter refer to the peak intensity of the fundamental pulse alone. Note that we use the CEP  $\varphi$  of the  $2\omega$  field for controlling the relative phase of the two colors. Another option would be to introduce a variable delay between the two pulses—this is easier to implement experimentally. For pulses that are long enough and for small delays ( $\pm$  one optical cycle), the resulting electric fields are similar in both cases and we resort to the relative-phase control because it has the advantage that it produces exactly periodic results.

Figure 3.1 shows example fields for two opposite choices of  $\varphi$ . It can be seen that although the second field is much weaker (intensity ratio 5:1),  $E(t)$  has a significant directional asymmetry. The nonlinearity of strong-field processes amplifies this asymmetry even further.

The CEP-controlled three-cycle pulses used in section 2.4 feature a particular time dependence in the time-asymmetric cases  $\varphi \neq n\pi$ ,  $n \in \mathbb{Z}$  (in the sense that a certain temporal order of a strong and a weak field maximum occurs, depending on  $\varphi$ ). Due to the longer duration and the smaller slope of the envelope, this effect is much weaker in our two-color field (3.1). The cases of CEP  $\varphi$  and CEP  $-\varphi$  differ mostly in the slope of the rising vs. falling edge of individual half-cycles. The main effect, however, is the change of preferred direction from positive to negative. The preferred direction takes extreme values at  $\varphi = 0$  and  $\varphi = \pi$  and is symmetric around these values. We can thus expect our observables—e. g. ionization or dissociation yields—to be symmetric around  $\varphi = 0$ , too.

## 3.2 Non-Born-Oppenheimer and focal-volume-averaged results

We use the non-Born-Oppenheimer model as described in section 2.1 and start by presenting results that aim at being comparable to measurement data. To this end, we consider two-color fields with parameters that are supposed to be experimentally feasible: 50 fs FWHM pulse duration for the fundamental 1380 nm field and a slightly longer 60 fs pulse using the second harmonic at 690 nm. Also, we use focal-volume averaging (FVA) as described in section 2.8. Figure 3.2 shows the probabilities for ionization and for dissociation into the ground state as a function of the relative phase  $\varphi$ .

Both the ionization yield and the dissociation yield show a  $2\pi$ -periodic

### 3 Two-color dissociation vs. ionization control at 1380nm

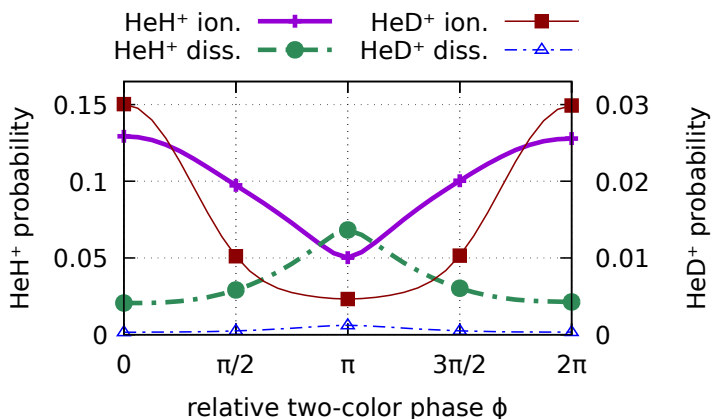


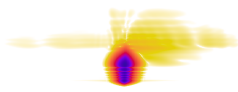
Figure 3.2: Intensity averaged (intensity between  $10^{14}$  W/cm<sup>2</sup> to  $10^{15}$  W/cm<sup>2</sup>) ionization (solid) and dissociation (dash-dotted) yields for HeH<sup>+</sup> (thick lines, left axis) and HeD<sup>+</sup> (thin lines, right axis) after irradiation of the  $v = 0$  state with a two-color laser pulse with 50 fs (1380 nm wavelength) and 60 fs (690 nm wavelength) pulse duration and 5:1 intensity ratio. Reproduced fig. 3 from [53].

behaviour which is symmetric around  $\phi = 0$  (and  $\phi = \pi$ ) in agreement with the considerations from the previous section. The ionization yield has its maximum at  $\phi = 0$  and the minimum at  $\phi = \pi$ ; it is the other way round for the dissociation yield.

Remarkably, the ratio of ionization to dissociation probability drops from 6.3 at  $\phi = 0$  to 0.74 at  $\phi = \pi$ , i. e. dissociation becomes even more probable than ionization.

By changing the relative phase or the delay in a collinear two-color field, the dominant fragmentation channel can be switched from ionization to dissociation and vice versa.

The HeD<sup>+</sup> isotopologue differs from HeH<sup>+</sup> in various ways: 1. The reduced mass  $\mu$  is larger and thus there are more vibrational states and they have smaller transition energies. 2. As a consequence, the vibrational ground state has a slightly lower energy and thus the energy required to reach the dissociation threshold is higher. 3. Since the mass ratio determines the center-of-mass, the dipole moment (vibrational coupling to the electric field) is smaller.



### 3.2 Non-Born-Oppenheimer and focal-volume-averaged results

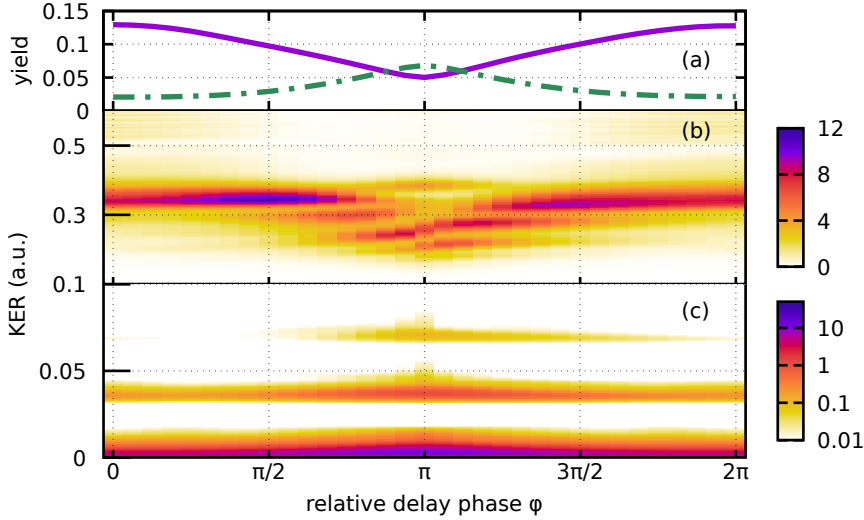


Figure 3.3: Results for same laser parameters as in figure 3.2 (including focal-volume averaging). (a) Probabilities for ionization (solid line) and dissociation into the ground state (dash-dotted line) (same as in Fig. 3.2). (b) KER spectrum for ionization, normalized for every value of  $\varphi$ . (c) KER spectrum for dissociation. Reproduced fig. 7 from [53].

However, the most important *similarity* is that all isotopologues have the same electronic structure, Born-Oppenheimer potential-energy curves etc.

From these considerations it can be understood that the dissociation yield is much lower (almost negligible) for  $\text{HeD}^+$  than for  $\text{HeH}^+$  (note the different scale on the left and right axis). However, just as in the previous chapter we can observe that ionization does not occur independently from the nuclear motion (otherwise the ionization probability of  $\text{HeD}^+$  should be similar to that of  $\text{HeH}^+$ ). Instead, we see the ionization yield reduced by roughly a factor of 5. Also, the relative amplitude of the  $\varphi$  dependence is larger and the minimum around  $\varphi = \pi$  is broader.

Figure 3.3 shows the kinetic-energy release in the ionization (panel (b)) and dissociation channel (panel (c)), respectively. Since they are separated in energy, a single KER axis is used which covers both plots (with different scale, though). Note, however, that the ionization KER is normalized for every value of  $\varphi$  (i. e. divided by the corresponding ionization yield, solid curve

in panel (a)) and that the dissociation KER is shown on a logarithmic scale. This allows us to see the above-threshold-dissociation peaks (cf. section 2.3) which are spaced by photon energies of the fundamental field (0.033 a.u.). The ionization KER  $\approx 1/R_{\text{ion}}$  tells us that for most  $\varphi$ , ionization takes place at 2 a.u.  $< R_{\text{ion}} < 3$  a.u. In contrast to that, the region around  $\varphi = \pi$  that is amplified by the normalization reveals an additional structure at lower KER which indicates ionization from larger internuclear distance, i. e. after some nuclear motion took place.

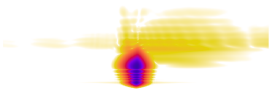
Before going into the details of the ionization and dissociation processes, we can already conclude:

1. Nuclear motion (the vibrational degree of freedom) is important for the ionization process.
2. The  $\varphi$  dependence does not only shift probability between the fragmentation channels while keeping the sum constant. Instead, both processes (ionization and dissociation) depend on  $\varphi$  individually as can be seen from the large difference of the absolute amplitudes in the HeD<sup>+</sup> case.

While the focal-volume averaged results are useful for prediction of and comparison to measurements (which to our knowledge have not been carried out yet), they can obscure the mechanisms. It is important to know that the described effects “survive” focal-volume averaging but we will see in the following that they are also visible at single-intensity calculations which will make interpretations easier.

### 3.3 Two-color ionization in detail

Figure 3.4 shows the same quantities as figure 3.2 but for a shorter laser pulse (both colors 16.7 fs FWHM duration, i. e. 10 cycles of the fundamental field total  $\sin^2$  duration) and for a single peak intensity  $5 \times 10^{14}$  W/cm<sup>2</sup>. The overall results are very similar, although some differences in magnitude and relative height of ionization versus dissociation signal can be seen. Notably, the contrast in the ionization yield—comparing  $\varphi = 0$  to  $\varphi = \pi$ —is much larger without intensity averaging. It is also visible that a 10-cycle pulse is short enough that the assumptions from section 3.1 about the symmetry of  $\varphi$ -dependent observables start to break down. At these laser parameters, the HeD<sup>+</sup> results are decreased even further (by more than a factor of 10 relative





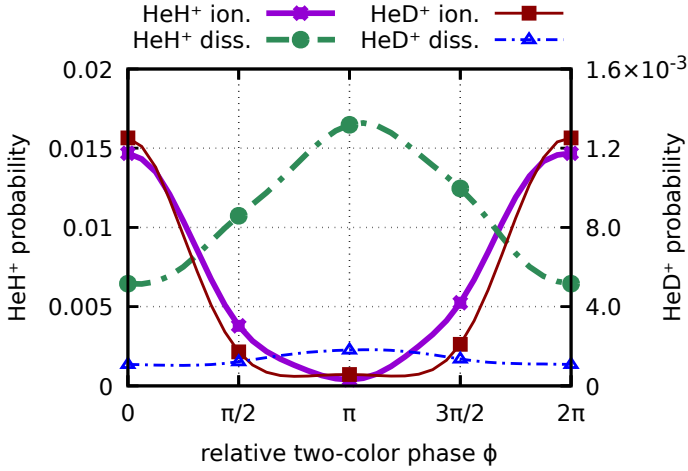


Figure 3.4: Same as figure 3.2 but different laser parameters: single intensity  $5 \times 10^{14} \text{ W/cm}^2$ , pulse duration 16.7 fs for both colors. Reproduced fig. 4 from [53].

to the  $\text{HeH}^+$  results) and the  $\text{HeD}^+$  ionization yield has a broad and almost flat region around  $\varphi = \pi$  with two minima slightly offset from the center.

The maximum (minimum) of the ionization probability at  $\varphi = 0$  ( $\varphi = \pi$ ) is in agreement with our previous results from section 2.4: At  $\varphi = 0$ , the second harmonic increases the positive electric-field maxima which correspond to the electric-field vector pointing from hydrogen to helium, i. e. during ionization, the electron travels from the helium site over the attractive hydrogen potential to the continuum. This is easier than tunneling through the whole barrier on the other side and thus ionization is preferred in this direction. At  $\varphi = \pi$  the electric field in the preferred direction is suppressed.

In order to investigate this mechanism, we compare results from two-color calculations with monochromatic laser pulses which are modified so that they match the central positive electric-field maximum of the two-color pulse. The green dashed curves in figure 3.5 use the same wavelength 1380 nm as the fundamental color in the two-color pulse but have increased intensity so that the maximal field strength is equal. Because there is no DC component (the vector potential vanishes after the pulse,  $A(\infty) = -\int^{\infty} E(t)dt = 0$ ), the second harmonic does not only increase the height of positive electric-field

### 3 Two-color dissociation vs. ionization control at 1380nm

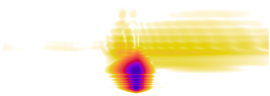
maxima (for  $\varphi = 0$ ) but also makes them shorter whereas the negative parts become slightly longer than half the fundamental period such that the integral is zero. Therefore, the positive half-cycles of the green curve do not match the two-color field exactly and a second monochromatic field (red dotted curve) is constructed as a 10-cycle pulse with increased intensity *and* reduced wavelength which makes the positive half-cycles agree very well. The wavelength is chosen so that the total duration (zero to zero) of the central half-cycle agrees with the two-color field.

Note that at  $\varphi = \pi/2$ , the positive half-cycles last exactly half the fundamental period, i. e. all monochromatic pulses coincide and their ionization yields intersect therefore in figure 3.5(c). It is not useful to match the width for  $\varphi > \pi/2$  because then the positive half-cycle deviates from the cosine shape and develops a double-peak structure towards  $\varphi = \pi$ . In order to account for the pulse duration, we introduce a third monochromatic field with the same intensity and wavelength as the red dotted curve but with the same total pulse duration as the two-color field, i. e. slightly more than 10 optical cycles of the chosen wavelength. While it restores the correct pulse duration, it destroys the matching of the side peaks whose height is now larger than that of the corresponding peak of the two-color pulse (not shown). Obviously, there is a tradeoff when trying to mimic features of a two-color pulse using monochromatic light.

Panels (a) and (b) in figure 3.5 show parts of the two-color and the matching monochromatic laser pulses for two values of  $\varphi$  (the matching is done for every  $\varphi$  separately, here  $\lambda = 1073$  nm in (a) and  $\lambda = 1098$  nm in (b)). The third monochromatic field (with fixed pulse duration) is omitted here since it is very similar to the red dotted curve on this scale. Panel (c) shows the comparison of ionization yields for the four laser-pulse shapes<sup>2</sup> where the violet two-color curve is the same as in figure 3.4. Obviously, just matching the peak intensity (green curve) leads to exceedingly high ionization yields. This is due to the extended duration of the positive half-cycles compared to the two-color pulse: Reducing the wavelength and thus the optical period (red dotted curve) decreases the yield even below the two-color level. Adjusting the pulse duration allows us to reproduce the two-color result quantitatively at least for  $\varphi = 0$ . Apparently, the intra-cycle temporal asymmetry that is

---

<sup>2</sup>By construction, the matched monochromatic curves are symmetric around  $\varphi = \pi$ , therefore only  $\varphi \in [0, \pi]$  is shown.



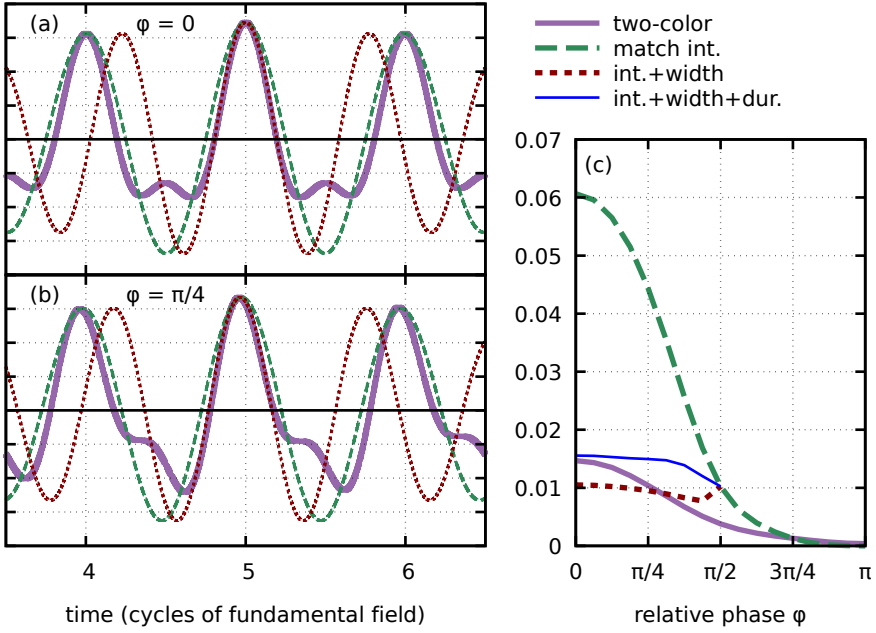


Figure 3.5: (a) and (b): Electric laser fields for relative phases  $\varphi = 0$  and  $\varphi = \pi/4$  (zoom into the center of the 10-cycle pulse). The two-color field is approximated by monochromatic laser pulses with matched peak intensity (“match int.,” green dashed curves) or matched peak intensity and effective wavelength (“int.+width”, red dotted curves). See text for details. (c): Ionization yield calculated in the non-Born-Oppenheimer model using the two-color laser pulse and the matched monochromatic pulses. Included is a modification of the red-dotted curve where the total pulse duration is fixed (“int.+width+dur.,” thin blue line).

### 3 Two-color dissociation vs. ionization control at 1380nm

introduced by the second harmonic for larger relative phases prevents us from mimicking the field using a single color.

Similar to section 2.4, we now run simulations with frozen nuclei in our two-color fields in order to further investigate the role of nuclear motion in the ionization process. Panel (c) of figure 3.6 shows the ionization yields as a function of the fixed internuclear distance for three values of the relative phase  $\varphi$ . Enhanced ionization is visible for  $R > 2$ ; in contrast to figure 2.7, the larger wavelength and pulse duration can lead to saturation for some  $R$  and  $\varphi$ . Weighting the fixed-nuclei yields in panel (c) with the vibrational distributions of the  $v = 0$  state of  $\text{HeH}^+$  or  $\text{HeD}^+$ , respectively, leads to the frozen-nuclei yields in panels (a) and (b).

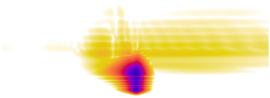
The comparison of the frozen-nuclei results (thin lines) to those from the non-BO model (thick lines) in figure 3.6 (a) and (b) shows that the ionization yield is dramatically underestimated if the nuclear motion is not included. The discrepancy is stronger for the lighter isotopologue  $\text{HeH}^+$  (note that the fixed-nuclei yields have been increased by a factor of 10 for better visibility) than for  $\text{HeD}^+$ . This matches our previous findings that the nuclei move slower in the heavier isotopologue and thus neglecting the nuclear motion introduces smaller errors.

One can also observe that the fixed-nuclei curves in figure 3.6 (a) and (b) have minima which are shifted away from  $\varphi = \pi$ . Although the enhanced ionization at increased  $R$  is much weaker for  $\varphi = \pi$  than for other values of  $\varphi$  (especially between  $R = 3$  a.u. and  $R = 4$  a.u., cf. figure 3.6 (c)), fixed-nuclei ionization is dominated by the region where the vibrational state is actually localized, i. e. around the equilibrium distance  $R \approx 1.46$  a.u. In this region, the ionization probability is not minimal for  $\varphi = \pi$ , but for values near  $\varphi = 5\pi/8$  and  $\varphi = 11\pi/8$ . This is similar to our findings in section 2.4 about the CEP-dependent enhanced ionization in very short laser pulses.

We can summarize the results of this section as follows:

Two-color ionization can to some extent be modelled by using a single-color field that mimics the positive electric-field half-cycles. Not only the maximum field strength is important but also the exact duration of the half-cycles.

Ionization cannot be understood without taking nuclear motion into account.



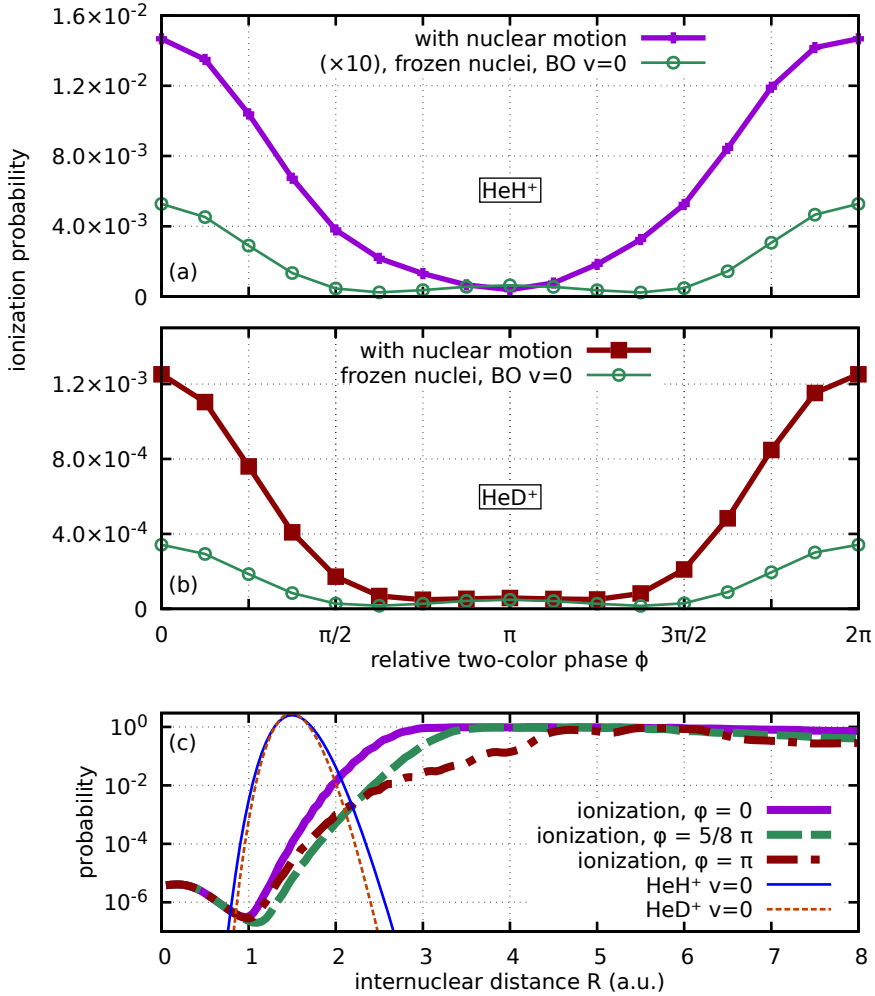


Figure 3.6: Ionization probabilities for the same laser parameters as in figure 3.4. (a) and (b): Comparison of calculations with (thick lines) and without nuclear motion (thin lines with circles) for  $\text{HeH}^+$  (a) and  $\text{HeD}^+$  (b). The fixed-nuclei ionization yield in panel (a) is increased by a factor 10. The thick lines are the same as in figure 3.4. (c): Thick lines: frozen-nuclei ionization probability as a function of internuclear distance for three values of the two-color phase  $\varphi$ . Thin lines: Probability distributions of the vibrational ground states of  $\text{HeH}^+$  and  $\text{HeD}^+$ , respectively. Modified fig. 6 from [53].

### 3.4 Two-color dissociation in detail

We turn to the dissociation process now. In order to understand the mechanisms that are involved, we apply the Born-Oppenheimer approximation and compare the non-BO results to results that follow from one- or two-level Born-Oppenheimer calculations. The derivation of the Born-Oppenheimer model as well as the numerical time-propagation scheme is described in appendix A.2. The Hamiltonian for the  $k$ -th potential-energy surface  $V_k(R)$  reads

$$H_k(t) = \frac{p^2}{2\mu} + V_k(R) - d_k(R)E(t)$$

and the two-level TDSE including the coupling terms is given by

$$i \frac{\partial}{\partial t} \begin{pmatrix} \psi_1(R; t) \\ \psi_2(R; t) \end{pmatrix} = \begin{pmatrix} H_1(t) & -\kappa d_{12}E(t) \\ -\kappa d_{12}E(t) & H_2(t) \end{pmatrix} \begin{pmatrix} \psi_1(R; t) \\ \psi_2(R; t) \end{pmatrix}.$$

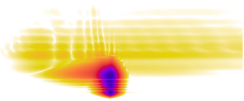
Here, the dipole transition moments are calculated from the electronic eigenstates  $\phi(x; R)$  for frozen nuclei (cf. section 2.4) via

$$d_{jk}(R) = -\langle \phi_j | x | \phi_k \rangle_{(x)}, \quad d_k(R) = -\langle \phi_k | (\kappa x + \lambda R) | \phi_k \rangle_{(x)} \quad (3.2)$$

where  $\kappa = (M + 2)/(M + 1)$  and  $\lambda = (m_{\text{H}} - m_{\text{He}})/M$  (we will discuss the dipole transition moments in more detail in chapter 4).

We can estimate the ground-state dipole moment  $d_1(R)$  roughly with the following picture: In the ground state, the electron is located mostly at the helium site, i. e. the molecule consists of a neutral helium atom and a proton. Since the mass ratio of helium and hydrogen is roughly 4:1, the center of mass—the origin of our coordinate system—is close to the helium nucleus and the proton is located at coordinate  $-0.8R$ . Therefore, the dipole moment  $d_1(R) \approx -0.8R$  is negative and the nuclei are pushed together (pulled apart) at positive (negative) electric-field values. Assuming that pulling the nuclei apart is the main driver for dissociation on the electronic ground-state PEC, this can be an explanation for the maximum of the dissociation yield around  $\varphi = \pi$ .

However, results from one- and two-level Born-Oppenheimer calculations shown in figure 3.7 do not support this explanation: The one-level calculation (blue curve with triangles) which includes the aforementioned mechanism shows only very little  $\varphi$  dependence. It is also out of phase, i. e. without a maximum around  $\varphi = \pi$ . Nevertheless, the single-level model can explain



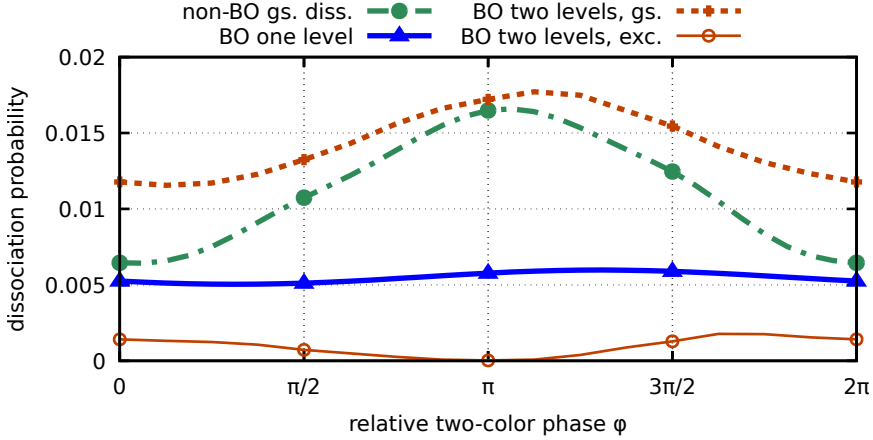


Figure 3.7: Same as figure 3.4 but showing only dissociation probabilities of  $\text{HeH}^+$  and several models: “non-BO” is the non-Born-Oppenheimer dissociation curve from figure 3.4, “BO” curves are from one- and two-level Born-Oppenheimer calculations. Modified fig. 8 from [53].

almost all of the  $\varphi$ -independent dissociation yield. Note that the dot-dashed non-Born-Oppenheimer curve shows only dissociation into the electronic ground state, too. If we add the first excited state to the Born-Oppenheimer model, thereby creating the two-level system, the ground-state dissociation signal (orange dotted curve) is greatly increased and adopts roughly the shape of the non-BO curve with a maximum around  $\varphi = \pi$ . The change of the ground-state dissociation yield by adding the second state is much larger than the actual final population of the second state (thin solid orange curve)<sup>3</sup>. As ionization is stronger for  $\varphi = 0$  than for  $\varphi = \pi$ , one can expect that including ionization in the two-level calculation would give quite good agreement with the non-BO dissociation results.

The instantaneous Born-Oppenheimer potential-energy curves at maximum positive (negative) field strength are shown in figure 3.8 for  $\varphi = 0$  ( $\varphi = \pi$ ). The right panel corresponds to the electric field pointing from helium to hydrogen. Here, we see that the vibrational wave packet becomes temporarily

<sup>3</sup>The second level has a similar  $\varphi$  dependence as the ionization yield in figure 3.4 which makes sense since it is mostly populated when the electric field is positive and pushes the electron wave function from the helium potential well towards the hydrogen side.

### 3 Two-color dissociation vs. ionization control at 1380nm

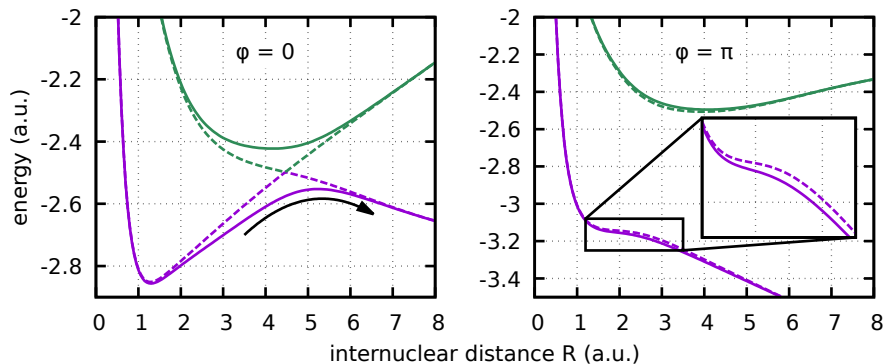
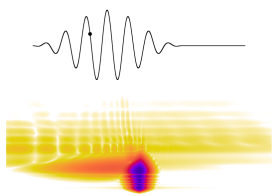


Figure 3.8: Field-dressed instantaneous Born-Oppenheimer potential-energy curves for the two-level system with (solid curves) and without (dashed curves) coupling between the two lowest states, calculated by diagonalizing the Hamiltonian operator. The field strength corresponds to the maximal positive (negative) field strength of the two-color pulse with relative phase  $\varphi = 0$  ( $\varphi = \pi$ ). The black arrow in the left panel indicates the pathway that leads to population of the excited state. Modified fig. 9 from [53].

unbound because the potential barrier is completely suppressed. This is the case even without coupling of the two states (dashed curve). If the coupling is included, it additionally lowers the barrier and thereby extends the time of barrier suppression. This increases the chance for the wave packet to escape towards large internuclear distance, i. e. the dissociation probability is increased compared to the case without coupling. The change to the potential barrier may look negligible but in section 3.3, figure 3.5 we have seen how a subtle change in the duration of positive half-cycles drastically influences the yield. Similarly, an increased period of time with barrier suppression has an enormous effect on the dissociation probability.

If the electric field is reversed—the situation of the left panel—the dressed potential curves are bent towards each other. This is because the dipole moment of the excited state,  $d_2(R) \approx 0.2R$  (for large  $R$ ), and that of the ground state have different signs<sup>4</sup>. By including the coupling term, the crossing turns into an avoided crossing. The resulting barrier on the lower dressed curved

<sup>4</sup>Remember that the ground state corresponds to dissociation into  $\text{He} + \text{H}^+$  whereas the first excited state dissociates into  $\text{He}^+ + \text{H}$ . The given dipole moments are valid for the isotopologue  $^4\text{HeH}^+$  with a nuclear mass ratio of roughly 4:1.





can be overcome by a part of the dissociating wave packet, following the black arrow. This part ends up in the excited state when the laser pulse is over and contributes to its population.

Even though the excited state is energetically well separated and only weakly populated, the dissociation process cannot be explained by the ground-state dynamics alone. The coupling between the two lowest electronic states facilitates efficient dissociation depending on the direction of the electric field. These two states are enough to fairly reproduce the  $\varphi$  dependence of the dissociation yield.

### 3.5 Photoelectron momentum distribution

Figure 3.9 shows the focal-volume averaged photoelectron momentum distribution (PMD) after ionization as a function of the two-color phase  $\varphi$ . It is calculated from the ionized part of the wave function, i. e. the absorbed part at large electron coordinate  $x$ , by integrating the modulus squared of the wave function over the nuclear degree of freedom in momentum space. The result is a one-dimensional distribution where positive (negative) momenta correspond to the electron approaching infinity on the helium (hydrogen) side of the molecule. Since the very slow electrons have not reached the absorbing boundary at the end of the time evolution, there is an unphysical minimum around  $p = 0$ .

In classical mechanics, an electron that is liberated at some time  $t_i$  with zero velocity and subsequently follows the force of an electric (laser) field without any potential is accelerated and ends up with a momentum that is defined by the vector potential at the time of ionization,  $p = A(\infty) - A(t_i)$ . As a simple model we assume that ionization mostly happens at peak electric-field strengths. While a monochromatic field has vanishing vector potential at electric-field maxima, the two-color pulse has a vector potential at maximal ( $A_{\max}$ ) and minimal ( $A_{\min}$ ) electric field that depends on the two-color phase. Here, minimal electric field refers to the *negative* electric-field peaks. The negative vector potential at the main positive and negative peaks is shown as solid lines in the bottom panel of figure 3.9 for one intermediate value for the intensity,  $I = 7 \times 10^{14} \text{ W/cm}^2$ . For those values of  $\varphi$  where the electric field has a double-peak structure in positive or negative direction, the vector potential

at the second peak is shown with symbols.

It can be seen that the PMD follows mostly  $-A_{\max}$ , i. e. ionization takes place at the highest positive field strength. This is in agreement with our previous findings on the orientation dependence. Ionization of the ground state at positive electric field implies that the initial tunneling goes from helium through the hydrogen potential well into the continuum in negative direction. For  $\varphi > \pi$ , however, the asymptotic momentum is positive, i. e. the electron changes direction at some point, recollides<sup>5</sup> and leaves towards  $+\infty$  (forward scattering). The recollision is visible in the larger magnitude of the photoelectron momentum (compare  $0 < \varphi < \pi$  to  $\pi < \varphi < 2\pi$ ) which is typical for photoelectron recollision.

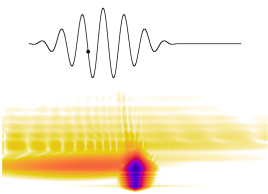
For comparison: The ponderomotive potential  $U_P = E_0^2/(4\omega^2)$  for just the fundamental field at the intermediate intensity  $7 \times 10^{14} \text{ W/cm}^2$  is  $U_P = 4.6 \text{ a.u.}$ , i. e. the  $2U_P$  “cutoff” for direct electrons [119–121] is at an electron momentum of 4.3 a.u. The negative momenta in figure 3.9 all lie within this range whereas the positive momenta exceed this threshold<sup>6</sup>.

### 3.6 Effect of the pulse duration

For  $\text{HeH}^+$  the dominant fragmentation process changes from ionization at  $\varphi = 0$  to dissociation at  $\varphi = \pi$ . We investigate the pulse-duration dependence of these two extreme cases in more detail. The yields as functions of the pulse duration are shown in figure 3.10. Data points from figure 3.2 can be found at the very left end of the graph. The simulations show that for all considered pulse durations the yields of ionization at  $\varphi = 0$  and dissociation at  $\varphi = \pi$  are of similar magnitude and scale approximately linearly with the pulse duration. We note as an observation that when ionization is suppressed ( $\varphi = \pi$ ), its yield grows approximately as  $T^3$ . The dissociation yield for  $\varphi = 0$  decreases for large pulse durations, probably because in long laser pulses, dissociating wave packets can still be ionized later in the pulse at large  $R$ . In this case, only dissociation that is initiated late in the pulse contributes to the dissociation yield.

<sup>5</sup>Since our model is one-dimensional, it is not possible for the electron to “miss” the nuclei when coming back after changing direction.

<sup>6</sup>But there are also higher intensities involved, so this is not a rigorous argument.



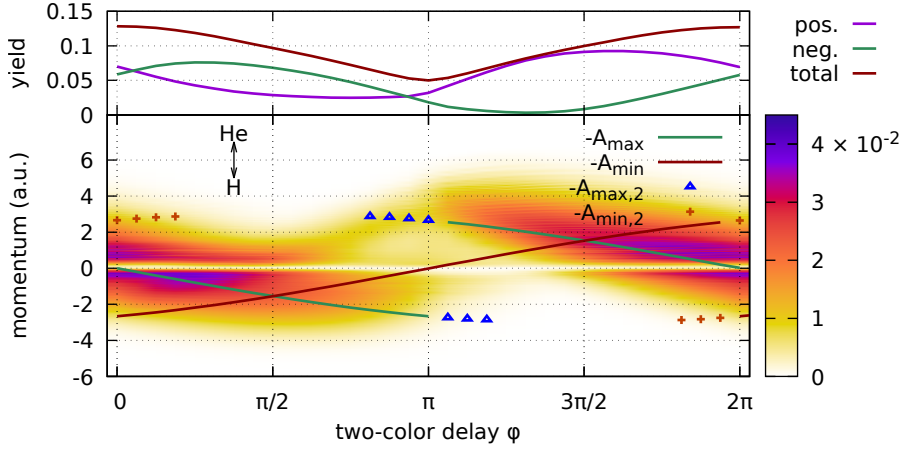


Figure 3.9: Ionization results for same laser parameters as in figure 3.2 (including FVA). Top: Ionization yield for positive and negative asymptotic momentum of the photoelectron and the sum of both. The sum is the same curve as the  $\text{HeH}^+$  ionization yield in figure 3.2. Bottom: 1D photoelectron momentum distribution for each delay. Curves (symbols) are the negative vector potential at the time of (second) largest positive, *max*, or negative, *min*, electric field strength. Curves and symbols are calculated for an intermediate intensity of  $7 \times 10^{14} \text{ W/cm}^2$  for the fundamental field.

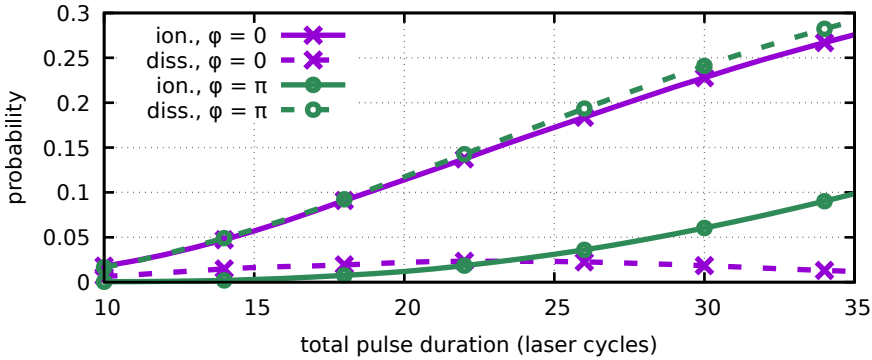
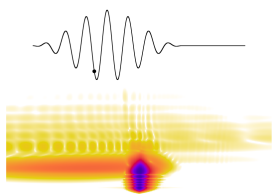


Figure 3.10: Ionization (solid lines) and ground-state dissociation yields (dashed lines) for  $\text{HeH}^+$  ( $v = 0$ ) in a two-color field with relative phase  $\varphi = 0$  (purple crosses) or  $\varphi = \pi$  (green circles) and variable pulse duration. The fundamental wavelength is 1380 nm and the peak intensity is  $5 \times 10^{14} \text{ W/cm}^2$ . The intensity ratio of the two colors is 5:1. Modified fig. 5 from [53].

### 3.7 Conclusion

In this chapter we have shown that it is possible to control the fragmentation process of  $\text{HeH}^+$  efficiently by using a simply tunable parameter, namely the relative two-color phase  $\varphi$  in a linearly polarized laser pulse. The two fragmentation channels ionization and dissociation (into the ground state) have opposite  $\varphi$  dependence and although the mechanisms for both are quite different, they are also linked to each other: Ionization cannot be understood without taking the nuclear motion into account and ground-state dissociation is greatly underestimated if the electronically excited states are neglected.

The focal-volume averaged results and the similar linear dependence of the dominating processes on the pulse duration make the findings of this chapter robust against experimental uncertainties. It would be interesting to have experimental data to compare our theoretical predictions to.



## 4 Mass-dependent dissociation dynamics

If you want to find the secrets of the universe,  
think in terms of energy, frequency and  
vibration.

---

Nikola Tesla

Parts of the content of this chapter have been published in [54].

In the previous chapters 2 and 3 we have already seen isotope effects: Nuclear motion is slower in the heavier isotopologue  $\text{HeD}^+$  than in  $\text{HeH}^+$  and thus there is less population at larger internuclear distance and the enhanced ionization is much weaker (section 2.10). Conversely, frozen-nuclei calculations can reproduce ionization yields much better for  $\text{HeD}^+$  than for  $\text{HeH}^+$  (section 3.3).

$\text{HeH}^+$  isotopologues can differ in multiple properties from each other: The total nuclear mass  $M = m_{\text{H}} + m_{\text{He}}$ , the reduced mass  $\mu = m_{\text{H}} m_{\text{He}} / M$  and the mass ratio  $r = m_{\text{H}} / M$ . The importance of  $M$  is limited since we split off and neglect the center-of-mass motion. The dynamics within the center-of-mass frame—and thus observables such as dissociation or ionization yields—do not depend on the total mass<sup>1</sup>. Instead, the reduced mass  $\mu$  is the parameter that defines the nuclear kinematics because it enters the Hamiltonian (2.3) in the kinetic-energy term of the nuclear degree of freedom. Via the Hamiltonian it also affects the eigenenergies of vibrational states and their spatial distribution (see for example figure 3.6(c)). Finally, the mass ratio  $r$  of the hydrogen nucleus and the total nuclear mass determines the location of the center of mass between the nuclei and thus the permanent dipole moment which is calculated in the center-of-mass frame<sup>2</sup>. The dipole moment is relevant for the coupling of the nuclei to the electric field of the laser pulse and its isotope

---

<sup>1</sup>This is not exactly true since the coupling strength  $\kappa \approx 1$  of the electronic degree of freedom depends on the total mass.

<sup>2</sup>Since the molecule is charged, the dipole moment depends on the coordinate system. We always work in coordinates where the center of mass of the nuclei is at the origin.

#### 4 Mass-dependent dissociation dynamics

dependence has also already been observed experimentally [122].

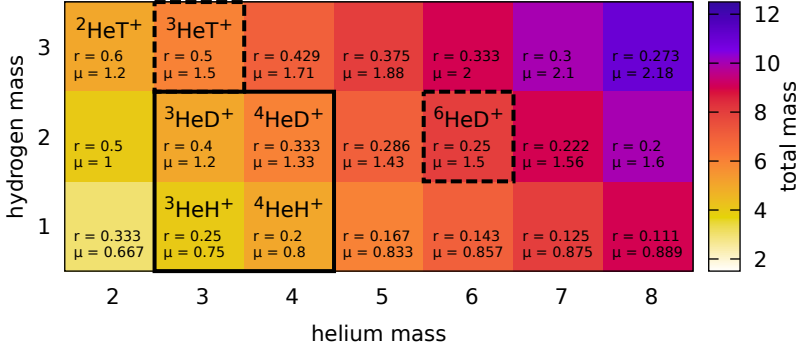
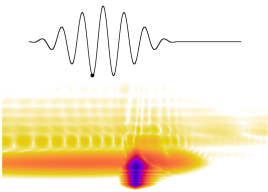


Figure 4.1: Mass ratios  $r = m_{\text{H}}/(m_{\text{H}} + m_{\text{He}})$  and reduced masses  $\mu = m_{\text{H}}m_{\text{He}}/(m_{\text{H}} + m_{\text{He}})$  for all imaginable  $\text{HeH}^+$  isotopologues up to helium mass 8. All masses are given in idealized units of identical neutron/proton mass  $m_{\text{n}}$  and the binding energy (mass defect) is neglected. Color coding shows the total mass  $M = m_{\text{H}} + m_{\text{He}}$ . The isotopologues that can be created using the experimentally available gases ( ${}^3\text{He}$ ,  ${}^4\text{He}$ , H and D) are explicitly labelled and highlighted by the black solid rectangle. The two isotopologues  ${}^3\text{HeT}^+$  and  ${}^6\text{HeD}^+$  with identical reduced mass  $\mu = 1.5 m_{\text{n}}$  are highlighted by black dashed rectangles.  ${}^2\text{HeT}^+$  is the only isotopologue with  $r > 0.5$ .

Since both  $r$  and  $\mu$  affect the strong-field dynamics, it would be desirable to keep one of them fixed while changing the other one in order to systematically study the effect of both. Figure 4.1 shows the values of both for a set of imaginable isotopologues of  $\text{HeH}^+$ . For simplicity we assume in this chapter that protons and neutrons have equal mass  $m_{\text{n}} = 1837$  a.u. and that the binding energy (mass defect) can be neglected. Note that most of the helium isotopes ( ${}^2\text{He}$  and all above  ${}^4\text{He}$ ) are highly unstable and decay with a half-life of less than one second (with surprisingly long half-times of 807 ms for  ${}^6\text{He}$  and 119 ms for  ${}^8\text{He}$  [123]). The experimentally easily available isotopes are  ${}^3\text{He}$  and  ${}^4\text{He}$  for helium as well as H and D for hydrogen. The resulting isotopologues of  $\text{HeH}^+$  are highlighted in the black rectangle. As we can see from figure 4.1, all these isotopologues differ in both  $r$  and  $\mu$ . Theoretically, there is the possibility to compare  ${}^3\text{HeT}^+$  and  ${}^6\text{HeD}^+$  which happen to have the same reduced mass but both tritium and  ${}^6\text{He}$  are not easy to use in strong-field experiments.

In our simulations, however, we can choose  $r$  and  $\mu$  arbitrarily. Using their



definitions, we find:

$$\begin{aligned}
 r &= m_{\text{H}}/M & m_{\text{He}} &= \mu/r \\
 \mu &= m_{\text{H}} m_{\text{He}}/M & \Leftrightarrow & & m_{\text{H}} &= \mu/(1-r) \\
 M &= m_{\text{H}} + m_{\text{He}} & & & M &= \frac{\mu}{r(1-r)}
 \end{aligned}$$

We see that for fixed  $\mu$ , one of the nuclear masses and thus also the total mass diverges if  $r$  approaches 0 or 1. Since our calculations are always carried out in the center-of-mass frame, there are no diverging terms in the Hamiltonian or elsewhere. Therefore, the extreme values of  $r$  are accessible for calculations.

In this chapter, we will study the molecule for fixed  $\mu = 0.8 m_{\text{n}}$  or  $\mu = 1.5 m_{\text{n}}$  and scan the mass ratio  $r$  between 0 and 1. This means that we can study the mass dependence of the coupling to the electric field without getting changes from the nuclear kinematics. Note that we are looking at *artificial* isotopologues; especially  $r > 0.5$  implies that the hydrogen nucleus is heavier than the helium nucleus. In figure 4.1, only the isotopologue  ${}^2\text{HeT}^+$  has this property.

In particular, we will look at the *dissociation dynamics* of these artificial  $\text{HeH}^+$  isotopologues because this can be expected to be most sensitive to changes in  $r$  (compared to, e. g., ionization dynamics which depends on  $r$  only indirectly). We first describe the properties of the applied quantum models as well as the classical-trajectory calculations. After an excursus on classical-trajectory initial conditions we compare and discuss the results of quantum and classical simulations at the end of this chapter.

## 4.1 Quantum models

Similar to the previous chapter, we use the non-Born-Oppenheimer (non-BO) model and the two-level Born-Oppenheimer model and solve the time-dependent Schrödinger equation (TDSE) to describe the strong-field dynamics of  $\text{HeH}^+$  isotopologues.

### 4.1.1 Electron-nuclear non-Born-Oppenheimer TDSE

The non-BO model and the time-evolution scheme have been described in section 2.1 and they are used in this chapter without any changes. We repeat

the TDSE (2.2) and the Hamiltonian (2.3):

$$i \frac{d\Psi(x, R; t)}{dt} = (H_0 + (\kappa x + \lambda R)E(t))\Psi(x, R; t),$$

$$H_0 = \frac{p^2}{2\mu_e} + \frac{P^2}{2\mu} - \frac{Z_1}{\sqrt{(x + \frac{m_{\text{He}}}{M}R)^2 + \alpha_1(R)}} - \frac{Z_2}{\sqrt{(x - \frac{m_{\text{H}}}{M}R)^2 + \alpha_2(R)}} + V_{\text{ion}}(R)$$

Here,  $\kappa = (M + Z_1 + Z_2)/(M + 1)$  and  $\lambda = (Z_1 m_{\text{He}} - Z_2 m_{\text{H}})/M$  are the coupling strengths in the center-of-mass reference frame and  $\mu_e = M/(M + 1)$ .

The numerical discretisation uses 2048 grid points for the  $R$ -direction ( $\Delta R = 0.05$  a.u.) and 4096 grid points for the  $x$ -direction ( $\Delta x = 0.2$  a.u.)<sup>3</sup>. As the initial state for the time evolution we always use the ground state of the system calculated as the lowest-energy eigenstate of the real-time evolution operator [124].

The linearly-polarized laser field is defined via its vector potential,

$$A(t) = \frac{E_0}{\omega} \cos^2(\pi t/T) \sin(\omega t) \quad (\text{for } -T/2 \leq t \leq T/2), \quad E(t) = -\dot{A}(t),$$

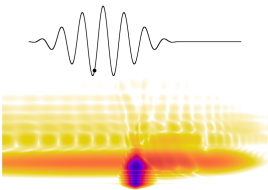
where  $T = T_{\text{FWHM}}/0.3641$  and  $T_{\text{FWHM}}$  is the full width at half maximum (FWHM) of the intensity. This form of the laser pulse guarantees that  $A(-\infty) = A(\infty) = 0$  and thus there is no DC component in the electric field. Throughout this chapter, the pulse duration is fixed at  $T_{\text{FWHM}} \approx 50$  fs.

At the end of the time evolution, all bound states (also calculated as real-time-propagator eigenstates) are projected out from the wave function which leaves the dissociating part only. This is then projected onto electronic eigenstates in order to yield dissociation probabilities for each electronic channel.

### 4.1.2 Two-level Born-Oppenheimer TDSE

In addition to the non-Born-Oppenheimer model, we apply the Born-Oppenheimer approximation again and use the same two-level model as in section 3.4. We can expect it to reproduce the non-BO results even better in this chapter than in the previous one because we will use longer wavelengths which drive

<sup>3</sup>The number of grid points in  $x$ -direction is larger than in chapter 2 because the larger wavelengths used in this chapter increase the electron excursion distance which has to be covered by the grid.





vibrational motion more efficiently and electronic excitations less efficiently than the 1380 nm used before. We will see that assumption confirmed later.

In order to investigate the effect of the mass ratio  $r$ , we first consider a nuclear wave function  $\psi_k$  on the  $k$ -th potential-energy surface alone, i. e. without coupling to other surfaces. The TDSE and the Hamiltonian are given by

$$\begin{aligned} i \frac{\partial}{\partial t} \psi_k(R; t) &= H_k(t) \psi_k(R; t), \\ H_k(t) &= \frac{P^2}{2\mu} + V_k(R) - d_k(R)E(t), \end{aligned} \quad (4.1)$$

where the dipole moment  $d_k(R)$  is calculated from the non-Born-Oppenheimer model as follows. The  $R$ -dependent  $k$ -th electronic eigenstate  $\phi_k(x; R)$  is calculated for frozen nuclei<sup>4</sup>. With the mass ratio  $r$ , the nuclear center of mass moves between the helium nucleus and the proton and with it the origin for the electron coordinate  $x$ . In other words: A coordinate shift relates  $\phi_k$  for different  $r$ .

$$\phi_k(x; R) = \phi_{k,r=0}(x + rR; R)$$

It follows that also the  $r$ -dependence of the purely electronic dipole transition moments can be made explicit,

$$d_{jk}(R) = -\langle \phi_j | x | \phi_k \rangle_{(x)} = d_{jk}(R) \Big|_{r=0} + rR \delta_{jk}. \quad (4.2)$$

The dipole moment  $d_k(R)$  used in (4.1) is defined as in (3.2); it consists of the contributions from the electron on the one hand and from the charged cores on the other hand. Its  $r$ -dependence can also be made explicit<sup>5</sup>,

$$d_k(R) = -\langle \phi_k | (\kappa x + \lambda R) | \phi_k \rangle_{(x)} = \kappa d_{kk}(R) \Big|_{r=0} + [1 - (2 - \kappa)r] R, \quad (4.3)$$

In the following, we use  $d(R)$  as an abbreviation for the permanent ground-state dipole moment  $d_1(R)$ . Its  $R$ -dependence is the main property that determines whether the laser field can drive vibrational transitions. Figure 4.2 shows  $d(R)$  for various values of  $r$ .

<sup>4</sup>Cf. section 2.4 for details on frozen-nuclei calculations. Note that in these calculations, the reduced electron mass is always  $\mu_e = 1$  regardless of  $r$ .

<sup>5</sup>Note that  $\kappa$  also depends (weakly) on  $r$ .

#### 4 Mass-dependent dissociation dynamics

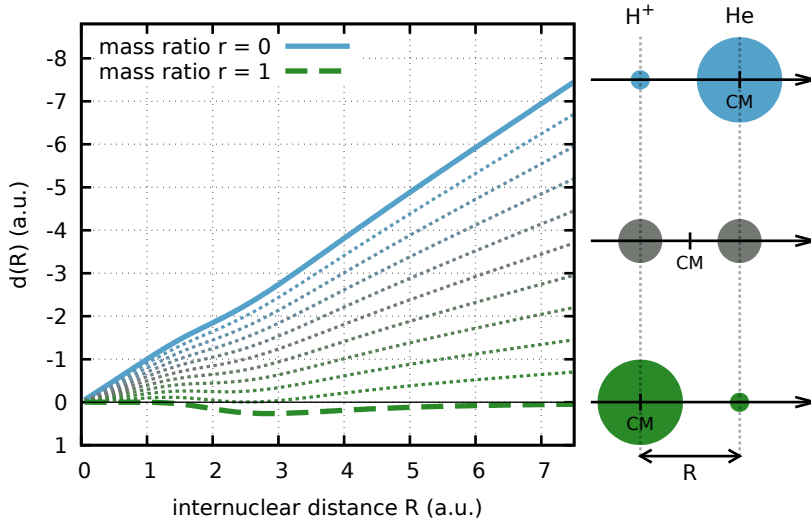
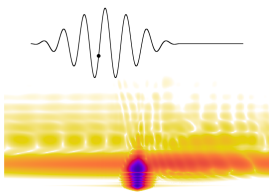


Figure 4.2: Left: Dipole coupling  $d(R)$  in the electronic ground state as calculated from (4.3). Solid curves show the extreme cases where all mass is concentrated in one nucleus. Dotted curves are calculated for intermediate values of the mass ratio  $r$  in steps of 0.1. Right: Sketch of the mass distribution for three cases of  $r$ ; the sizes of the circles represent the respective masses. With the mass ratio, the nuclear center of mass (CM)—the origin of the coordinate system—moves from the helium nucleus to the proton. Modified fig. 1 from [54]. Note that for consistency with our non-BO model, the orientation of the molecule has been inverted relative to [54] and thus  $d(R)$  has the opposite sign.



We allow electronic excitation from the ground state to the first excited state by including the coupling term  $d_{12}(R)$ . Using the definitions (4.1) and (4.2), the TDSE then reads

$$i \frac{\partial}{\partial t} \begin{pmatrix} \psi_1(R; t) \\ \psi_2(R; t) \end{pmatrix} = \begin{pmatrix} H_1(t) & -\kappa d_{12}E(t) \\ -\kappa d_{12}E(t) & H_2(t) \end{pmatrix} \begin{pmatrix} \psi_1(R; t) \\ \psi_2(R; t) \end{pmatrix}. \quad (4.4)$$

In numerical calculations, the same  $R$ -grid is used as for the non-BO model. The TDSE is solved by applying the split-operator scheme twice—for the single-level propagator using  $H_i(t)$  and to account for the off-diagonal part of the matrix. Details on the two-level model and the time-evolution scheme are described in appendix A.2.

Consistently with the non-BO model, we use the lowest-energy bound state as the initial state for the time evolution, i. e. the vibrational ground state of the lowest electronic state.  $\psi_2$  is initialized as 0. After the laser pulse, the dissociation probabilities for the two available channels are calculated as follows. All bound states are projected out from  $\psi_1$  which leaves the dissociating wave packet in the electronic ground state. All population of  $\psi_2$  contributes to the dissociation into the first-excited-state channel. The probabilities are calculated from the squared norm of the respective wave functions.

## 4.2 Classical-trajectory model

Since the nuclei move relatively slowly, we also try modelling the nuclear degree of freedom using ensembles of classical trajectories. Treating the nuclei classically means that we use the Hamiltonian function

$$H(R, P; t) = \frac{P^2}{2\mu} + V(R) - d(R)E(t),$$

where  $V(R) = V_1(R)$  and the other terms as defined before so that it agrees with the quantum-mechanical ground-state Hamiltonian in Born-Oppenheimer approximation (4.1). Then, the particle motion is described by Hamilton's equations

$$\begin{aligned} \frac{dR}{dt} &= \frac{\partial H}{\partial P} = P/\mu, \\ \frac{dP}{dt} &= -\frac{\partial H}{\partial R} = F(R, t) = -\nabla(V(R) - d(R)E(t)), \end{aligned} \quad (4.5)$$

where  $F(R, t)$  is the classical force. Given some initial position  $R(t_0)$  and momentum  $P(t_0)$ , the time evolution until some final time  $t_f$  after the laser pulse is performed using the fourth-order Runge-Kutta method [125, 126] with adaptive step size. The potential  $V(R)$  and dipole moment  $d(R)$  are taken from the two-level quantum system and linearly interpolated between grid points. After the time evolution, the final total energy  $E_f = H(R(t_f), P(t_f), t_f)$  determines whether a trajectory is unbound (by comparison with the asymptotic potential value  $V(\infty)$ , i. e. the dissociation threshold).

The most important ingredient for this type of classical-trajectory calculations is the choice of initial conditions. There are many possible choices and we will discuss a few in the following chapter.

### 4.3 Excursus: Classical initial conditions

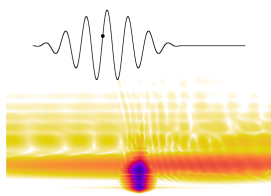
For this chapter, we briefly consider the general case that we want to reproduce a quantum-mechanical observable using classical trajectories. More specifically, we consider a one-dimensional<sup>6</sup> particle in a potential with a single minimum and a finite asymptotic value<sup>7</sup> so that there are unbound continuum states. The observable we are interested in is the probability to drive the system into the continuum. If the coordinate describes the internuclear distance of a diatomic molecule—the situation we have in mind—, this corresponds to dissociation. The question in this chapter is: How to sensibly choose initial conditions for classical trajectories in order to reproduce the quantum results?

One criterion for the initial condition is that it should somehow depend on the quantum-mechanical initial state, e. g. a vibrational wave function  $\psi_0$ , in order to provide a link between quantum and classical calculations. It also makes sense that the probability distribution should not change if it is propagated classically without any laser field; we call this a stationary distribution. We will see shortly that this is not always the case.

---

<sup>6</sup>The “stationary initial conditions” defined in this chapter do not generalize to more than one dimension straightforwardly, therefore we apply this restriction.

<sup>7</sup>Both conditions are typically met for ground-state Born-Oppenheimer curves of diatomic molecules such as  $\text{HeH}^+$ .



### 4.3.1 Equilibrium position & expectation values

The simplest translation from the quantum to the classical world is via expectation values. This generates one set of initial conditions, position  $\langle R \rangle = \langle \psi_0 | R | \psi_0 \rangle$  and momentum  $\langle P \rangle = \langle \psi_0 | P | \psi_0 \rangle = 0$ , which (due to its vanishing initial velocity) is stationary in field-free classical propagation. Alternatively, the position  $\langle R \rangle$  and the (eigen-)energy  $\langle \psi_0 | H | \psi_0 \rangle = E_0$  can be used to calculate an initial velocity.<sup>8</sup> The obvious drawback of this sampling method is that it does not allow to extract probabilities, generate spectra or investigate mechanisms for multiple outcomes because only a single trajectory is propagated. It is thus not suitable for our dissociation studies.

### 4.3.2 Fixed-energy momentum or position distribution

The initial state can be described by a position-space wave function  $\psi_0(R)$  or via Fourier transform by a momentum-space wave function  $\tilde{\psi}_0(P)$ . Their magnitude squared define probability distributions which can be used to construct phase-space distributions as follows. For each initial position (momentum) the corresponding momentum (position) is calculated<sup>9</sup> via the energy condition  $P^2/2\mu + V(R) = E_0$ , where  $E_0$  is the eigenenergy of  $\psi_0$ . Note that although these two phase-space distributions are defined similarly, their spatial distributions differ significantly: If  $\psi_0$  is the vibrational ground state,  $\psi_0(R)$  has a maximum around the potential minimum whereas  $\tilde{\psi}_0(P)$  is centered around zero which leads to a classical position distribution with peaks at the classical turning points (where  $V(R) = E_0$ ). A similar observation can be made for the momentum distributions. Neither  $\psi_0(R)$  nor  $\tilde{\psi}_0(P)$  are stationary when propagated classically: The unique stationary probability distribution at fixed energy  $E_0$  is defined by the time that a classical particle spends at a certain location. This (infinitesimal) time is inversely proportional to the particle's speed  $|v_{E_0}(R)| = \sqrt{\frac{2}{\mu}(E_0 - V(R))}$  and diverges at the turning points.

---

<sup>8</sup>The first approach gives the same initial conditions for all eigenstates of a harmonic oscillator (or any symmetric potential) regardless of their energy, i. e. it does not even fulfil the first criterion from above: dependence on the initial quantum state.

<sup>9</sup>There are no real solutions outside the classically allowed region, thus we cut off the spatial wave function at the turning points. Within the classically allowed region, this equation has two solutions which can either be randomized or trajectories for both solutions are started (which leads to a strictly symmetric momentum distribution which can be desirable).

On the one hand, the sharp energy spectrum of these distributions corresponds well to the sharp eigenenergy of the initial quantum state. On the other hand, the quantum wave function always extends into the classically forbidden region whereas the classical distribution is strictly confined to the phase-space region defined by  $E_0$ . We will see that it is necessary to include initial conditions with higher energy in order to provide any dissociation signal at all for certain parameter choices.

### 4.3.3 Wigner or Husimi distribution

The Wigner distribution [127] for  $\psi_0$  is a phase-space function defined as

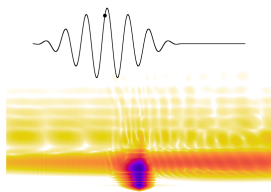
$$W(R, P) = \frac{1}{\pi} \int_{-\infty}^{\infty} \psi_0^*(R + s) \psi_0(R - s) e^{2iPs} ds$$

where we extend  $\psi_0(R)$  to negative arguments by setting  $\psi_0(R) = 0$  for  $R \leq 0$ . The Wigner distribution has the neat property that integrating over one of the phase-space variables yields the correct probability distribution for the other one, i. e.  $\int W(R, P) dP = |\psi_0(R)|^2$  and  $\int W(R, P) dR = |\tilde{\psi}_0(P)|^2$ . The Wigner distribution can take negative values. However, for our application—sampling the vibrational ground state—this is not an issue<sup>10</sup>. In case that the negative values are a problem in other applications, it is possible to use the Husimi distribution instead which is a smoothed version (convolution with a Gaussian) of the Wigner distribution—at the cost of changing the marginal distributions [129].

### 4.3.4 Stationary initial conditions

As described in section 4.3.2 on fixed-energy distributions, there is a unique stationary distribution for a given energy  $E$ . Since the following considerations are not only valid for our specific case of vibrational motion, let us use  $x$  and  $p$  as generalized one-dimensional coordinate and momentum labels for a moment and assume that  $V(x)$  is a general potential with a single minimum.

<sup>10</sup>The Wigner function is positive iff  $\psi_0(R) \sim e^{-(aR^2+2bR)/2}$  with  $\text{Re } a > 0$  [128]. Since the ground state is close to a (shifted) Gaussian function, the negative parts of the Wigner function are small and they are located outside the region of the phase space that corresponds to bound initial conditions.



Then,

$$P_E(x) = \frac{2}{T_E} \frac{1}{|v_E(x)|} \quad (4.6)$$

is the stationary probability distribution where  $|v_E(x)| = \sqrt{\frac{2}{\mu}(E - V(x))}$  is the speed at position  $x$ ,

$$T_E = 2 \int_{x_l}^{x_r} \frac{1}{|v_E(x)|} dx$$

is the oscillation period (which is included in (4.6) for normalization) and  $x_{l,r}$  are the left and right turning points,  $V(x_{l,r}) = E$ ,  $x_l \leq x_r$ . For an ensemble of classical trajectories all with the same energy  $E$  to be stationary (i. e. the probability distributions<sup>11</sup> in space or momentum are constant in time), we require it to be distributed in space according to (4.6) and in momentum according to the energy condition

$$E = \frac{p^2}{2\mu} + V(x)$$

with positive and negative momenta being equiprobable. Since the total energy of a particle is a constant of motion, we can add up ensembles of trajectories with several energies weighted by an energy spectrum  $S(E)$  and end up with a stationary ensemble as long as for each energy the aforementioned conditions are met. The spatial distribution is then given by

$$P(x) = \int S(E) P_E(x) dE. \quad (4.7)$$

Every distribution can be uniquely decomposed into an energy integral like this. Furthermore, an distribution is stationary if and only if every energy component by itself is stationary. Since the stationary distribution at fixed energy (4.6) is unique, it follows that every stationary distribution can be written in the form of (4.7).

In order to apply these considerations to our system, we want  $P(x)$  to reproduce the quantum probability  $|\psi_0(x)|^2$  as closely as possible. It turns out that it is possible to reproduce any (continuously differentiable) function  $f(x)$  on *one side of the minimum*, e. g. using

$$S(E) \sim \begin{cases} T_E \int_{x_r(E)}^{\infty} \frac{f'(x)}{\sqrt{V(x)-E}} dx & \text{if } E \in (V_{\min}, V_{\max,+}) \\ 0 & \text{else} \end{cases} \quad (4.8)$$

---

<sup>11</sup>For a finite number of trajectories, binning is required.

to reproduce  $f(x)$  on the right of the potential minimum. Here,  $V_{\min} = \min_x V(x)$  is the potential minimum and  $V_{\max,+} = \lim_{x \rightarrow \infty} V(x)$  is the right asymptotic potential value. By construction, this distribution is guaranteed to be stationary under field-free propagation.

To prove that  $S(E)$  reproduces  $f(x)$ , one can simply insert (4.6) and (4.8) into (4.7) and use Fubini's integral theorem. The derivation of (4.8) is inspired by the inverse Abel transform [130]: Inserting (4.6) into (4.7), doing partial integration and differentiating with respect to  $x$  yields

$$P'(x) = \sqrt{2\mu} \int_{V(x)}^{\infty} \frac{\tilde{S}'(E)}{\sqrt{E - V(x)}} V'(x) dE, \quad (4.9)$$

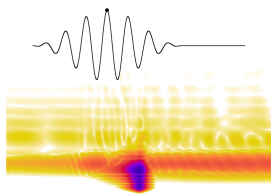
where  $\tilde{S}(E) = S(E)/T_E$ . (4.8) inverts this relation to ensure  $P(x) = f(x)$ . Note that for a given  $x$ , only energies with  $E > V(x)$  contribute to  $P'(x)$  in (4.9). The same ‘‘onion-peeling’’ principle applies in (4.8).

Later in this chapter, we will use and compare the Wigner distribution and the stationary initial conditions (SIC) for classical-trajectory calculations. Differences will become obvious and we will discuss them in section 4.6.

## 4.4 Quantum ladder climbing to dissociation

The energies and energy spacings of vibrational levels depend on the reduced mass  $\mu$  but not on the mass ratio  $r$ . We choose the laser wavelength so that we efficiently drive one of the transitions  $v = 0 \rightarrow 1$  or  $v = 0 \rightarrow 2$  with  $v$  being the vibrational quantum number. More precisely, we use 3436 nm for  $\mu = 0.8m_n$  and 4575 nm or 2376 nm for  $\mu = 1.5m_n$ . For these three cases, the dissociation yield as a function of the mass ratio  $r$  is shown in figure 4.3. It can be seen that the dissociation yield changes by many orders of magnitude despite always matching a resonant transition. The blue triangular data points from non-Born-Oppenheimer calculations agree very well with the corresponding two-level Born-Oppenheimer results (violet solid line). We infer that the role of excited states beyond the first excited state is negligible. The most remarkable feature of figure 4.3 is the deep minimum around  $r = 0.8$  if the wavelength corresponds to the  $v = 0 \rightarrow 1$  resonance. In contrast, the yield decreases monotonically with  $r$  for the  $v = 0 \rightarrow 2$  resonance case.

The dipole coupling  $d(R)$ , depicted in figure 4.2, depends monotonically on  $r$  for most  $R$ . In the simple approximation that  $\text{HeH}^+$  consists of a neutral





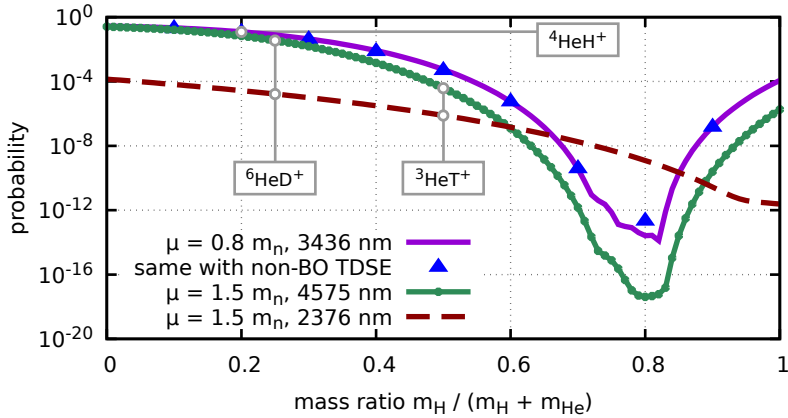


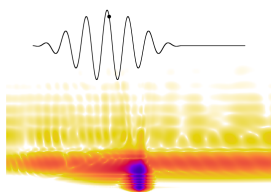
Figure 4.3: Ground-state dissociation yield from a 50 fs laser pulse at  $7 \times 10^{13} \text{ W/cm}^2$  peak intensity as a function of the mass ratio  $r$ . The wavelength is chosen so that either the  $v = 0 \rightarrow 1$  transition (violet line, blue triangles and small green circles) or the  $v = 0 \rightarrow 2$  transition (brown dashed curve) are in resonance. Blue triangles are calculated using the non-BO model, all other curves are calculated in high resolution (steps in the mass ratio 0.01) using the two-level BO model. Data points (mass ratio & reduced mass) that correspond to existing isotopologues of  $\text{HeH}^+$  are marked, cf. figure 4.1. Modified fig. 2 from [54].

helium atom and a proton (sketched on the right of figure 4.2), the dipole coupling is  $d(R) = -(1 - r)R$ . Decreasing the magnitude of the dipole coupling by increasing  $r$  effectively reduces the laser interaction term  $-d(R)E(t)$  in the nuclear Hamiltonian (4.1), i. e. it has the same effect as decreasing the laser field strength<sup>12</sup>. This can already explain qualitatively the dashed curve in figure 4.3. In order to understand the minimum that occurs if we drive the  $v = 0 \rightarrow 1$  transition (solid curves), we need to consider the exact shape of  $d(R)$ : It differs from  $-(1 - r)R$  because the ground-state electron is not exactly located at the helium nucleus; the polarized helium atom partly counters the dipole moment that is due to the location of the proton. This gives rise to the “bump” in  $d(R)$ .

We now consider vibrational transitions in the electronic ground state, i. e. we use the vibrational states in the lower level of the two-level Born-Oppenheimer model. The coupling strength is given by vibrational transition matrix elements  $|\langle v_2 | d(R) | v_1 \rangle|$  for the vibrational transition  $v_1 \rightarrow v_2$ . If the dipole moment was given by the simple formula  $-(1 - r)R$ , then the transition matrix elements as a function of  $r$  would be proportional to  $1 - r$ . If instead we insert  $d(R)$  including the “bump”, the resulting transition matrix elements can cross zero at  $r < 1$  which leads to distinct minima in figure 4.4 (a) and (b). Especially the series of vibrational transitions that occur in vibrational ladder climbing ( $v = 0 \rightarrow 1 \rightarrow 2$  etc.) all have minima close to  $r = 0.8$ . Since the probability for reaching a highly excited state via ladder climbing depends on the product of the single transition probabilities, all these minima together contribute to the structure of the minimum in the dissociation yield in figure 4.3. Note that “ladder climbing” is an idealized picture for the excitation to the dissociation threshold: Due to the anharmonicity of the potential, the spacings between successive vibrational levels become smaller towards larger energies and the higher transitions are not driven in perfect resonance by our laser pulses.<sup>13</sup> Therefore, multiple pathways may contribute to the dissociation yield. They all have in common the excitation step to the first excited state as a gateway if we specifically tune the laser to that resonance. We see that at a certain mass ratio, this gateway is effectively blocked which results in significant suppression of the dissociation probability.

<sup>12</sup>Dipole coupling of vibrational states requires a  $R$ -dependent dipole moment, i. e. the magnitude of  $d'(R)$  is essential, not that of  $d(R)$ . However, decreasing  $d(R)$  or  $E(t)$  has the same effect as decreasing  $d'(R)$ .

<sup>13</sup>See [103] for a detailed study of  $\text{HeH}^+$  as an example of an anharmonic oscillator.



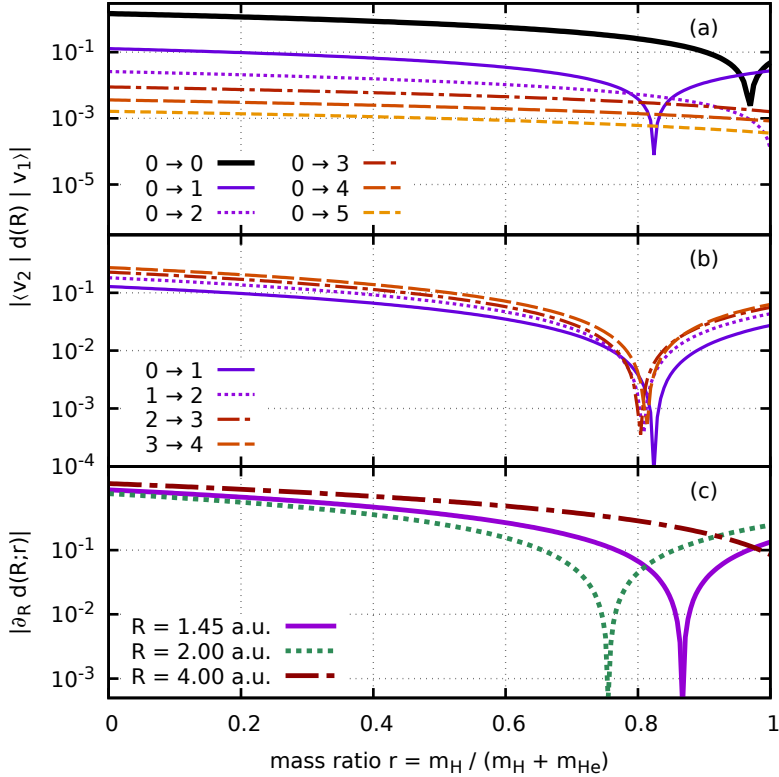


Figure 4.4: Upper two panels: Vibrational transition matrix elements  $|\langle v_2 | d(R) | v_1 \rangle|$  for selected vibrational transitions  $v_1 \rightarrow v_2$  in the electronic ground state with  $\mu = 0.8m_n$ . (a) Transitions which start in the vibrational ground state. (b) First four transitions that occur in a vibrational ladder-climbing scheme starting in the ground state  $v = 0$ . (c) Derivative of the dipole coupling  $d(R)$  at three selected internuclear distances. This quantity is proportional to the classical driving force, see (4.5). Modified fig. 3 from [54].

In agreement with this explanation, the dissociation yield in the  $v = 0 \rightarrow 2$  resonance case in figure 4.3 follows a similar trend as the corresponding  $v = 0 \rightarrow 2$  curve in figure 4.4(a).

### 4.5 Electronic excitation

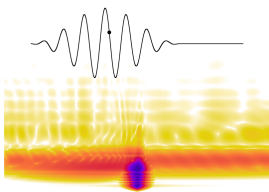
In the two-level TDSE (4.4), the electronically excited state is coupled to the ground state via the dipole transition element  $d_{12}$  which is independent of the mass ratio, see (4.2). Therefore, we could expect the population of electronically excited states to be independent of  $r$  in first order, i. e. without taking nuclear motion into account. Figure 4.5 shows the population of the first excited state at the end of the time evolution for both the two-level Born-Oppenheimer model (yellow dashed line) and the non-Born-Oppenheimer model (orange circles). We see that it has the same general shape as the probability for dissociation into the ground state, i. e. a suppression by many orders of magnitude centered roughly around  $r = 0.8$ . The flattened minimum at approximately  $10^{-15}$  is the double-precision limit of the numerical calculation of the population and likely not caused by physics.

From the population of the excited state and its dependence on the mass ratio we can conclude that electronic excitation does not occur primarily from the initial vibrational state (which would give the same value for all  $r$ ). Instead, enhanced excitation [90] at larger internuclear distance is the main pathway to the excited state. This is similar to chapter 2 where we already saw how vibrational motion affects the probability for electronic transitions. Here, the dissociation probability is directly connected to the expansion of the molecule into the region of enhanced excitation which explains the similar shapes of the excitation and dissociation curves.

Overall, the magnitude of the excited-state population is very small both in absolute numbers and also relative to the dissociation probability. It is therefore justified to carry out the following classical calculations on the ground-state potential curve alone.

### 4.6 Classical dissociation probabilities

Now, we compare the results from TDSE calculations for  $\mu = 0.8m_n$  and 3436 nm wavelength to classical simulations as described in section 4.2. For a



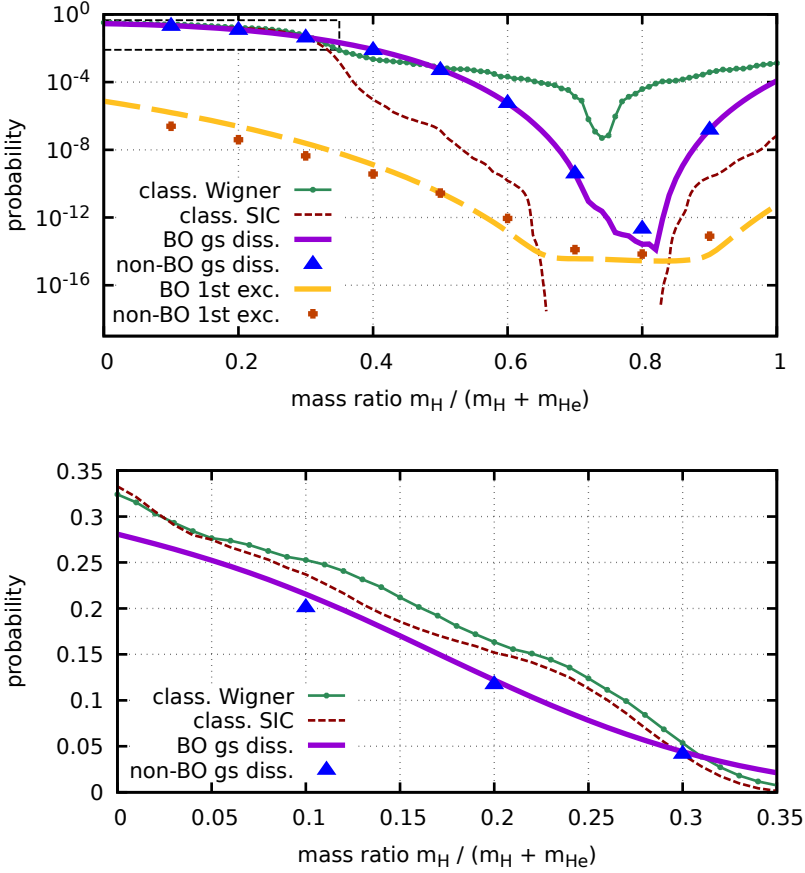


Figure 4.5: Dissociation probabilities for  $\mu = 0.8m_n$  and a 50 fs laser pulse with  $7 \times 10^{13} \text{ W/cm}^2$  peak intensity at 3436 nm wavelength. The green line/circles show results from classical calculations on the electronic-ground-state potential curve using the Wigner distribution as initial conditions. The red dashed curve shows the same using stationary initial conditions (SIC) as defined in section 4.3.4. The violet solid curve and the blue triangles show the ground-state dissociation yield from TDSE calculations (same as in figure 4.3). Additionally, the population of the first excited electronic state is shown (yellow dashed curve and orange symbols). The curves without symbols are calculated using the two-level BO model; the blue triangles and orange crosses are results from the non-BO TDSE. Bottom panel shows a linear-scale zoom into the dashed rectangular region of the top panel. Modified fig. 4 from [54].

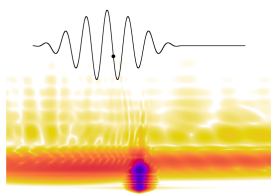
classical trajectory, there are no vibrational levels with transition probabilities. Instead, there is a time- and position-dependent force  $F(R, t)$ , (4.5). Via  $d'(R)$ , it depends not only on  $R$  but also, parametrically, on the mass ratio  $r$ . For three values of the internuclear distance, the  $r$  dependence of the force is plotted in figure 4.4(c). From (4.3) and figure 4.2 it can be seen that  $d'(R)$  depends roughly linearly on  $r$  and may or may not cross zero, depending on the value of  $R$ . Zero-crossings are visible in the log-scale plot of figure 4.4(c) as deep minima at mass ratios that depend on  $R$ . This means that for each  $r \gtrsim 0.7$ , there is an internuclear distance between the equilibrium distance ( $R = 1.45$  a.u.) and the dissociation limit where the force vanishes and the molecule can be trapped.

In figure 4.5, the classical dissociation probabilities are shown as green circles/line (Wigner initial conditions) and thin dashed line (stationary initial conditions). Both results show a significant suppression of the dissociation process near  $r = 0.75$  in agreement with the previous reasoning and the quantum models. It is, however, remarkable that the quantitative results of the classical calculations are extremely sensitive to the choice of initial conditions.

The right panel of figure 4.5 shows the small- $r$  region of the left panel in linear scale. It can be seen that here both classical models are able to reproduce the quantum results relatively well. This is because at small mass ratio the force is strong enough to drive trajectories with low initial energy—this means location close to the potential minimum and small velocity—out to the continuum. Both the Wigner distribution and the stationary initial conditions have most of their probabilities concentrated at this low-energy part of the phase space. If the laser coupling becomes weaker with increasing  $r$ , the probability at larger initial energies becomes more and more important. Whereas—by definition—the SIC energy spectrum approaches zero towards the dissociation threshold, the Wigner distribution has a finite value at the threshold<sup>14</sup>. From these considerations it is clear that fixed-energy distributions of initial conditions as described in section 4.3.2 give much too small yields. To be precise, I was not able to find any classical trajectory at all which starts at the energy of the vibrational ground state and dissociates at the conditions of figure 4.5 for  $r \gtrsim 0.4$ , i. e. the yield drops to zero.

We conclude that on the one hand it is hard to simulate a quantum process

<sup>14</sup>Actually, the Wigner distribution's energy spectrum exceeds the dissociation threshold and thus contains unbound initial conditions. We do not consider these self-dissociating initial conditions, i. e. we cut the energy spectrum at the dissociation threshold.



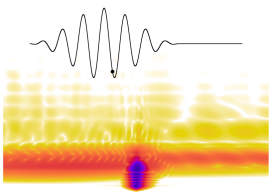
using classical trajectories. Results depend on the choice of initial conditions. Similarities between the quantum initial state and classical initial conditions can (or must) not be made perfect, e. g. the sharp energy of the quantum state must not be reproduced by the classical initial energy distribution. On the other hand, the same suppression effect as in quantum simulations can be seen, at least qualitatively: Via the mass-ratio dependent coupling of the molecule to the laser field, the dissociation probability depends on the distribution of the nuclear masses and the resulting permanent dipole moment. This can change the dissociation probability by several orders of magnitude.

## 4.7 Conclusion

In this chapter, we have seen that not only the reduced molecular mass but also the mass distribution within a molecule can affect the dynamics in strong external laser fields significantly. The ingredients for this effect are: 1. a *total charge* of the molecule such that the dipole moment depends on the location of the center of mass and 2. a *wavelength that is long enough* to drive certain vibrational transitions, in our case  $v = 0 \rightarrow 1$ . If these conditions are met, the mass-ratio dependent dipole transition matrix elements in the dissociation pathway via vibrational ladder climbing vanish at some mass ratio which leads to dramatically decreased dissociation probability. For the  $\text{HeH}^+$  case studied here, the critical mass ratio is around 0.8 which is not realistic since the hydrogen would need to be heavier than the helium.

The general observation is, however, that moving the center of mass close to the charge (assuming the simple model of a diatomic molecule with one neutral and one charged component) reduces the dipole moment and suppresses the dissociation. In this sense, our simple artificial model  $\text{HeH}^+$  generalizes to other molecular ions and may find applications in other studies of isotope-dependent strong-field effects.

Notably, strong-field dissociation of charged molecules occurs frequently as the second step after strong-field ionization of neutral molecules. Since the dipole moment depends on the electronic state that is populated after the ionization step, interesting isotopologue-dependent effects may be observable.





## 5 Conclusion and outlook

In this thesis, we have discussed the strong-field dynamics of molecular ions by the example of the helium hydride molecular ion  $\text{HeH}^+$ . It serves as a simple benchmark system for asymmetric diatomic molecular ions and the fragmentation channels—electron removal (ionization) and dissociation into different electronic configurations—are simple examples of light-induced chemical reactions.

In order to make theoretical predictions via numerical simulations, we have developed a reduced-dimensional model with special potentials that allow our model to accurately reproduce real Born-Oppenheimer potential-energy curves. For this reason, calculations with our model require only moderate computational resources while still avoiding limiting assumptions such as the Born-Oppenheimer approximation. Comparisons with experimental data in section 2.9 support the validity of our model.

We have seen throughout this work that, in general, dynamics of the (active) electron and dynamics of the nuclei cannot be separated from each other in the presence of a strong laser field. Enhanced excitation and enhanced ionization occur when the molecule has stretched to two to four times its equilibrium internuclear distance. If the molecule has the chance to stretch, e. g. via vibrational excitation, this can dramatically increase the ionization probability and change the shape of the kinetic-energy-release (KER) spectrum. As an effect, the ionization probability and KER differ qualitatively between 400 nm and 800 nm laser pulses at low intensities because the latter can induce vibrational excitation whereas the former cannot. We also conclude that in general, high dissociation probabilities facilitate the ionization process.

Furthermore, we have seen that the spatial asymmetry of the molecule can be exploited to control the fragmentation channel: By adding a relatively weak collinearly polarized second harmonic field to the laser pulse, a spatially asymmetric electric field is created and its asymmetry can be controlled via the relative delay or relative phase of the two colors. Both ionization and dissociation yields are sensitive to the relative phase but in contrast to our previous findings this tailored two-color field suppresses ionization when

the dissociation yield is large and vice versa. In other words: The easily controllable relative two-color phase allows to steer the molecule into one of the two fragmentation channels. In our simulations, this effect survives focal-volume averaging and should thus be visible in experiments.

If observables depend on the nuclear motion it is likely that the nuclear reduced mass has an effect. Indeed, isotope effects have been discussed in all chapters of this thesis, usually with the intuitive result that heavier isotopologues such as  $\text{HeD}^+$  move slower and thus show less dissociation, enhanced excitation and ionization. However, isotopologues differ not only in their reduced masses but also the mass distribution within the molecule (or the mass ratio between the nuclei) can vary. We have isolated the effect of the mass ratio by studying artificial isotopologues with fixed reduced mass and looked specifically at the ground-state dissociation process. The main result is that the excitations necessary for vibrational ladder climbing can be effectively forbidden<sup>1</sup> around a certain value of the mass ratio. This suppresses the dissociation probability by many orders of magnitude. These findings are general in the sense that the same effect can occur in other charged molecules if the center of mass is near the charge. If isotopologues are compared, not only the reduced mass but also the mass distribution plays an important role for the coupling to the laser field.

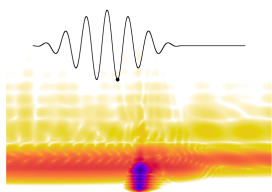
### Future research

In the introduction, we have raised three questions and we have found at least some answers throughout this work. However, science does not stop and new projects may start from this point. While we were lucky to have experimentalists with us who provided data to compare our simulations from chapter 2 to, measurement data to compare with the two-color calculations is still missing. It would be a nice progress if the degree of control that we have found theoretically could also be realized in the lab.

Isotope effects due to the mass distribution in molecular ions have not found much attention so far. Investigations for other molecules than  $\text{HeH}^+$  can be interesting, e. g. the carbon monoxide cation  $\text{CO}^+$ . Its isotopologues  $^{12}\text{C}^{18}\text{O}^+$  and  $^{13}\text{C}^{16}\text{O}^+$  have similar reduced masses and are possible targets for measurements. Also,  $\text{CO}^+$  has multiple electronic states that support

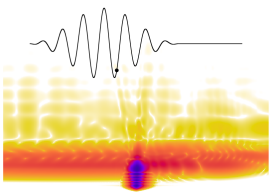
---

<sup>1</sup>In the sense that the transition matrix elements become very small.



vibrational levels. With their different charge distributions these states will likely have different critical mass ratios where the suppression of vibrational transitions is strongest.

It is easy to predict that isotope effects are also important in the case that a freed electron returns to and interacts with the fragmenting  $\text{HeH}^{2+}$  parent ion and the remaining electron during the laser pulse. If the laser intensity is high enough, non-sequential double ionization can occur, i. e. the returning electron leads to removal of the second electron. The internuclear distance at the time of recollision depends on the reduced nuclear mass and thus on the isotopologue. Our single-active-electron model is not able to describe double ionization but it can be extended. In appendix B.2, the two-active-electron version of our reduced-dimensionality model is outlined and the parameter functions for the softened Coulomb potentials are given so that the model again reproduces the real-world potential curves. This model potential is ready to be used for fully correlated two-electron non-Born-Oppenheimer calculations of the strong-field dynamics of  $\text{HeH}^+$ .



# A Born-Oppenheimer approximation

## A.1 General considerations

For some calculations and arguments throughout this thesis we use or refer to the Born-Oppenheimer approximation [131]. Therefore, we derive its main properties here briefly along the lines of [88].

We consider a molecular system with a fixed number of electrons and nuclei. Electrons and nuclei are labeled with indices  $j, k$  and  $A, B$ , respectively, and sums are understood to cover all electrons or nuclei, depending on the index type. In this chapter, we collect coordinates  $\vec{x}_j$  and momenta  $\vec{p}_j$  of all electrons in bold notation  $\mathbf{x}$  and  $\mathbf{p}$ , nuclear coordinates and momenta are written in capital letters  $\vec{X}_A, \vec{P}_A, \mathbf{X}, \mathbf{P}$ . Distances between electrons are denoted as  $r_{jk} = |\vec{x}_j - \vec{x}_k|$  and analogously  $r_{AB}$  for distances between nuclei and  $r_{iA}$  for distances between an electron and a nucleus. Both electron and nuclear spins are ignored here<sup>1</sup>, as well as relativistic contributions. Then, the full Hamiltonian for the molecule in some external interacting field is given by

$$\begin{aligned} H &= H_e + H_n + H_{\text{int}, e}(\mathbf{x}, \mathbf{p}, t) + H_{\text{int}, n}(\mathbf{X}, \mathbf{P}, t), \\ H_e &= \sum_j \frac{\vec{p}_j^2}{2} + V_{ee}(\mathbf{x}) + V_{en}(\mathbf{x}, \mathbf{X}), \\ H_n &= \sum_A \frac{\vec{P}_A^2}{2M_A} + V_{nn}(\mathbf{X}), \\ V_{ee} &= \frac{1}{2} \sum_{j \neq k} \frac{1}{r_{jk}}, \quad V_{en} = - \sum_{j,A} \frac{Z_A}{r_{jA}}, \quad V_{nn} = \frac{1}{2} \sum_{A \neq B} \frac{Z_A Z_B}{r_{AB}}, \end{aligned}$$

where  $Z_A$  and  $M_A$  are nuclear charges and masses, respectively. The interaction  $H_{\text{int}, e}, H_{\text{int}, n}$  can be given in length or velocity gauge, which is why we specify the (possible) dependence on both coordinates and momenta. For fixed nuclei,

---

<sup>1</sup>At this stage, neglecting the spin simply aids notational brevity. There is no need for this simplification but we do not consider spins later anyway.

## A Born-Oppenheimer approximation

we consider *electronic eigenstates*  $\phi_n$  which solve the time-independent field-free Schrödinger equation for the electrons,

$$H_e \phi_n(\mathbf{x}; \mathbf{X}) = E_n(\mathbf{X}) \phi_n(\mathbf{x}; \mathbf{X}), \quad n \in \mathbb{N}. \quad (\text{A.1})$$

Here,  $\phi_n$  is a real-valued square-integrable wave function of electron coordinates  $\mathbf{x}$  and depends parametrically on the nuclear configuration  $\mathbf{X}$ ,  $n$  labels electronic eigenstates and  $E_n(\mathbf{X})$  are *Born-Oppenheimer potential-energy surfaces* (BO-PES). We assume the phases of the the  $\phi_n$  to be chosen such that derivatives with respect to  $\mathbf{X}$  exist<sup>2</sup>. Since the electronic eigenstates form an orthonormal basis,  $\langle \phi_n | \phi_m \rangle_{(x)} = \delta_{nm}$  (subscript  $(x)$  means integration only over  $\mathbf{x}$  coordinates), it is possible to expand any wave function of  $\mathbf{x}$  and  $\mathbf{X}$  as

$$\Psi(\mathbf{x}, \mathbf{X}; t) = \sum_{n \in \mathbb{N}} \phi_n(\mathbf{x}; \mathbf{X}) \psi_n(\mathbf{X}; t). \quad (\text{A.2})$$

Inserting this expansion into the time-dependent Schrödinger equation  $i\partial_t \Psi = H \Psi$  and projecting onto  $\phi_n$  gives a system of coupled differential equations for the time evolution of the  $\psi_n$ ,

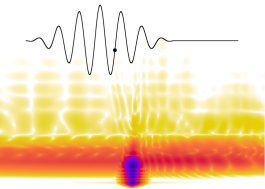
$$i\partial_t \psi_n(\mathbf{X}; t) = \langle \phi_n | H \Psi \rangle_{(x)} =: \left( \mathbf{H}_n \vec{\psi} \right)_n, \quad \vec{\psi} = (\psi_1, \psi_2, \dots), \quad (\text{A.3})$$

where  $\mathbf{H}_n$ <sup>3</sup> is a matrix of operators that is applied to the vector of nuclear wave functions  $\vec{\psi}$ , i. e. the prefactors of  $\psi_n$  in  $\langle \phi_n | H \Psi \rangle_{(x)}$  are the diagonal elements of  $\mathbf{H}_n$  and prefactors of  $\psi_m$  with  $m \neq n$  are off-diagonal coupling terms. Using (A.1) and considering that  $\phi_l$  depends on  $\mathbf{X}$  and thus does not commute with  $\vec{P}_A = -i\nabla_{\vec{X}_A}$ , the scalar product can be split into multiple terms,

$$\begin{aligned} \langle \phi_n | H \Psi \rangle_{(x)} &= \left\langle \phi_n \left| \sum_{m \in \mathbb{N}} (E_m + H_n + H_{\text{int}, e} + H_{\text{int}, n}) (\phi_m \psi_m) \right. \right\rangle_{(x)} \\ &= (E_n(\mathbf{X}) + H_n + H_{\text{int}, n}) \psi_n \\ &\quad + \sum_{m, A} \frac{1}{M_A} \left\langle \phi_n \left| \vec{P}_A \phi_m \right. \right\rangle_{(x)} \cdot \vec{P}_A \psi_m \\ &\quad + \sum_{m, A} \frac{1}{2M_A} \left\langle \phi_n \left| \vec{P}_A^2 \phi_m \right. \right\rangle_{(x)} \psi_m + \sum_m \langle \phi_n | H_{\text{int}, e} \phi_m \rangle_{(x)} \psi_m. \end{aligned} \quad (\text{A.4})$$

<sup>2</sup>Note that there are cases where it is not possible to choose  $\phi_n$  both real and differentiable (cf. Berry phase [132]). For simplicity, we still assume both.

<sup>3</sup>Note the difference between the subscript  $n$  which stands for *nuclear* and the index  $n$  which numbers electronic levels.



From  $\nabla_{\vec{X}_A} |\phi_n|^2 = 2\bar{\phi}_n \nabla_{\vec{X}_A} \phi_n$  it follows that

$$\langle \phi_n | \vec{P}_A \phi_n \rangle_{(x)} = -\frac{i}{2} \nabla_{\vec{X}_A} \langle \phi_n | \phi_n \rangle_{(x)} = 0.$$

Up to this point, there is no approximation (beyond the assumptions explicitly stated above). The *Born-Oppenheimer approximation* is that the scalar products involving  $\vec{P}_A$  in (A.4) can be neglected. Then, the field-free Hamiltonian  $H_n$  is diagonal, i. e. vibrational wave functions evolve independently on all PES,

$$i\partial_t \psi_m(\mathbf{X}; t) = (E_m(\mathbf{X}) + H_n) \psi_m(\mathbf{X}; t), \quad m \in \mathbb{N}. \quad (\text{A.5})$$

To see the validity of the Born-Oppenheimer approximation, we remember that  $\phi_m$  depends on  $\mathbf{X}$  and  $\mathbf{x}$  in a similar way because  $V_{\text{en}}$  depends on the distances  $r_{jA}$ . Thus it is reasonable to assume that the terms  $\vec{P}_A^2 \phi_m$  give contributions that are of similar magnitude as the kinetic-energy term in (A.1) but with prefactors  $1/M_A$  that usually are at least 3 orders of magnitude smaller. The same argument can be applied to  $\vec{P}_A \phi_m$ . It is not easy to make this argument rigorous for the general case [133] and in fact the approximation is not always valid. To see this, we first note that

$$\left[ \vec{P}_A, H_e \right] = \left[ \vec{P}_A, V_{\text{en}} \right] = -i \left( \nabla_{\vec{X}_A} V_{\text{en}} \right) = iZ_A \sum_j \frac{\vec{x}_j - \vec{X}_A}{r_{jA}^3}. \quad (\text{A.6})$$

Then, for  $n \neq m$  the scalar product in the third line of (A.4) can be written as

$$\left\langle \phi_n \left| \vec{P}_A \phi_m \right. \right\rangle_{(x)} = \frac{\left\langle \phi_n \left| \left[ \vec{P}_A, H_e \right] \phi_m \right. \right\rangle_{(x)}}{E_m(\mathbf{X}) - E_n(\mathbf{X})}.$$

Using (A.6), one can see that the numerator as a sum of one-electron matrix elements is finite, i. e. the coupling of vibrational wave functions on different electronic surfaces becomes stronger (and thus the Born-Oppenheimer approximation is not valid) if the PES come close to each other or cross.

## A.2 Two-level Born-Oppenheimer model

If the separation between potential-energy surfaces is large or certain excitation pathways are prohibited—e. g. due to polarization of the laser field—often

it is enough to consider only one or two electronic states, i. e. to truncate the sum (A.2) after one or two terms. We derive the resulting Hamiltonian including the coupling terms and a calculation scheme for time propagation in this section. Let's consider the interaction terms in length gauge and dipole approximation, i. e. the laser pulse is described by its electric field vector  $\vec{E}(t)$  and the interaction Hamiltonian is

$$H_{\text{int, e}}(\mathbf{x}, t) = \sum_j \vec{x}_j \cdot \vec{E}(t) = -\vec{d}_e \cdot \vec{E}(t),$$

$$H_{\text{int, n}}(\mathbf{X}, t) = - \sum_A Z_A \vec{X}_A \cdot \vec{E}(t) = -\vec{d}_n \cdot \vec{E}(t),$$

with dipole operators  $\vec{d}_e$  and  $\vec{d}_n$ . The dipole transition matrix elements for the electronic states  $\phi_n$  are given by

$$\vec{d}_{nm}(\mathbf{X}) = \left\langle \phi_n \left| \vec{d}_e + \vec{d}_n \right| \phi_m \right\rangle_{(x)} = \left\langle \phi_n \left| \vec{d}_e \right| \phi_m \right\rangle_{(x)} + \vec{d}_n \delta_{nm}.$$

Using  $\vec{d}_{nm} = \vec{d}_{mn}$  (for real  $\phi_n, \phi_m$ ), the TDSE reads

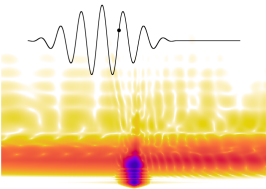
$$i\partial_t \begin{pmatrix} \psi_1(\mathbf{X}; t) \\ \psi_2(\mathbf{X}; t) \end{pmatrix} = \begin{pmatrix} H_1 & -\vec{d}_{12} \cdot \vec{E}(t) \\ -\vec{d}_{12} \cdot \vec{E}(t) & H_2 \end{pmatrix} \begin{pmatrix} \psi_1 \\ \psi_2 \end{pmatrix} =: \mathbf{H}_n^{\text{BO}} \begin{pmatrix} \psi_1 \\ \psi_2 \end{pmatrix} \quad (\text{A.7})$$

with the *nuclear Hamiltonian on the first electronic surface*  $H_1 = H_n + E_1(\mathbf{X}) - \vec{d}_{11} \cdot \vec{E}(t)$  and similarly for  $H_2$ . The matrix  $\mathbf{H}_n^{\text{BO}}$  is the truncated and BO-approximated version of  $\mathbf{H}_n$  in (A.3). Obviously, in the field-free case (A.7) reduces to (A.5). Numerical solutions for the TDSE (A.7) can be obtained conveniently by the following procedure. We want to apply the short-time propagator  $\exp(-i\mathbf{H}_n^{\text{BO}}\Delta t)$ . To this end, we split the  $2 \times 2$  matrix  $\mathbf{H}_n^{\text{BO}}$  into a diagonal part  $\mathbf{H}_d$  and an anti-diagonal coupling part  $\mathbf{H}_c$ ,

$$\mathbf{H}_n^{\text{BO}} = \mathbf{H}_d + \mathbf{H}_c = \begin{pmatrix} H_1 & \\ & H_2 \end{pmatrix} - \vec{d}_{12} \cdot \vec{E}(t) \begin{pmatrix} & 1 \\ 1 & \end{pmatrix}.$$

The diagonal matrix  $\mathbf{H}_d$  and its exponential  $\exp(-i\mathbf{H}_d\Delta t)$  acts on each  $\psi_n$  separately and can be implemented with any TDSE solver, e. g. the split-operator method. The matrix exponential of the coupling term  $\mathbf{H}_c$  between electronic states can be easily calculated. From

$$\mathbf{H}_c^2 = \left( \vec{d}_{12} \cdot \vec{E}(t) \right)^2 \begin{pmatrix} 1 & \\ & 1 \end{pmatrix}$$





it follows that

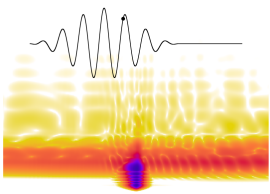
$$\begin{aligned}
e^{-i\mathbf{H}_c\Delta t} &= \sum_n \frac{(-i\mathbf{H}_c\Delta t)^n}{n!} \\
&= \cos\left(\vec{d}_{12} \cdot \vec{E}(t)\Delta t\right) \begin{pmatrix} 1 & \\ & 1 \end{pmatrix} + i \sin\left(\vec{d}_{12} \cdot \vec{E}(t)\Delta t\right) \begin{pmatrix} & 1 \\ 1 & \end{pmatrix}.
\end{aligned}$$

Then, the full short-time propagator can be split using the split-operator formula,

$$e^{-i\mathbf{H}_n^{\text{BO}}\Delta t} = e^{-i\mathbf{H}_c\Delta t/2} e^{-i\mathbf{H}_d\Delta t} e^{-i\mathbf{H}_c\Delta t/2} + \mathcal{O}(\Delta t^3)$$

where each of the operators can be applied easily.

Extending this to a general multi-level propagation scheme is in principle straightforward except that  $\mathbf{H}_c$  is a general symmetric matrix with zeros on the diagonal. Factoring out the time-dependent part  $\vec{E}(t)$  allows to calculate the rotation (matrix of eigenvectors) that diagonalizes  $\mathbf{H}_c$ . This has to be done only once, the calculation of  $\exp(-i\mathbf{H}_c\Delta t)$  in every time step is then achieved by simple matrix multiplication.



## B Fine-tuning of soft-core parameters

### B.1 Parameters for one-electron model

In numerical calculations the Coulomb potential is often softened, i. e. the singularity is removed. Except for nuclear-nuclear repulsion, we always use potentials of the form

$$V_\alpha(x) = \frac{q_1 q_2}{\sqrt{|x_1 - x_2|^2 + \alpha}},$$

where  $\alpha > 0$  is the *soft-core parameter*,  $q_i$  are the charges and  $x_i$  are the locations of the charges.

We note that the softened potential is monotonic in  $\alpha$ , more precisely

$$|V_\alpha(x)| > |V_{\alpha'}(x)| \quad \forall x \in \mathbb{R}, \forall \alpha' > \alpha. \quad (\text{B.1})$$

We consider the reduced-dimensionality model of  $\text{HeH}^+$  in field-free Born-Oppenheimer approximation. Since the location of the center of mass is not important, we choose the origin centered between the nuclei such that the nuclei with charges  $Z_1, Z_2$  are located at  $x = \mp R/2$ .

Within the single-active-electron approximation and for fixed nuclei (i. e. neglecting the kinetic-energy term for the nuclei), the Hamiltonian reads

$$\begin{aligned} H &= \frac{p^2}{2} + V_{\text{ion}}(R) + V_{\text{H}}(x; R) + V_{\text{He}}(x; R) \\ &= \frac{p^2}{2} + V_{\text{ion}}(R) + \frac{-Z_1}{\sqrt{(x + R/2)^2 + \alpha_1(R)}} + \frac{-Z_2}{\sqrt{(x - R/2)^2 + \alpha_2(R)}}. \end{aligned} \quad (\text{B.2})$$

Since we assume the inactive electron to be located at the helium core, the effective nuclear charges are  $Z_1 = Z_2 = 1$ . This has the effect that the eigenenergies of (B.2) are symmetric with respect to exchange of  $\alpha_1$  and  $\alpha_2$ . We fix the orientation of the molecule to H-He by choosing  $\alpha_1 > \alpha_2$  (helium at  $x = +R/2$  has the deeper potential well).  $V_{\text{ion}}(R)$  is the BO-PEC of the ground state

Table B.1: Numeric values of polarizabilities together with their sources.

quantity	value (a. u.)	source
$\alpha_{\text{D,He}}$	1.383 746	[135]
$\alpha_{\text{D,H}}$	4.5	[136] <sup>3</sup>
$\alpha_{\text{D,He}^+}$	0.281 187 8	[137]

( $1s\sigma$ ) of  $\text{HeH}^{2+}$ ; we use literature data from [84, Table 4]. It roughly equals  $1/R - 2$  a.u. except for small internuclear distances. For the calculation of soft-core parameters in this chapter, we subtract the  $2/R$  nuclear repulsion from  $V_{\text{ion}}(R)$  which makes it finite for  $R \rightarrow 0$ .

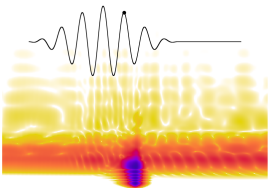
Our goal is now to tune  $\alpha_1$  and  $\alpha_2$  for each  $R$  so that the two lowest eigenenergies  $E_0, E_1$  of (B.2) reproduce the literature values for the two lowest singlet BO curves<sup>1</sup>. We use the ground-state energies from [81, Table II] and combine data from [82, Table V], [83, Table III] and from additional calculations using the framework of [81]<sup>2</sup> for the energies of the first excited state.

### Asymptotic behaviour of potential-energy curves

For  $R \rightarrow \infty$ , we use the asymptotic behaviour instead of data points from the literature: In the ground state,  $\text{HeH}^+$  dissociates into  $\text{He} + \text{H}^+$  and thus  $E_0(R)$  approaches the ionization potential of helium in lowest order as  $-\frac{1}{2}\alpha_{\text{D,He}}/R^4$  with the dipole polarizability of helium  $\alpha_{\text{D,He}}$ . In the first excited state, it dissociates into  $\text{He}^+ + \text{H}$  with energy  $-2 - 0.5 = -2.5$  (here, we know analytically that  $\alpha_1(\infty) = 2$  gives the correct hydrogen ground-state energy  $-0.5$  [134]). The lowest-order approximation of the asymptotic behaviour is given by  $-\frac{1}{2}\alpha_{\text{D,H}}/R^4$  with the dipole polarizability of hydrogen  $\alpha_{\text{D,H}}$ . The ionized system  $\text{HeH}^{2+}$  dissociates into  $\text{He}^+ + \text{H}^+$  in its ground state and thus the lowest-order term for the energy is  $1/R$ . For consistency, we also include the induced dipole shift and approximate the asymptotic behaviour to the same order in  $1/R$  as the other energies by  $1/R - \frac{1}{2}\alpha_{\text{D,He}^+}/R^4$  with the dipole polarizability of  $\text{He}^+$   $\alpha_{\text{D,He}^+}$ . The values of the polarizabilities are given in table B.1.

<sup>1</sup>We only consider singlet states because we start in a singlet state and in dipole approximation the laser field does not couple to the electron spin.

<sup>2</sup>I am grateful for the support from Magda Zientkiewicz and Krzysztof Pachucki who provided the data to me.



For  $R \rightarrow 0$ , we end up with a  $\text{Li}^+$  ion. Because  $\text{Li}^{2+}$  is hydrogen-like, we have  $V_{\text{ion}}(0) = 9/2$ , and the ground- and excited-state energies of  $\text{Li}^+$  can be looked up from atomic-spectra databases [73]. The combined BO PEC are shown in figure B.1. It is the same as figure 2.1 but without the  $2/R$  nuclear repulsion. In this plot, the potential minimum at the equilibrium distance  $R \approx 1.46$  a.u. is not obvious.

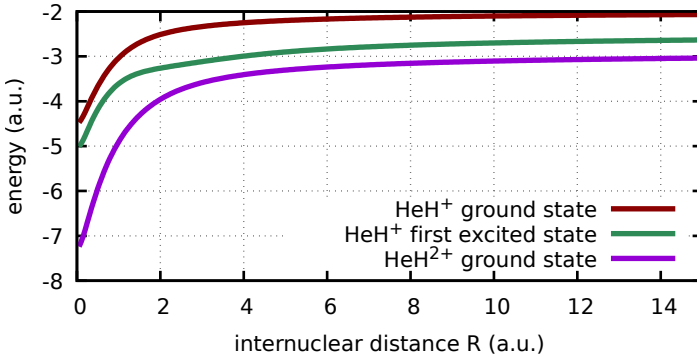


Figure B.1: Born-Oppenheimer potential-energy curves  $V_{\text{ion}}(R)$ ,  $E_0(R)$  and  $E_1(R)$  without  $2/R$  nuclear repulsion. Data collected, interpolated and sampled from [81–84] as described in the text.

### Calculation of optimized soft-core parameters

Once the input data  $V_{\text{ion}}(R)$ ,  $E_0(R)$  and  $E_1(R)$  is known, it is straightforward to calculate  $\alpha_1(R)$  and  $\alpha_2(R)$  by applying Newton’s algorithm on the  $\alpha_1$ - $\alpha_2$  plane<sup>4</sup>, calculating the lowest two eigenstates in each step, e. g. by imaginary-time evolution [138]. This is fast and accurate because the internuclear distance is fixed and the eigenstate calculation is thus one-dimensional. It is useful to use the results for one value of  $R$  as initial guess for the neighbouring  $R$  value.

The resulting curves for  $\alpha_1$  and  $\alpha_2$  are printed in table B.2 and displayed in figure B.2. For most internuclear distances, the potential wells have a constant shape/depth because  $\alpha_1$  and  $\alpha_2$  are almost constant. Only for small

<sup>3</sup>This is the exact value for non-relativistic hydrogen.

<sup>4</sup>One can work on the  $\ln(\alpha_1)$ - $\ln(\alpha_2)$  plane instead which at the same time restricts  $\alpha$  to positive values and conveniently allows to have one value very large and the other one very small.

## B Fine-tuning of soft-core parameters

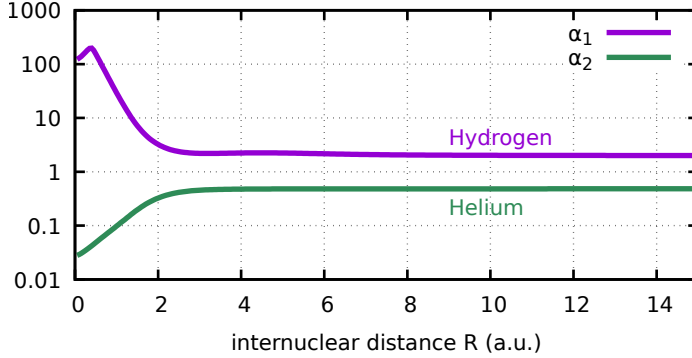


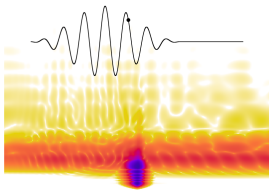
Figure B.2: Tuned soft-core parameters  $\alpha_1(R)$  and  $\alpha_2(R)$ .

separations the helium well becomes quite a bit deeper ( $\alpha_2$  decreases).  $\alpha_1$  reaches relatively large values but this is not problematic since it just makes the hydrogen potential very shallow.

Using these parameter curves in (B.2) guarantees that our very simple one-dimensional model exactly reproduces at least the two lowest potential-energy curves of  $\text{HeH}^+$  and the vertical ionization potential.

Table B.2: Numerical values of input and output data of the described procedure on an internuclear-distance grid with 0.05 a.u. grid spacing up to  $R = 6$  a.u. and 0.5 a.u. for larger  $R$ . Input: Ground- and excited-state energies  $E_0$ ,  $E_1$  of  $\text{HeH}^+$  and ground-state energy  $V_{\text{ion}}$  of  $\text{HeH}^{2+}$  (see text for sources). All energies without  $2/R$  nuclear repulsion. Output: Softening parameters  $\alpha_1$ ,  $\alpha_2$ .

R	$E_0$	$E_1$	$V_{\text{ion}}$	$\alpha_1$	$\alpha_2$
0.00	-7.279 72	-5.040 85	-4.5	120.799 230 040 902 30	2.764 153 800 545 884 2 $\times 10^{-2}$
0.05	-7.238 579 770 146 289 5	-5.014 005 732 419 525 1	-4.474 230 881 480 234 1	122.557 618 913 516 95	2.807 205 178 632 607 1 $\times 10^{-2}$
0.10	-7.138 448 755 973 120 0	-4.947 578 634 999 998 4	-4.411 316 871 487 636 1	129.751 990 145 855 87	2.912 163 324 846 685 2 $\times 10^{-2}$
0.15	-7.004 899 622 664 794 4	-4.859 366 057 540 786 0	-4.327 375 492 358 932 3	138.725 292 023 247 22	3.061 798 254 764 795 7 $\times 10^{-2}$
0.20	-6.853 138 599 446 220 2	-4.759 422 621 199 999 7	-4.232 694 714 478 920 0	151.331 711 331 803 58	3.245 577 883 161 991 6 $\times 10^{-2}$
0.25	-6.694 701 366 517 122 7	-4.655 035 769 348 386 6	-4.133 650 926 966 653 9	165.339 704 453 714 15	3.453 310 768 836 700 3 $\times 10^{-2}$
0.30	-6.535 287 039 387 886 1	-4.550 075 329 666 666 1	-4.034 134 906 133 936 7	181.313 079 689 370 68	3.680 939 162 685 676 5 $\times 10^{-2}$
0.35	-6.378 690 471 980 974 1	-4.447 550 181 194 828 6	-3.936 482 362 865 090 2	195.916 781 732 739 11	3.927 340 928 991 630 84 $\times 10^{-2}$
0.40	-6.226 926 036 556 521 1	-4.350 443 024 099 999 6	-3.842 058 126 972 948 4	198.299 192 443 004 24	4.199 690 346 853 912 6 $\times 10^{-2}$
0.45	-6.081 354 180 337 335 4	-4.260 945 263 001 457 5	-3.751 619 672 280 606 1	180.144 981 281 858 29	4.506 659 522 124 674 41 $\times 10^{-2}$
0.50	-5.942 500 132 059 320 7	-4.178 109 299 200 000 0	-3.665 543 943 731 378 8	154.188 840 735 951 29	4.844 743 762 811 318 9 $\times 10^{-2}$
0.55	-5.810 607 894 758 277 3	-4.100 503 013 611 837 7	-3.583 969 873 659 024 0	130.845 796 543 490 96	5.206 229 175 959 541 8 $\times 10^{-2}$
0.60	-5.685 631 787 156 554 0	-4.027 895 208 933 333 7	-3.506 888 621 505 817 5	110.922 462 442 591 20	5.590 867 602 401 270 6 $\times 10^{-2}$
0.65	-5.567 425 441 285 179 1	-3.960 302 804 564 883 2	-3.434 201 098 903 513 7	93.774 079 004 115 748	6.000 876 414 497 117 3 $\times 10^{-2}$
0.70	-5.455 729 426 723 375 6	-3.897 534 264 942 856 4	-3.365 754 807 636 653 5	79.202 042 987 614 959	6.438 021 361 601 011 0 $\times 10^{-2}$
0.75	-5.350 249 226 136 308 6	-3.839 353 377 922 677 2	-3.301 367 463 078 567 0	66.938 693 006 842 342	6.904 174 012 862 025 8 $\times 10^{-2}$
0.80	-5.250 663 036 984 721 4	-3.785 553 679 999 999 6	-3.240 842 100 894 590 2	56.630 863 139 810 437	7.402 085 170 663 939 84 $\times 10^{-2}$
0.85	-5.156 643 615 356 569 1	-3.735 931 297 462 068 2	-3.183 976 656 133 368 4	47.960 777 036 870 503	7.935 120 757 210 957 5 $\times 10^{-2}$













## B.2 Parameters for two-electron model

R	$E_0$	$E_1$	$V_{\text{ion}}$	$\alpha_1$	$\alpha_2$
94.50	-2.924 888 406 873 734 0	-2.521 164 049 377 412 1	-2.010 582 012 344 957 8	2.000 017 705 369 232 5	0.482 749 237 102 338 86
95.00	-2.924 777 017 107 452 5	-2.521 052 659 203 044 7	-2.010 526 317 515 597 8	2.000 017 424 498 296 7	0.482 749 241 986 093 81
95.50	-2.924 666 793 728 967 7	-2.520 942 435 427 072 9	-2.010 471 205 878 739 7	2.000 017 149 433 133 6	0.482 749 246 769 320 91
96.00	-2.924 557 718 513 397 7	-2.520 833 359 824 286 9	-2.010 416 668 321 985 5	2.000 016 879 376 954 8	0.482 749 251 452 627 70
96.50	-2.924 449 773 613 580 4	-2.520 725 414 547 206 9	-2.010 362 695 921 795 1	2.000 016 616 604 948 0	0.482 749 256 044 662 34
97.00	-2.924 342 941 550 339 2	-2.520 618 582 116 350 9	-2.010 309 279 938 621 5	2.000 016 358 229 156 1	0.482 749 260 541 505 63
97.50	-2.924 237 205 203 045 9	-2.520 512 845 410 797 0	-2.010 256 411 812 189 7	2.000 016 105 476 216 2	0.482 749 264 947 924 92
98.00	-2.924 132 547 800 476 3	-2.520 408 187 659 036 1	-2.010 204 083 156 923 9	2.000 015 857 847 848 6	0.482 749 269 265 871 19
98.50	-2.924 028 952 911 939 4	-2.520 304 592 430 103 5	-2.010 152 285 757 515 6	2.000 015 615 220 174 7	0.482 749 273 497 651 07
99.00	-2.923 926 404 438 678 8	-2.520 202 043 624 978 1	-2.010 101 011 564 621 4	2.000 015 377 523 667 3	0.482 749 277 645 387 28
99.50	-2.923 824 886 605 534 5	-2.520 100 525 468 244 7	-2.010 050 252 690 694 3	2.000 015 144 618 166 2	0.482 749 281 711 189 80
100.00	-2.923 724 383 952 849 9	-2.520 000 022 500 000 1	-2.010 000 001 405 939 2	2.000 014 915 921 101 8	0.482 749 285 696 419 62
100.50	-2.923 624 881 328 625 4	-2.519 900 519 568 007 1	-2.009 950 250 134 386 9	2.000 014 692 715 586 4	0.482 749 289 604 887 50
101.00	-2.923 526 363 880 903 0	-2.519 802 001 820 077 7	-2.009 900 991 450 089 6	2.000 014 473 467 952 6	0.482 749 293 436 686 21
101.50	-2.923 428 817 050 375 3	-2.519 704 454 696 682 0	-2.009 852 218 073 422 0	2.000 014 258 553 268 3	0.482 749 297 194 170 65
102.00	-2.923 332 226 563 212 0	-2.519 607 863 923 777 1	-2.009 803 922 867 497 8	2.000 014 047 991 792 9	0.482 749 300 879 261 54

## B.2 Parameters for two-electron model

We can remove the single-active-electron approximation from our model by including the second electron in the Hamiltonian, leading to a two-active-electron (TAE) model. As the fixed-nuclei TAE Hamiltonian, i. e. the analogue to (B.2), we propose

$$\begin{aligned}
 H_{\text{HeH}^+} = & \frac{p_1^2}{2} + \frac{p_2^2}{2} + V_{\text{H}}(x_1; R) + V_{\text{He}}(x_1; R) + V_{\text{H}}(x_2; R) + V_{\text{He}}(x_2; R) \\
 & + V_{ee}(x_1, x_2; R) + V_{\text{H-He}}(R)
 \end{aligned} \tag{B.3}$$

using the potentials

$$\begin{aligned}
 V_{\text{H}}(x) &= \frac{-Z_1}{\sqrt{(x + R/2)^2 + \alpha_1(R)}} \\
 V_{\text{He}}(x) &= \frac{-Z_2}{\sqrt{(x - R/2)^2 + \alpha_2(R)}} \\
 V_{ee}(x_1, x_2) &= \frac{1}{\sqrt{(x_1 - x_2)^2 + \beta(R)}} \\
 V_{\text{H-He}} &= \frac{Z_1 Z_2}{R}.
 \end{aligned}$$

Here,  $x_1$  and  $x_2$  are the coordinates of the two electrons and the nuclei are located at  $\pm R/2$  as before. The charge of the helium nucleus is not shielded by an inactive electron anymore, therefore we have  $Z_1 = 1$ ,  $Z_2 = 2$ . Instead of the literature potential values  $V_{\text{ion}}(R)$  in (B.2), the nuclear repulsion is included in

the exact term  $V_{\text{H-He}}$ . In fixed-nuclei calculations, it is constant and can be omitted. It is, however, important for calculations including nuclear motion.

It may seem counterintuitive that the electron-electron repulsion  $V_{ee}$  depends on the internuclear distance. The reason for introducing the  $R$ -dependent function  $\beta(R)$  is that we still want to reproduce three Born-Oppenheimer curves which in general requires three tunable functions. We can consider the model reasonable if  $\beta(R)$  does not vary too much and if it is constant for large internuclear distance.

If one electron has been removed from the molecule, the reduced system can be described by the following Hamilton operator (which follows from (B.3) via  $x := x_1$  and  $x_2 \rightarrow \infty$ ).

$$H_{\text{HeH}^{2+}} = \frac{p^2}{2} + V_{\text{H}}(x) + V_{\text{He}}(x) + V_{\text{H-He}}$$

Similar to the SAE model, we tune the soft-core parameter functions  $\alpha_1(R)$ ,  $\alpha_2(R)$  and  $\beta(R)$  such that the model reproduces the two lowest Born-Oppenheimer potential-energy curves of  $\text{HeH}^+$  and the ground-state BO PEC of  $\text{HeH}^{2+}$ . Explicitly, we solve the time-independent Schrödinger equations

$$H_{\text{HeH}^+} \psi(x_1, x_2; R) = E(R) \psi(x_1, x_2; R) \quad (\text{B.4})$$

and

$$H_{\text{HeH}^{2+}} \chi(x; R) = E_{\text{ion}}(R) \chi(x; R) \quad (\text{B.5})$$

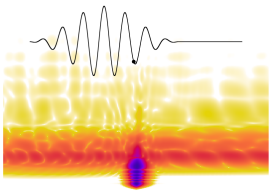
for each value of the internuclear distance  $R$ .

In the following, first we consider how to solve the eigenvalue equations (B.4) and (B.5). Then, we develop a strategy for optimizing the parameters functions.

## Solving the eigenvalue problems

The eigenenergy calculation for  $\text{HeH}^{2+}$ , i. e. the solution of eq. (B.5) is easy: It is an ordinary differential equation (depending only on  $x$  as a variable) which can be perfectly solved using the shooting method with Numerov integration [139, 140]. The ground-state energy is the largest energy for which “shooting” gives a wave function without nodes.

Solving (B.4) is harder. Since we are not interested in all eigenvalues but only the lowest two, diagonalization of the Hamiltonian (which can be a



large matrix, depending on the grid sizes for  $x_1$  and  $x_2$ ) is wasteful. Instead, iterative algorithms such as imaginary-time evolution [138] or the power method [124, 141] can be applied.<sup>5</sup> A numerically two-dimensional operator has to be evaluated many times which is relatively expensive compared to the calculation of eigenstates of  $H_{\text{HeH}^{2+}}$ . The excited state and its energy can be calculated by projecting out the ground state during the iteration.

Summarizing these considerations, the calculation of  $E_{\text{ion}}$  is easy whereas  $E_0$  and  $E_1$  are much harder with  $E_1$  being slightly more expensive because of the projections.

## Physical intuition

In order to optimize the tuning algorithm for the soft-core parameters, we investigate how they affect the different eigenenergies if the eigenstates are close to the real-world situation. For large internuclear distance, the three relevant eigenstates can be characterized as follows.

$E_0$ : In the ground state of  $\text{HeH}^+$ , both electrons are located at the helium core. Therefore, the ground-state energy is sensitive to  $\alpha_2$  (the softening parameter for helium) and  $\beta$  (the softening parameter for the electron-electron interaction), but not very sensitive to  $\alpha_1$ .

$E_1$ : In the excited state, one of the electrons has moved to the hydrogen core and the electrons are thus far apart.<sup>6</sup> Therefore, the excited-state energy depends on both  $\alpha_1$  and  $\alpha_2$ , but not very strongly on  $\beta$ .

$E_{\text{ion}}$ : In the ground state of the ionized system, the single electron is located at the helium core. Since there is no electron-electron interaction, the energy does not depend on  $\beta$  at all.  $E_{\text{ion}}$  depends sensitively on  $\alpha_2$  and only very weakly on  $\alpha_1$ .

Most of these considerations apply only “close to the real situation”. As an example: The “real” excited state (i. e. one electron at He and H each) can become the ground state of the model system if  $\beta$  gets very small because in this case the electron-electron interaction becomes very strong which increases the energy of the “real” ground state where both electrons are located at the helium site. In this case, the ground-state energy in the model is also sensitive

<sup>5</sup>Power method here means to apply the shifted operator  $H_{\text{HeH}^+} + \lambda$  repeatedly to a randomly initialized state. The shift  $\lambda$  is chosen such that all eigenvalues are negative. This procedure converges towards the ground state.

<sup>6</sup>The wave function of course is still symmetric with respect to  $x_1 \leftrightarrow x_2$ .

to  $\alpha_1$ . This kind of pitfalls can lead to undesired behaviour if the algorithms are not restricted to physically reasonable parameter ranges.

### Calculating the soft-core parameter

We restrict the parameters  $\alpha_1, \alpha_2, \beta$  to positive values with the parametrization

$$\alpha_1 = \exp(\lambda_1) \quad \alpha_2 = \exp(\lambda_2) \quad \beta = \exp(\lambda_3)$$

and we only use  $\lambda_i$  in the following. Consider the following function

$$f : \begin{pmatrix} \lambda_1 \\ \lambda_2 \\ \lambda_3 \end{pmatrix} \mapsto \begin{pmatrix} E_0 \\ E_1 \\ E_{\text{ion}} \end{pmatrix},$$

assuming that each of the eigenenergies has been shifted by the correct value from the literature. The sought-after parameters then are the solution of

$$f(\lambda_1, \lambda_2, \lambda_3) = 0. \tag{B.6}$$

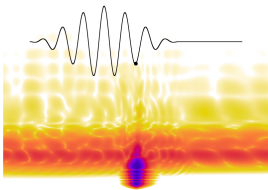
One could apply a general root-finding algorithm in three dimensions (e. g. the generalized Newton's method), but in the following we construct in three steps a specialized algorithm that uses the physical intuition.

#### The ionized problem: $\lambda_1(\lambda_2)$

For any given  $\lambda_2$ , we can easily calculate  $\lambda_1$  (and vice versa): For fixed  $\lambda_2, E_{\text{ion}}$  depends monotonically on  $\lambda_1$  (cf. (B.1)), so once two bounds for  $\lambda_1$  are found (with differing sign of  $E_{\text{ion}}$ ), a simple bisection or secant method converges quickly.

This works as long as  $\lambda_2$  is not too small. If that is the case,  $E_{\text{ion}}$  cannot be made positive, no matter how large  $\lambda_1$  is. This indicates that this small value of  $\lambda_2$  cannot solve (B.6). If it works, this defines a function  $\lambda_1(\lambda_2)$  which is not too expensive to evaluate.

Although all components of  $f(\lambda_1, \lambda_2, \lambda_3)$  are monotonic in  $\lambda_2$ , this is no longer true for  $\lambda_2 \mapsto f(\lambda_1(\lambda_2), \lambda_2, \lambda_3)$ . This function can have local extrema which can severely disturb Newton's algorithm.



**The ground-state energy:  $\lambda_3(\lambda_2)$** 

The ground-state energy is still monotonic in  $\lambda_3$  for fixed  $\lambda_1$  and  $\lambda_2$ . Therefore, for fixed  $\lambda_2$ , it is possible to calculate the root of

$$\lambda_3 \mapsto E_0(\lambda_1(\lambda_2), \lambda_2, \lambda_3)$$

similarly to the procedure outlined in the previous section. The major difference is that instead of solving a one-dimensional eigenvalue problem, in every step a two-dimensional eigenstate has to be found. If we use iterative algorithms for that, only an approximation to that state is calculated, i. e. the degree of convergence can influence the results. Also, the effort is much higher to calculate these states than for the one-dimensional case.

Anyway, this gives a function  $\lambda_3(\lambda_1, \lambda_2)$  which can already take minutes to hours to evaluate, depending on the grid size and convergence criteria. Again, for some values of  $\lambda_2$  it may be impossible to find a suitable  $\lambda_3$ . A good starting value for  $\lambda_2$  and small steps help to avoid that situation.

**Final stage: find  $\lambda_2$** 

Given some value of  $\lambda_2$ , the functions  $\lambda_1(\lambda_2)$  and  $\lambda_3(\lambda_2)$  give results which guarantee that  $E_0$  and  $E_{\text{ion}}$  are reproduced, if possible. This leaves a one-dimensional function

$$\lambda_2 \mapsto E_1(\lambda_1(\lambda_2), \lambda_2, \lambda_3(\lambda_2))$$

which is not only not monotonic, but can also have a very large derivative. Therefore, at a zero-crossing it can effectively jump from positive to negative values and Newton's algorithm is not very useful here. Instead, it proved useful to look at some starting value for  $\lambda_2$  and neighbouring values, alternating between larger and smaller values while increasing the difference to the starting value. Once a sign change of  $E_1$  is detected, the secant (or regula falsi) method is used within the found bounds.

As long as the starting value is not too bad, this usually converges quickly. It is useful to calculate soft-core parameters for neighbouring values of  $R$  one after the other and use the previous parameters as initial values for the next step. Also, it makes sense to reuse the eigenstates corresponding to  $E_0$  and  $E_1$ , respectively, to speed up the convergence if the parameters have been changed only slightly.

## B Fine-tuning of soft-core parameters

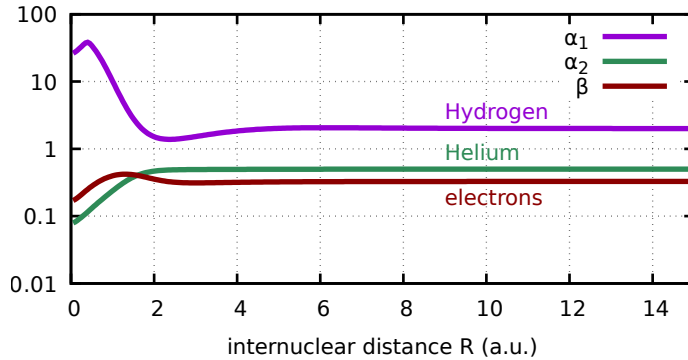


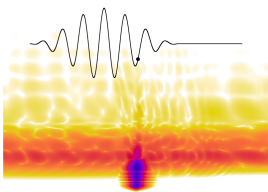
Figure B.3: Tuned soft-core parameters  $\alpha_1(R)$ ,  $\alpha_2(R)$  and  $\beta(R)$ .

### Resulting soft-core parameters

The described algorithm uses the same potential-energy curves as the input as the SAE model. Their values are printed in table B.2. The results of these calculations are shown in figure B.3. It is not guaranteed that the solution is unique but the displayed parameters reproduce the three energy curves and they are physically reasonable.  $\alpha_1$  and  $\alpha_2$  are similar (but not identical) to their counterparts in the single-active-electron model, cf. figure B.2. The softening of the electron-electron repulsion varies with the internuclear distance but does not take extreme values and it flattens for large  $R$  in agreement with our initial considerations. That  $\beta(R)$  takes its maximum value close to the equilibrium distance of  $\text{HeH}^+$  has no direct physical explanation; it is just necessary in order to produce correct energies. The numerical values of the three soft-core parameters as a function of the internuclear distance are printed in table B.3.

Table B.3: Numerical values of the resulting softening parameters  $\alpha_1$ ,  $\alpha_2$ ,  $\beta$  of the described procedure on an internuclear-distance grid with 0.05 a.u. grid spacing up to  $R = 6$  a.u. and 0.5 a.u. for larger  $R$ .

R	$\alpha_1$	$\alpha_2$	$\beta$
0.05	26.374 716 394 859 085	7.932 316 297 922 131 8 $\times 10^{-2}$	0.171 054 377 972 186 78
0.10	27.531 007 105 865 097	8.215 025 823 332 450 2 $\times 10^{-2}$	0.177 473 423 642 548 14
0.15	29.014 155 922 901 207	8.614 524 942 862 147 9 $\times 10^{-2}$	0.186 537 956 477 529 49
0.20	30.917 976 659 641 507	9.093 432 219 049 202 3 $\times 10^{-2}$	0.197 082 297 256 623 18
0.25	33.041 357 431 250 297	9.633 551 175 771 072 6 $\times 10^{-2}$	0.209 132 671 996 239 44
0.30	35.379 057 619 688 304	0.102 214 579 564 383 39	0.222 191 605 643 154 68





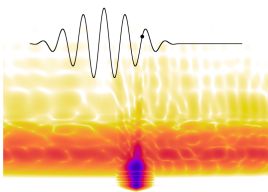






## B Fine-tuning of soft-core parameters

R	$\alpha_1$	$\alpha_2$	$\beta$
54.50	1.999 855 187 046 600 6	0.500 010 973 784 968 50	0.328 291 190 325 496 36
55.00	1.999 853 457 273 078 8	0.500 011 027 867 872 66	0.328 291 268 596 224 87
55.50	1.999 851 790 948 050 4	0.500 011 078 935 532 54	0.328 291 346 866 971 98
56.00	1.999 850 185 052 106 2	0.500 011 128 175 653 41	0.328 291 425 137 737 74
56.50	1.999 848 636 439 522 3	0.500 011 176 787 333 42	0.328 291 503 408 522 20
57.00	1.999 847 142 870 995 4	0.500 011 223 734 184 16	0.328 291 581 679 325 32
57.50	1.999 845 702 328 542 5	0.500 011 267 970 010 16	0.328 291 659 950 147 09
58.00	1.999 844 312 119 118 9	0.500 011 310 679 662 76	0.328 291 738 220 987 51
58.50	1.999 842 969 755 723 4	0.500 011 353 038 610 88	0.328 291 816 491 846 58
59.00	1.999 841 673 507 890 8	0.500 011 393 995 112 19	0.328 291 894 762 724 30
59.50	1.999 840 421 680 715 7	0.500 011 432 498 900 90	0.328 291 973 033 620 73
60.00	1.999 839 218 742 353 5	0.500 011 469 713 760 65	0.328 292 012 169 075 94
60.50	1.999 838 042 847 039 3	0.500 011 506 802 233 61	0.328 292 090 440 000 35
61.00	1.999 836 912 313 903 0	0.500 011 542 709 204 34	0.328 292 129 575 469 55
61.50	1.999 835 819 368 243 7	0.500 011 576 364 317 26	0.328 292 207 846 421 94
62.00	1.999 834 762 098 330 6	0.500 011 608 929 231 35	0.328 292 246 981 905 12
62.50	1.999 833 738 825 683 0	0.500 011 641 553 729 57	0.328 292 325 252 885 54
63.00	1.999 832 748 402 800 2	0.500 011 673 172 716 00	0.328 292 364 388 382 72
63.50	1.999 831 789 851 358 5	0.500 011 702 712 841 90	0.328 292 403 523 884 56
64.00	1.999 830 863 502 293 0	0.500 011 731 320 351 26	0.328 292 481 794 902 28
64.50	1.999 829 962 237 240 4	0.500 011 760 146 469 75	0.328 292 520 930 418 11
65.00	1.999 829 090 847 143 0	0.500 011 788 110 062 75	0.328 292 560 065 938 65
65.50	1.999 828 250 487 850 0	0.500 011 814 130 990 16	0.328 292 599 201 463 81
66.00	1.999 827 428 463 316 8	0.500 011 839 357 039 41	0.328 292 638 336 993 68
66.50	1.999 826 635 211 532 8	0.500 011 864 926 998 67	0.328 292 677 472 528 16
67.00	1.999 825 865 101 674 3	0.500 011 889 755 194 84	0.328 292 755 743 611 22
67.50	1.999 825 118 756 609 4	0.500 011 912 762 338 58	0.328 292 794 879 159 74
68.00	1.999 824 394 653 800 4	0.500 011 935 080 944 88	0.328 292 834 014 712 88
68.50	1.999 823 691 619 930 3	0.500 011 957 849 825 22	0.328 292 834 014 712 88
69.00	1.999 823 009 154 093 2	0.500 011 979 983 220 44	0.328 292 873 150 270 73
69.50	1.999 822 346 891 406 5	0.500 012 000 387 951 02	0.328 292 912 285 833 24
70.00	1.999 821 703 756 661 9	0.500 012 020 200 005 46	0.328 292 951 421 400 41
70.50	1.999 821 078 766 922 6	0.500 012 040 550 602 89	0.328 292 990 556 972 25
71.00	1.999 820 472 411 652 8	0.500 012 060 347 831 63	0.328 293 029 692 548 75
71.50	1.999 819 881 890 998 7	0.500 012 078 499 866 29	0.328 293 068 828 129 92
72.00	1.999 819 312 041 807 5	0.500 012 096 138 137 13	0.328 293 107 963 715 75
72.50	1.999 818 751 248 918 3	0.500 012 114 391 418 24	0.328 293 107 963 715 75
73.00	1.999 818 209 223 889 0	0.500 012 132 162 083 73	0.328 293 147 099 306 24
73.50	1.999 817 682 386 803 9	0.500 012 148 358 763 18	0.328 293 186 234 901 39
74.00	1.999 817 169 922 318 2	0.500 012 164 107 863 64	0.328 293 186 234 901 39
74.50	1.999 816 671 101 760 0	0.500 012 180 531 492 43	0.328 293 225 370 501 26
75.00	1.999 816 185 688 646 5	0.500 012 196 537 498 51	0.328 293 264 506 105 74

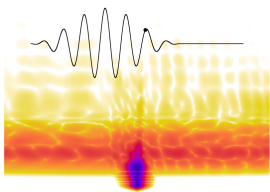


# Bibliography

- [1] Joseph Fraunhofer. “Bestimmung des Brechungs- und des Farbenzerstreungs-Vermögens verschiedener Glasarten, in Bezug auf die Vervollkommnung achromatischer Fernröhre”. In: *Annalen der Physik* 56.7 (1817), pp. 264–313. DOI: 10.1002/andp.18170560706.
- [2] H. Hertz. “Ueber einen Einfluss des ultravioletten Lichtes auf die elektrische Entladung”. In: *Annalen der Physik und Chemie* 267.8 (1887), pp. 983–1000. DOI: 10.1002/andp.18872670827.
- [3] A. Einstein. “Über einen die Erzeugung und Verwandlung des Lichtes betreffenden heuristischen Gesichtspunkt”. In: *Annalen der Physik* 322.6 (1905), pp. 132–148. DOI: 10.1002/andp.19053220607.
- [4] T. H. Maiman. “Stimulated Optical Radiation in Ruby”. In: *Nature* 187.4736 (1960), pp. 493–494. DOI: 10.1038/187493a0.
- [5] Georg A. Reider. *Photonics*. Springer International Publishing, 2016. DOI: 10.1007/978-3-319-26076-1.
- [6] Markus Kitzler and Stefanie Gräfe, eds. *Ultrafast Dynamics Driven by Intense Light Pulses*. Springer International Publishing, 2016. DOI: 10.1007/978-3-319-20173-3.
- [7] Thomas Brabec and Ferenc Krausz. “Intense few-cycle laser fields: Frontiers of nonlinear optics”. In: *Reviews of Modern Physics* 72.2 (2000), pp. 545–591. DOI: 10.1103/revmodphys.72.545.
- [8] Ferenc Krausz and Misha Ivanov. “Attosecond physics”. In: *Reviews of Modern Physics* 81.1 (2009), pp. 163–234. DOI: 10.1103/revmodphys.81.163.
- [9] W. Becker et al. “Above-Threshold Ionization: From Classical Features to Quantum Effects”. In: *Advances In Atomic, Molecular, and Optical Physics*. Elsevier, 2002, pp. 35–98. DOI: 10.1016/s1049-250x(02)80006-4.
- [10] B. Walker et al. “Precision Measurement of Strong Field Double Ionization of Helium”. In: *Physical Review Letters* 73.9 (1994), pp. 1227–1230. DOI: 10.1103/physrevlett.73.1227.

## Bibliography

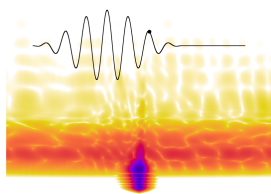
- [11] P. A. Franken, A. E. Hill, C. W. Peters, and G. Weinreich. “Generation of Optical Harmonics”. In: *Physical Review Letters* 7.4 (1961), pp. 118–119. DOI: 10.1103/physrevlett.7.118.
- [12] Georg A. Reider. “XUV attosecond pulses: generation and measurement”. In: *Journal of Physics D: Applied Physics* 37.5 (2004), R37–R48. DOI: 10.1088/0022-3727/37/5/r01.
- [13] A. M. Perelomov, V. S. Popov, and M. V. Terent’ev. “Ionization of Atoms in an Alternating Electric Field”. In: *Soviet Journal of Experimental and Theoretical Physics* 23 (1966), p. 924.
- [14] A. M. Perelomov, V. S. Popov, and M. V. Terent’ev. “Ionization of Atoms in an Alternating Electric Field: II”. In: *Soviet Journal of Experimental and Theoretical Physics* 24 (1967), p. 207.
- [15] Maxim V. Ammosov, Nikolai B. Delone, and Vladimir P. Krainov. “Tunnel ionization of complex atoms and atomic ions in electromagnetic field”. In: *High intensity laser processes*. Vol. 664. SPIE, 1986, pp. 138–141. DOI: 10.1117/12.938695.
- [16] L. V. Keldysh. “Ionization in the field of a strong electromagnetic wave”. In: *Sov. Phys. JETP* 20.5 (1965), pp. 1307–1314.
- [17] F. H. M. Faisal. “Collision of electrons with laser photons in a background potential”. In: *Journal of Physics B: Atomic and Molecular Physics* 6.11 (1973), pp. L312–L315. DOI: 10.1088/0022-3700/6/11/003.
- [18] Howard R. Reiss. “Effect of an intense electromagnetic field on a weakly bound system”. In: *Physical Review A* 22.5 (1980), pp. 1786–1813. DOI: 10.1103/physreva.22.1786.
- [19] Jeffrey L. Krause, Kenneth J. Schafer, and Kenneth C. Kulander. “High-order harmonic generation from atoms and ions in the high intensity regime”. In: *Physical Review Letters* 68.24 (1992), pp. 3535–3538. DOI: 10.1103/physrevlett.68.3535.
- [20] P. B. Corkum. “Plasma perspective on strong field multiphoton ionization”. In: *Physical Review Letters* 71.13 (1993), pp. 1994–1997. DOI: 10.1103/physrevlett.71.1994.
- [21] Wolfgang Demtröder. *Atoms, Molecules and Photons*. Springer Berlin Heidelberg, 2010. DOI: 10.1007/978-3-642-10298-1.



- [22] Ahmed H. Zewail. “Laser Femtochemistry”. In: *Science* 242.4886 (1988), pp. 1645–1653. DOI: 10.1126/science.242.4886.1645.
- [23] Ahmed H. Zewail. “Femtochemistry: Atomic-Scale Dynamics of the Chemical Bond”. In: *The Journal of Physical Chemistry A* 104.24 (2000), pp. 5660–5694. DOI: 10.1021/jp001460h.
- [24] Marc J. J. Vrakking and Franck Lepine. *Attosecond molecular dynamics*. Vol. 13. Royal Society of Chemistry, 2018. DOI: 10.1039/9781788012669.
- [25] S. Gräfe and V. Engel. “Indirect versus direct photoionization with ultrashort pulses: interferences and time-resolved bond-length changes”. In: *Chemical Physics Letters* 385.1-2 (2004), pp. 60–65. DOI: 10.1016/j.cplett.2003.12.047.
- [26] Manfred Lein. “Attosecond Probing of Vibrational Dynamics with High-Harmonic Generation”. In: *Physical Review Letters* 94.5 (2005), p. 053004. DOI: 10.1103/physrevlett.94.053004.
- [27] S. Baker et al. “Probing Proton Dynamics in Molecules on an Attosecond Time Scale”. In: *Science* 312.5772 (2006), pp. 424–427. DOI: 10.1126/science.1123904.
- [28] T. Zuo and A. D. Bandrauk. “Charge-resonance-enhanced ionization of diatomic molecular ions by intense lasers”. In: *Physical Review A* 52.4 (1995), R2511–R2514. DOI: 10.1103/physreva.52.r2511.
- [29] Tamar Seideman, M. Yu. Ivanov, and P. B. Corkum. “Role of Electron Localization in Intense-Field Molecular Ionization”. In: *Physical Review Letters* 75.15 (1995), pp. 2819–2822. DOI: 10.1103/physrevlett.75.2819.
- [30] Volkhard May and Oliver Kühn. *Charge and Energy Transfer Dynamics in Molecular Systems*. Wiley, 2011. DOI: 10.1002/9783527633791.
- [31] R. A. Marcus. “On the Theory of Oxidation-Reduction Reactions Involving Electron Transfer. I”. In: *The Journal of Chemical Physics* 24.5 (1956), pp. 966–978. DOI: 10.1063/1.1742723.
- [32] R. A. Marcus. “Electrostatic Free Energy and Other Properties of States Having Nonequilibrium Polarization. I”. In: *The Journal of Chemical Physics* 24.5 (1956), pp. 979–989. DOI: 10.1063/1.1742724.
- [33] Hans Jakob Wörner et al. “Charge migration and charge transfer in molecular systems”. In: *Structural Dynamics* 4.6 (2017), p. 061508. DOI: 10.1063/1.4996505.

## Bibliography

- [34] S. Lepp, P. C. Stancil, and A. Dalgarno. “Atomic and molecular processes in the early Universe”. In: *Journal of Physics B: Atomic, Molecular and Optical Physics* 35.10 (2002), R57–R80. DOI: 10.1088/0953-4075/35/10/201.
- [35] Rolf Güsten et al. “Astrophysical detection of the helium hydride ion  $\text{HeH}^+$ ”. In: *Nature* 568.7752 (2019), pp. 357–359. DOI: 10.1038/s41586-019-1090-x.
- [36] Michele Pavanello, Sergiy Bubin, Marcin Molski, and Ludwik Adamowicz. “Non-Born–Oppenheimer calculations of the pure vibrational spectrum of  $\text{HeH}^+$ ”. In: *The Journal of Chemical Physics* 123.10 (2005), p. 104306. DOI: 10.1063/1.2012332.
- [37] T. R. Hogness and E. G. Lunn. “The Ionization of Hydrogen by Electron Impact as Interpreted by Positive Ray Analysis”. In: *Physical Review* 26.1 (1925), pp. 44–55. DOI: 10.1103/physrev.26.44.
- [38] Zhuan Liu and Paul B. Davies. “Infrared laser absorption spectroscopy of rotational and vibration rotational transitions of  $\text{HeH}^+$  up to the dissociation threshold”. In: *The Journal of Chemical Physics* 107.2 (1997), pp. 337–341. DOI: 10.1063/1.474394.
- [39] Alejandro Saenz. “Photoabsorption and photoionization of  $\text{HeH}^+$ ”. In: *Phys. Rev. A* 67 (3 2003), p. 033409. DOI: 10.1103/PhysRevA.67.033409.
- [40] J. Fernández and F. Martín. “Photoionization of the  $\text{HeH}^+$  molecular ion”. In: *Journal of Physics B: Atomic, Molecular and Optical Physics* 40.12 (2007), pp. 2471–2480. DOI: 10.1088/0953-4075/40/12/020.
- [41] H. B. Pedersen et al. “Crossed Beam Photodissociation Imaging of  $\text{HeH}^+$  with Vacuum Ultraviolet Free-Electron Laser Pulses”. In: *Phys. Rev. Lett.* 98 (22 2007), p. 223202. DOI: 10.1103/PhysRevLett.98.223202.
- [42] Irina Dumitriu and Alejandro Saenz. “Photodissociation of the  $\text{HeH}^+$  molecular ion”. In: *Journal of Physics B: Atomic, Molecular and Optical Physics* 42.16 (2009), p. 165101. DOI: 10.1088/0953-4075/42/16/165101.
- [43] Qing Liao, Peixiang Lu, Qingbin Zhang, Zhenyu Yang, and Xinbing Wang. “Double ionization of  $\text{HeH}^+$  molecules in intense laser fields”. In: *Optics Express* 16.21 (2008), p. 17070. DOI: 10.1364/oe.16.017070.

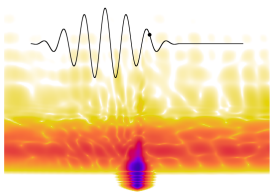




- [44] D. Ursrey, F. Anis, and B. D. Esry. “Multiphoton dissociation of  $\text{HeH}^+$  below the  $\text{He}^+(1s)+\text{H}(1s)$  threshold”. In: *Phys. Rev. A* 85 (2 2012), p. 023429. DOI: 10.1103/PhysRevA.85.023429.
- [45] E. Dehghanian, A. D. Bandrauk, and G. Lagmago Kamta. “Enhanced ionization of the non-symmetric  $\text{HeH}^+$  molecule driven by intense ultrashort laser pulses”. In: *The Journal of Chemical Physics* 139.8 (2013), p. 084315. DOI: 10.1063/1.4818528.
- [46] D. Ursrey and B. D. Esry. “Using the carrier-envelope phase to control strong-field dissociation of  $\text{HeH}^+$  at midinfrared wavelengths”. In: *Phys. Rev. A* 96 (6 2017), p. 063409. DOI: 10.1103/PhysRevA.96.063409.
- [47] Shang Wang, Jun Cai, and Yanjun Chen. “Ionization dynamics of polar molecules in strong elliptical laser fields”. In: *Physical Review A* 96.4 (2017), p. 043413. DOI: 10.1103/physreva.96.043413.
- [48] A. Vilà, J. Zhu, A. Scrinzi, and A. Emmanouilidou. “Intertwined electron-nuclear motion in frustrated double ionization in driven heteronuclear molecules”. In: *Journal of Physics B: Atomic, Molecular and Optical Physics* 51.6 (2018), p. 065602. DOI: 10.1088/1361-6455/aaaa2a.
- [49] Philipp Wustelt et al. “Heteronuclear Limit of Strong-Field Ionization: Fragmentation of  $\text{HeH}^+$  by Intense Ultrashort Laser Pulses”. In: *Phys. Rev. Lett.* 121 (7 2018), p. 073203. DOI: 10.1103/PhysRevLett.121.073203.
- [50] Simon Brennecke and Manfred Lein. “High-order above-threshold ionization beyond the electric dipole approximation”. In: *Journal of Physics B: Atomic, Molecular and Optical Physics* 51.9 (2018), p. 094005. DOI: 10.1088/1361-6455/aab91f.
- [51] Bing Zhang and Manfred Lein. “High-order harmonic generation from diatomic molecules in an orthogonally polarized two-color laser field”. In: *Physical Review A* 100.4 (2019), p. 043401. DOI: 10.1103/physreva.100.043401.
- [52] Nicolas Eicke, Simon Brennecke, and Manfred Lein. “Attosecond-Scale Streaking Methods for Strong-Field Ionization by Tailored Fields”. In: *Physical Review Letters* 124.4 (2020), p. 043202. DOI: 10.1103/physrevlett.124.043202.

## Bibliography

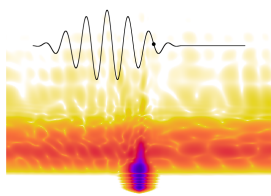
- [53] Florian Oppermann et al. “Dissociation and ionization of  $\text{HeH}^+$  in sub-cycle-controlled intense two-color fields”. In: *Journal of Physics B: Atomic, Molecular and Optical Physics* 53.17 (2020). DOI: 10.1088/1361-6455/ab9a93.
- [54] Florian Oppermann, Saurabh Mhatre, Stefanie Gräfe, and Manfred Lein. “Mass-ratio dependent strong-field dissociation of artificial helium hydride isotopologues”. In: *Journal of Physics B: Atomic, Molecular and Optical Physics* (2023), accepted. arXiv: 2301.04500.
- [55] John Nuckolls, Lowell Wood, Albert Thiessen, and George Zimmerman. “Laser Compression of Matter to Super-High Densities: Thermonuclear (CTR) Applications”. In: *Nature* 239.5368 (1972), pp. 139–142. DOI: 10.1038/239139a0.
- [56] A. B. Zylstra et al. “Record Energetics for an Inertial Fusion Implosion at NIF”. In: *Physical Review Letters* 126.2 (2021), p. 025001. DOI: 10.1103/physrevlett.126.025001.
- [57] Jörn Bleck-Neuhaus. “Quarks, Gluonen, Starke Wechselwirkung”. In: *Elementare Teilchen*. Springer Berlin Heidelberg, 2010, pp. 585–632. DOI: 10.1007/978-3-540-85300-8\_13.
- [58] Albert Einstein. “Zur Quantentheorie der Strahlung”. In: *Physikalische Zeitschrift* 18 (1917), pp. 121–128.
- [59] Norbert Straumann. *Einstein in 1916: “On the Quantum Theory of Radiation”*. 2017. arXiv: 1703.08176.
- [60] Christopher Gerry and Peter Knight. *Introductory Quantum Optics*. Cambridge University Press, 2004. ISBN: 9780511229497.
- [61] Richard Phillips Feynman, Robert B. Leighton, and Matthew Sands. *The Feynman Lectures on Physics, Vol. 2*. Addison Wesley, 1971, p. 592. ISBN: 9780201021172. URL: [https://feynmanlectures.caltech.edu/II\\_toc.html](https://feynmanlectures.caltech.edu/II_toc.html).
- [62] D. B. Milošević, G. G. Paulus, D. Bauer, and W. Becker. “Above-threshold ionization by few-cycle pulses”. In: *Journal of Physics B: Atomic, Molecular and Optical Physics* 39.14 (2006), R203–R262. DOI: 10.1088/0953-4075/39/14/r01.
- [63] A. Ludwig et al. “Breakdown of the Dipole Approximation in Strong-Field Ionization”. In: *Physical Review Letters* 113.24 (2014), p. 243001. DOI: 10.1103/physrevlett.113.243001.



- [64] Reiner M. Dreizler and Eberhard K. U. Gross. *Density Functional Theory*. Springer Berlin Heidelberg, 1990. DOI: 10.1007/978-3-642-86105-5.
- [65] Eberhard Engel and Reiner M. Dreizler. *Density Functional Theory*. Springer Berlin Heidelberg, 2011. DOI: 10.1007/978-3-642-14090-7.
- [66] David Hochstuhl and Michael Bonitz. “Time-dependent restricted-active-space configuration-interaction method for the photoionization of many-electron atoms”. In: *Physical Review A* 86.5 (2012), p. 053424. DOI: 10.1103/physreva.86.053424.
- [67] S. Bauch, L. K. Sørensen, and L. B. Madsen. “Time-dependent generalized-active-space configuration-interaction approach to photoionization dynamics of atoms and molecules”. In: *Physical Review A* 90.6 (2014), p. 062508. DOI: 10.1103/physreva.90.062508.
- [68] Kenneth C. Kulander. “Multiphoton ionization of hydrogen: A time-dependent theory”. In: *Physical Review A* 35.1 (1987), pp. 445–447. DOI: 10.1103/physreva.35.445.
- [69] C. I. Blaga et al. “Strong-field photoionization revisited”. In: *Nature Physics* 5.5 (2009), pp. 335–338. DOI: 10.1038/nphys1228.
- [70] Michael Spanner, Jochen Mikosch, Arjan Gijsbertsen, Andrey E. Boguslavskiy, and Albert Stolow. “Multielectron effects and nonadiabatic electronic dynamics in above threshold ionization and high-harmonic generation”. In: *New Journal of Physics* 13.9 (2011), p. 093010. DOI: 10.1088/1367-2630/13/9/093010.
- [71] Chuan Yu and Lars Bojer Madsen. “Above-threshold ionization of helium in the long-wavelength regime: Examining the single-active-electron approximation and the two-electron strong-field approximation”. In: *Physical Review A* 95.6 (2017), p. 063407. DOI: 10.1103/physreva.95.063407.
- [72] Kasra Amini et al. “Symphony on strong field approximation”. In: *Reports on Progress in Physics* 82.11 (2019), p. 116001. DOI: 10.1088/1361-6633/ab2bb1.
- [73] Alexander Kramida, Yuri Ralchenko, J. Reader, and NIST ASD Team. *NIST Atomic Spectra Database, NIST Standard Reference Database 78*. 1999. DOI: 10.18434/T4W30F. URL: <https://physics.nist.gov/asd>.

## Bibliography

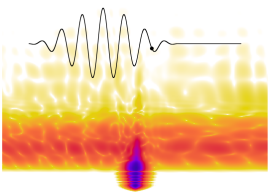
- [74] F. Gesztesy. “On the one-dimensional Coulomb Hamiltonian”. In: *Journal of Physics A: Mathematical and General* 13.3 (1980), pp. 867–875. DOI: 10.1088/0305-4470/13/3/019.
- [75] P. Kurasov. “On the Coulomb potential in one dimension”. In: *Journal of Physics A: Mathematical and General* 29.8 (1996), pp. 1767–1771. DOI: 10.1088/0305-4470/29/8/023.
- [76] J. Javanainen, J. H. Eberly, and Qichang Su. “Numerical simulations of multiphoton ionization and above-threshold electron spectra”. In: *Physical Review A* 38.7 (1988), pp. 3430–3446. DOI: 10.1103/physreva.38.3430.
- [77] Stefanie Kerbstadt, Kevin Eickhoff, Tim Bayer, and Matthias Wollenhaupt. “Bichromatic Control of Free Electron Wave Packets”. In: *Topics in Applied Physics*. Springer International Publishing, 2020, pp. 43–76. DOI: 10.1007/978-3-030-47098-2\_3.
- [78] Philipp Wustelt. “Atome und Moleküle fundamentaler Bedeutung in intensiven Laserfeldern: He, He<sup>+</sup> und HeH<sup>+</sup>”. PhD thesis. 2019. DOI: 10.22032/DBT.38372.
- [79] Mathias Uhlmann, Thomas Kunert, and Rüdiger Schmidt. “Molecular alignment of fragmenting H<sub>2</sub><sup>+</sup> and H<sub>2</sub> in strong laser fields”. In: *Physical Review A* 72.4 (2005), p. 045402. DOI: 10.1103/physreva.72.045402.
- [80] Lun Yue et al. “Strong-field polarizability-enhanced dissociative ionization”. In: *Phys. Rev. A* 98 (4 2018), p. 043418. DOI: 10.1103/PhysRevA.98.043418.
- [81] Krzysztof Pachucki. “Born-Oppenheimer potential for HeH<sup>+</sup>”. In: *Physical Review A* 85.4 (2012), p. 042511. DOI: 10.1103/physreva.85.042511.
- [82] T. A. Green, H. H. Michels, J. C. Browne, and M. M. Madsen. “Configuration interaction studies of the HeH<sup>+</sup> molecular ion. I Singlet sigma states”. In: *The Journal of Chemical Physics* 61.12 (1974), pp. 5186–5199. DOI: 10.1063/1.1681864.
- [83] W. Kołos. “Long- and intermediate-range interaction in three lowest sigma states of the HeH<sup>+</sup> ion”. In: *International Journal of Quantum Chemistry* 10.2 (1976), pp. 217–224. DOI: 10.1002/qua.560100203.



- [84] T. G. Winter, M. D. Duncan, and N. F. Lane. “Exact eigenvalues, electronic wavefunctions and their derivatives with respect to the internuclear separation for the lowest 20 states of the  $\text{HeH}^{2+}$  molecule”. In: *Journal of Physics B: Atomic and Molecular Physics* 10.2 (1977), pp. 285–304. DOI: 10.1088/0022-3700/10/2/016.
- [85] M. Frigo and S.G. Johnson. “The Design and Implementation of FFTW3”. In: *Proceedings of the IEEE* 93.2 (2005), pp. 216–231. DOI: 10.1109/jproc.2004.840301.
- [86] M. D. Feit, J. A. Fleck, and A. Steiger. “Solution of the Schrödinger equation by a spectral method”. In: *Journal of Computational Physics* 47.3 (1982), pp. 412–433. DOI: 10.1016/0021-9991(82)90091-2.
- [87] Nicolas Thomas Eicke. “Momentum distributions from bichromatic ionization of atoms and molecules”. PhD thesis. Hannover: Gottfried Wilhelm Leibniz Universität, 2020. DOI: 10.15488/10082.
- [88] Frank Grossmann. “Molecules in Strong Laser Fields”. In: *Infinity in Early Modern Philosophy*. Springer International Publishing, 2018, pp. 173–256. DOI: 10.1007/978-3-319-74542-8\_5.
- [89] G. Lagmago Kamta and A. D. Bandrauk. “Phase Dependence of Enhanced Ionization in Asymmetric Molecules”. In: *Phys. Rev. Lett.* 94.20 (2005), p. 203003. DOI: 10.1103/PhysRevLett.94.203003.
- [90] G. Lagmago Kamta and A. D. Bandrauk. “Nonsymmetric molecules driven by intense few-cycle laser pulses: Phase and orientation dependence of enhanced ionization”. In: *Phys. Rev. A* 76.5 (2007), p. 053409. DOI: 10.1103/PhysRevA.76.053409.
- [91] Moshe Shapiro. “Photofragmentation and mapping of nuclear wavefunctions”. In: *Chemical Physics Letters* 81.3 (1981), pp. 521–527. DOI: 10.1016/0009-2614(81)80455-1.
- [92] M.S. Child and M. Shapiro. “Photodissociation and the Condon reflection principle”. In: *Molecular Physics* 48.1 (1983), pp. 111–128. DOI: 10.1080/00268978300100081.
- [93] M. S. Child, Hanno Essén, and Robert J. Le Roy. “An RKR-like inversion procedure for bound–continuum transition intensities”. In: *The Journal of Chemical Physics* 78.11 (1983), pp. 6732–6740. DOI: 10.1063/1.444673.

## Bibliography

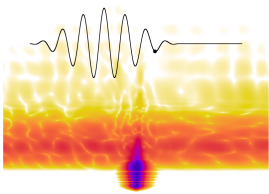
- [94] T. Nubbemeyer, K. Gorling, A. Saenz, U. Eichmann, and W. Sandner. “Strong-Field Tunneling without Ionization”. In: *Phys. Rev. Lett.* 101.23 (2008), p. 233001. DOI: 10.1103/PhysRevLett.101.233001.
- [95] B. Manschwetus et al. “Strong Laser Field Fragmentation of  $H_2$ : Coulomb Explosion without Double Ionization”. In: *Physical Review Letters* 102.11 (2009), p. 113002. DOI: 10.1103/physrevlett.102.113002.
- [96] Francisco M. Fernández and Javier Garcia. “Highly Accurate Potential Energy Curves for the Hydrogen Molecular Ion”. In: *ChemistrySelect* 6.35 (2021), pp. 9527–9534. DOI: 10.1002/slct.202102509.
- [97] Bernold Feuerstein and Uwe Thumm. “Fragmentation of  $H_2^+$  in strong 800-nm laser pulses: Initial-vibrational-state dependence”. In: *Physical Review A* 67.4 (2003), p. 043405. DOI: 10.1103/physreva.67.043405.
- [98] André D. Bandrauk and Jonathan Ruel. “Charge-resonance-enhanced ionization of molecular ions in intense laser pulses: Geometric and orientation effects”. In: *Physical Review A* 59.3 (1999), pp. 2153–2162. DOI: 10.1103/physreva.59.2153.
- [99] Amalia Apalategui, Alejandro Saenz, and P. Lambropoulos. “Effect of vibration and internuclear axis orientation on multiphoton ionization of  $H_2^+$ ”. In: *Journal of Physics B: Atomic, Molecular and Optical Physics* 33.14 (2000), pp. 2791–2807. DOI: 10.1088/0953-4075/33/14/316.
- [100] Fatima Anis and B. D. Esry. “Role of nuclear rotation in dissociation of  $H_2^+$  in a short laser pulse”. In: *Phys. Rev. A* 77 (3 2008), p. 033416. DOI: 10.1103/PhysRevA.77.033416.
- [101] T. Rathje et al. “Coherent Control at Its Most Fundamental: Carrier-Envelope-Phase-Dependent Electron Localization in Photodissociation of a  $H_2^+$  Molecular Ion Beam Target”. In: *Physical Review Letters* 111.9 (2013), p. 093002. DOI: 10.1103/physrevlett.111.093002.
- [102] T. Rathje et al. “Review of attosecond resolved measurement and control via carrier-envelope phase tagging with above-threshold ionization”. In: *Journal of Physics B: Atomic, Molecular and Optical Physics* 45.7 (2012), p. 074003. DOI: 10.1088/0953-4075/45/7/074003.



- [103] Philipp Wustelt et al. “Laser-Driven Anharmonic Oscillator: Ground-State Dissociation of the Helium Hydride Molecular Ion by Midinfrared Pulses”. In: *Physical Review Letters* 127.4 (2021). DOI: 10.1103/PhysRevLett.127.043202.
- [104] Pengqian Wang, A. Max Saylor, Kevin D. Carnes, Brett D. Esry, and Itzik Ben-Itzhak. “Disentangling the volume effect through intensity-difference spectra: application to laser-induced dissociation of  $H_2^+$ ”. In: *Opt. Lett.* 30.6 (2005), pp. 664–666. DOI: 10.1364/OL.30.000664.
- [105] Mette B. Gaarde, Jennifer L. Tate, and Kenneth J. Schafer. “Macroscopic aspects of attosecond pulse generation”. In: *Journal of Physics B: Atomic, Molecular and Optical Physics* 41.13 (2008), p. 132001. DOI: 10.1088/0953-4075/41/13/132001.
- [106] Pengfei Lan et al. “Attosecond Probing of Nuclear Dynamics with Trajectory-Resolved High-Harmonic Spectroscopy”. In: *Physical Review Letters* 119.3 (2017), p. 033201. DOI: 10.1103/physrevlett.119.033201.
- [107] J. Loreau, J. Lecointre, X. Urbain, and N. Vaeck. “Rovibrational analysis of the XUV photodissociation of  $HeH^+$  ions”. In: *Physical Review A* 84.5 (2011), p. 053412. DOI: 10.1103/physreva.84.053412.
- [108] Erich Goll, Günter Wunner, and Alejandro Saenz. “Formation of Ground-State Vibrational Wave Packets in Intense Ultrashort Laser Pulses”. In: *Physical Review Letters* 97.10 (2006), p. 103003. DOI: 10.1103/physrevlett.97.103003.
- [109] H. G. Muller, P. H. Bucksbaum, D. W. Schumacher, and A. Zavriyev. “Above-threshold ionisation with a two-colour laser field”. In: *Journal of Physics B: Atomic, Molecular and Optical Physics* 23.16 (1990), pp. 2761–2769. DOI: 10.1088/0953-4075/23/16/018.
- [110] E. Charron, A. Giusti-Suzor, and F. H. Mies. “Two-color coherent control of  $H_2^+$  photodissociation in intense laser fields”. In: *Physical Review Letters* 71.5 (1993), pp. 692–695. DOI: 10.1103/physrevlett.71.692.
- [111] B. Sheehy, B. Walker, and L. F. DiMauro. “Phase Control in the Two-Color Photodissociation of  $HD^+$ ”. In: *Phys. Rev. Lett.* 74.24 (1995), pp. 4799–4802. DOI: 10.1103/PhysRevLett.74.4799.

## Bibliography

- [112] N. Dudovich et al. “Measuring and controlling the birth of attosecond XUV pulses”. In: *Nature Physics* 2.11 (2006), pp. 781–786. DOI: 10.1038/nphys434.
- [113] D. Ray et al. “Momentum spectra of electrons rescattered from rare-gas targets following their extraction by one- and two-color femtosecond laser pulses”. In: *Phys. Rev. A* 83.1 (2011), p. 013410. DOI: 10.1103/PhysRevA.83.013410.
- [114] Dror Shafir et al. “Resolving the time when an electron exits a tunnelling barrier”. In: *Nature* 485.7398 (2012), pp. 343–346. DOI: 10.1038/nature11025.
- [115] Xinhua Xie et al. “Probing the influence of the Coulomb field on atomic ionization by sculpted two-color laser fields”. In: *New Journal of Physics* 15.4 (2013), p. 043050. DOI: 10.1088/1367-2630/15/4/043050.
- [116] Li Zhang et al. “Laser-sub-cycle two-dimensional electron-momentum mapping using orthogonal two-color fields”. In: *Phys. Rev. A* 90.6 (2014), p. 061401. DOI: 10.1103/PhysRevA.90.061401.
- [117] Jinlei Liu et al. “Trajectory-based analysis of low-energy electrons and photocurrents generated in strong-field ionization”. In: *Phys. Rev. A* 90.6 (2014), p. 063420. DOI: 10.1103/PhysRevA.90.063420.
- [118] S. Skruszewicz et al. “Two-Color Strong-Field Photoelectron Spectroscopy and the Phase of the Phase”. In: *Phys. Rev. Lett.* 115.4 (2015), p. 043001. DOI: 10.1103/PhysRevLett.115.043001.
- [119] P. B. Corkum, N. H. Burnett, and F. Brunel. “Above-threshold ionization in the long-wavelength limit”. In: *Physical Review Letters* 62.11 (1989), pp. 1259–1262. DOI: 10.1103/physrevlett.62.1259.
- [120] K. J. Schafer, Baorui Yang, L. F. DiMauro, and K. C. Kulander. “Above threshold ionization beyond the high harmonic cutoff”. In: *Physical Review Letters* 70.11 (1993), pp. 1599–1602. DOI: 10.1103/physrevlett.70.1599.
- [121] G. G. Paulus, W. Becker, and H. Walther. “Classical rescattering effects in two-color above-threshold ionization”. In: *Physical Review A* 52.5 (1995), pp. 4043–4053. DOI: 10.1103/physreva.52.4043.

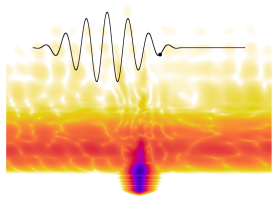




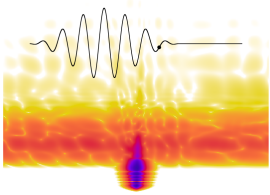
- [122] K. B. Laughlin, Geoffrey A. Blake, R. C. Cohen, D. C. Hovde, and R. J. Saykally. “Determination of the dipole moment of  $\text{ArH}^+$  from the rotational Zeeman effect by tunable far infrared laser spectroscopy”. In: *Physical Review Letters* 58.10 (1987), pp. 996–999. DOI: 10.1103/physrevlett.58.996.
- [123] G. Audi, F. G. Kondev, Meng Wang, W. J. Huang, and S. Naimi. “The NUBASE2016 evaluation of nuclear properties”. In: *Chinese Physics C* 41.3 (2017), p. 030001. DOI: 10.1088/1674-1137/41/3/030001.
- [124] Florian Oppermann, Nicolas Eicke, and Manfred Lein. “Real-time propagator eigenstates”. In: *Journal of Physics B: Atomic, Molecular and Optical Physics* (2022). DOI: 10.1088/1361-6455/ac8bb9.
- [125] C. Runge. “Über die numerische Auflösung von Differentialgleichungen”. In: *Mathematische Annalen* 46.2 (1895), pp. 167–178. DOI: 10.1007/bf01446807.
- [126] W. Kutta. “Beitrag zur näherungsweise Integration totaler Differentialgleichungen”. In: *Zeit. Math. Phys.* 46 (1901), pp. 435–53.
- [127] E. Wigner. “On the Quantum Correction For Thermodynamic Equilibrium”. In: *Physical Review* 40.5 (1932), pp. 749–759. DOI: 10.1103/physrev.40.749.
- [128] R. L. Hudson. “When is the wigner quasi-probability density non-negative?” In: *Reports on Mathematical Physics* 6.2 (1974), pp. 249–252. DOI: 10.1016/0034-4877(74)90007-x.
- [129] E. Colomé, Z. Zhan, and X. Oriols. “Comparing Wigner, Husimi and Bohmian distributions: which one is a true probability distribution in phase space?” In: *Journal of Computational Electronics* 14.4 (2015), pp. 894–906. DOI: 10.1007/s10825-015-0737-6.
- [130] N. H. Abel. “Auflösung einer mechanischen Aufgabe.” In: *Journal für die reine und angewandte Mathematik (Crelles Journal)* 1826.1 (1826), pp. 153–157. DOI: 10.1515/crll.1826.1.153.
- [131] M. Born and R. Oppenheimer. “Zur Quantentheorie der Molekeln”. In: *Annalen der Physik* 389.20 (1927), pp. 457–484. DOI: 10.1002/andp.19273892002.

## Bibliography

- [132] Michael Victor Berry. “Quantal phase factors accompanying adiabatic changes”. In: *Proceedings of the Royal Society of London. A. Mathematical and Physical Sciences* 392.1802 (1984), pp. 45–57. DOI: 10.1098/rspa.1984.0023.
- [133] Hermann Haken and Hans Christoph Wolf. *Molekülphysik und Quantenchemie*. Springer Berlin Heidelberg, 1992. DOI: 10.1007/978-3-662-08832-6.
- [134] Wei-Chih Liu and C. W. Clark. “Closed-form solutions of the Schrödinger equation for a model one-dimensional hydrogen atom”. In: *Journal of Physics B: Atomic, Molecular and Optical Physics* 25.21 (1992), pp. L517–L524. DOI: 10.1088/0953-4075/25/21/001.
- [135] Peter Schwerdtfeger and Jeffrey K. Nagle. “2018 Table of static dipole polarizabilities of the neutral elements in the periodic table”. In: *Molecular Physics* 117.9-12 (2018), pp. 1200–1225. DOI: 10.1080/00268976.2018.1535143.
- [136] P. W. Fowler. “Energy, polarizability and size of confined one-electron systems”. In: *Molecular Physics* 53.4 (1984), pp. 865–889. DOI: 10.1080/00268978400102701.
- [137] S. P. Goldman. “Gauge-invariance method for accurate atomic-physics calculations: Application to relativistic polarizabilities”. In: *Physical Review A* 39.3 (1989), pp. 976–980. DOI: 10.1103/physreva.39.976.
- [138] R. Kosloff and H. Tal-Ezer. “A direct relaxation method for calculating eigenfunctions and eigenvalues of the Schrödinger equation on a grid”. In: *Chemical Physics Letters* 127.3 (1986), pp. 223–230. DOI: [https://doi.org/10.1016/0009-2614\(86\)80262-7](https://doi.org/10.1016/0009-2614(86)80262-7).
- [139] William H. Press, Saul A. Teukolsky, William T. Vetterling, and Brian P. Flannery. *Numerical Recipes 3rd Edition. The Art of Scientific Computing*. Cambridge University Press, 2007, p. 1256. ISBN: 9780521880688. URL: <http://numerical.recipes/>.
- [140] B. V. Noumerov. “A Method of Extrapolation of Perturbations”. In: *Monthly Notices of the Royal Astronomical Society* 84.8 (1924), pp. 592–602. DOI: 10.1093/mnras/84.8.592.



- [141] R. V. Mises and H. Pollaczek-Geiringer. “Praktische Verfahren der Gleichungsauflösung .” In: *ZAMM - Journal of Applied Mathematics and Mechanics / Zeitschrift für Angewandte Mathematik und Mechanik* 9.2 (1929), pp. 152–164. DOI: <https://doi.org/10.1002/zamm.19290090206>.



# Acknowledgements

SOLI DEO GLORIA

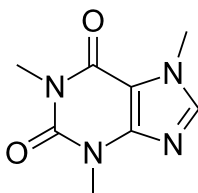
This work is the result of a long journey through the world of physics research which would not have been possible without many people accompanying and guiding me.

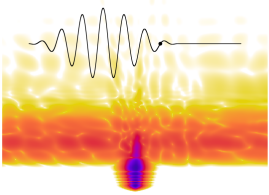
First and foremost, I am grateful to my supervisor Manfred Lein for giving me the opportunity to do full-time research in an international group with a lot of freedom and fun. He also organized the QUTIF DFG priority programme which I was a part of and which allowed me to meet many fantastic colleagues.

As a part of our QUTIF collaboration, I have had many fruitful discussions with Philipp Wustelt, Lun Yue and Saurabh Mhatre as well as with their professors Gerhard G. Paulus and Stefanie Gräfe.

I want to express my gratitude towards my officemates in the institute (first Marc Ruhmann, later Tobias Florin) who endured my jokes and lifted my spirits. The same holds for my closest friends and regular mensa company: Stina Scheer, Daniel Edler, Christoph Dreißigacker and Julian Westerweck

During all this time I found a lot of support in my church, in the famous #theobubble on Twitter and of course in my *family* without whom I'd not be where I am now.



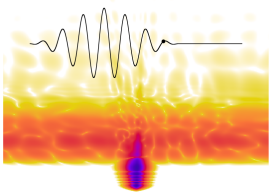


# Curriculum Vitae

- 14 June 1992 Born in Hannover, Germany
- 1998 – 2010 School in Hannover,  
Degree: Abitur (general qualification for university entrance)
- 2010 – 2015 Studies of physics at Leibniz University Hannover:
- 2014 Bachelor's thesis: "Quantenzustände auf dem Sierpiński-Teppich"  
Supervisor: Manfred Lein  
Degree: Bachelor of Science
- 2015 Master's thesis: "Die Poincaré-symmetrische Saite"  
Supervisor: Norbert Dragon  
Degree: Master of Science
- 2015 – 2023 PhD student / scientific assistant at Leibniz University Hannover,  
group of Manfred Lein

## List of publications

- [1] Philipp Wustelt, **Florian Oppermann**, Lun Yue, Max Möller, Thomas Stöhlker, Manfred Lein, Stefanie Gräfe, Gerhard G. Paulus, and A. Max Sayler. “Heteronuclear Limit of Strong-Field Ionization: Fragmentation of  $\text{HeH}^+$  by Intense Ultrashort Laser Pulses”. In: *Phys. Rev. Lett.* 121 (7 2018), p. 073203. DOI: 10.1103/PhysRevLett.121.073203.
- [2] Lun Yue, Philipp Wustelt, A. Max Sayler, **Florian Oppermann**, Manfred Lein, Gerhard G. Paulus, and Stefanie Gräfe. “Strong-field polarizability-enhanced dissociative ionization”. In: *Phys. Rev. A* 98 (4 2018), p. 043418. DOI: 10.1103/PhysRevA.98.043418.
- [3] Hongcheng Ni, Nicolas Eicke, Camilo Ruiz, Jun Cai, **Florian Oppermann**, Nikolay I. Shvetsov-Shilovski, and Liang-Wen Pi. “Tunneling criteria and a nonadiabatic term for strong-field ionization”. In: *Physical Review A* 98.1 (2018), p. 013411. DOI: 10.1103/physreva.98.013411.
- [4] **Florian Oppermann**, Philipp Wustelt, T. Florin, S. Mhatre, Gerhard G. Paulus, Manfred Lein, and Stefanie Gräfe. “Dissociation and ionization of  $\text{HeH}^+$  in sub-cycle-controlled intense two-color fields”. In: *Journal of Physics B: Atomic, Molecular and Optical Physics* 53.17 (2020). DOI: 10.1088/1361-6455/ab9a93.
- [5] Philipp Wustelt, **Florian Oppermann**, Saurabh Mhatre, Matthias Kübel, A. Max Sayler, Manfred Lein, Stefanie Gräfe, and Gerhard G. Paulus. “Laser-Driven Anharmonic Oscillator: Ground-State Dissociation of the Helium Hydride Molecular Ion by Midinfrared Pulses”. In: *Physical Review Letters* 127.4 (2021). DOI: 10.1103/PhysRevLett.127.043202.
- [6] Norbert Dragon and **Florian Oppermann**. “Heisenberg Algebra and String Theory”. In: (2022). arXiv: 2203.03063.
- [7] **Florian Oppermann**, Nicolas Eicke, and Manfred Lein. “Real-time propagator eigenstates”. In: *Journal of Physics B: Atomic, Molecular and Optical Physics* (2022). DOI: 10.1088/1361-6455/ac8bb9.





- [8] Norbert Dragon and **Florian Oppermann**. “Heisenberg versus the Covariant String”. In: (2022). arXiv: 2212.07256.
- [9] Norbert Dragon and **Florian Oppermann**. “The Rough with the Smooth of the Light Cone String”. In: (2022). arXiv: 2212.14822.
- [10] **Florian Oppermann**, Saurabh Mhatre, Stefanie Gräfe, and Manfred Lein. “Mass-ratio dependent strong-field dissociation of artificial helium hydride isotopologues”. In: *Journal of Physics B: Atomic, Molecular and Optical Physics* (2023), accepted. arXiv: 2301.04500.

